



저작자표시-비영리-변경금지 2.0 대한민국

이용자는 아래의 조건을 따르는 경우에 한하여 자유롭게

- 이 저작물을 복제, 배포, 전송, 전시, 공연 및 방송할 수 있습니다.

다음과 같은 조건을 따라야 합니다:



저작자표시. 귀하는 원저작자를 표시하여야 합니다.



비영리. 귀하는 이 저작물을 영리 목적으로 이용할 수 없습니다.



변경금지. 귀하는 이 저작물을 개작, 변형 또는 가공할 수 없습니다.

- 귀하는, 이 저작물의 재이용이나 배포의 경우, 이 저작물에 적용된 이용허락조건을 명확하게 나타내어야 합니다.
- 저작권자로부터 별도의 허가를 받으면 이러한 조건들은 적용되지 않습니다.

저작권법에 따른 이용자의 권리는 위의 내용에 의하여 영향을 받지 않습니다.

이것은 [이용허락규약\(Legal Code\)](#)을 이해하기 쉽게 요약한 것입니다.

[Disclaimer](#)

공학박사학위논문

A Study on Composite-Based Magnetorheological
Fluids for Resolution of Trade-Off Between
Performance and Long-Term Stability

성능-침강안정성 상충 문제 해결을 위한
복합체 기반 자기유변유체에 대한 연구

2021 년 2월

서울대학교 대학원

재료공학부

최 준 석

A Study on Composite-Based
Magnetorheological Fluids for Resolution of
Trade-Off Between Performance and Long-
Term Stability

성능-침강안정성 상충 문제 해결을 위한
복합체 기반 자기유변유체에 대한 연구

지도교수 서 용 석

이 논문을 최준석 박사학위논문으로 제출함

2020 년 10월

서울대학교 대학원

재료공학부

최준석

최준석의 박사학위논문을 인준함

2020 년 12월

위 원 장	홍 성 현
부위원장	서 용 석
위 원	윤 재 룬
위 원	김 장 주
위 원	최 형 진



Handwritten signatures of the committee members, including the names of the members listed in the table to the left.

Abstract

A Study on Composite-Based Magnetorheological Fluids for Resolution of Trade-Off Between Performance and Long-Term Stability

Junsok Choi

Department of Materials Science and Engineering

The Graduate School

Seoul National University

Magnetorheological (MR) fluids are smart materials composed of magnetic particles dispersed in magnetically-insulating carrier medium. With magnetic field, chain-like structures are formed due to dipole-induced magnetostatic interaction between magnetic particles, and the structures inhibit the flow and increase the viscosity of MR fluids in very short time. This characteristic enables the rheological properties of MR fluids to be easily tailored with magnetic field strength. Due to this unique response, MR fluids can be used for actuator systems like power steering pumps haptic devices, and active suspensions, and damper systems in automobile, bridges, buildings and so on.

A huge obstacle for application of MR fluids is their poor long-term stability against the

sedimentation of magnetic particles. The large difference in the density between heavy magnetic particles and light medium make magnetic particles quickly go down to bottom, reducing the MR fluids' length of life. One of the strategies for improvement of the long-term stability was to reduce the density of magnetic particles by synthesizing magnetic composite materials. Fabrication of magnetic composites using light materials such as polymer, silica, carbon materials efficiently have reduced the density mismatch between magnetic materials and carrier medium, enhancing the long-term stability of MR fluids. However, there was trade-off between long-term stability and performance of MR fluids because use of light materials is equivalent to the deterioration in magnetic properties.

In this study, various magnetic composites with different composition and structures were fabricated for the objective of producing MR fluids having excellent performance and long-term stability simultaneously. As a first step, hollow structured polymer-Fe₃O₄ composite particles were synthesized using SiO₂ as sacrificial template. With cavity inside, the hollow magnetic composite particles showed the density only 40 % of bare Fe₃O₄ and the large improvement in long-term stability of MR suspensions could be observed. To avoid huge decline in MR performance with non-magnetic polymers, hierarchically-structured Fe₃O₄ nanoparticles were prepared with simple electrospaying process. By excluding polymers, hierarchically-structured Fe₃O₄ had magnetization value very closed to its primary nanoparticles, leading to MR performance higher more than 3 times of hollow structured polymer-Fe₃O₄ suspensions. At the same time, the pores inside reduced the density of the structured particles by 23 %, resulting in better long-term stability of

hierarchically-structured Fe_3O_4 suspension than bare Fe_3O_4 suspension.

To minimize the trade-off between MR performance and long-term stability (density of magnetic particles), non-spherical, CoFeNi-based magnetic composites were fabricated and applied for MR fluids. CNT- $\text{Co}_{0.4}\text{Fe}_{0.4}\text{Ni}_{0.2}$ composite was produced by synthesizing $\text{Co}_{0.4}\text{Fe}_{0.4}\text{Ni}_{0.2}$ on the surface of functionalized CNTs. Much higher magnetization of $\text{Co}_{0.4}\text{Fe}_{0.4}\text{Ni}_{0.2}$ compared to Fe_3O_4 enabled CNT- $\text{Co}_{0.4}\text{Fe}_{0.4}\text{Ni}_{0.2}$ suspension to have much superior MR performance than Fe_3O_4 composite-based MR fluids. Also, due to high aspect ratio of CNTs, outstanding long-term stability of 22 % light transmission was observed with formation of 3-dimensional network structures. Finally, magnetically non-active CNTs were replaced by magnetizable, flake-shaped sendust. The high drag coefficient of flake sendust, combined with roughened surface due to attached $\text{Co}_{0.4}\text{Fe}_{0.4}\text{Ni}_{0.2}$ nanoparticles, resulted in excellent stability with 23 % of light transmission despite of the high density of sendust- $\text{Co}_{0.4}\text{Fe}_{0.4}\text{Ni}_{0.2}$ composite particles. Also, because both constituents of sendust- $\text{Co}_{0.4}\text{Fe}_{0.4}\text{Ni}_{0.2}$ are both magnetic materials with high magnetization value, the MR fluids retained very high yield stress value.

Keywords: Magnetorheological fluids, sedimentation problem, long-term stability, MR performance, magnetic composites, aspect ratio

Student Number: 2016-20839

Contents

Abstract	i
Contents	v
List of Tables	x
List of Figures	xi
Chapter 1. Introduction	1
1. 1. Magnetorheological (MR) Fluids and Applications.....	1
1. 2. Long-Term Stability Problem and Proposed Solutions	4
1. 3. Research Objectives	7
References	9
Chapter 2. Backgrounds	16
2. 1. Definition of Terms	16
2. 1. 1. Shear Stress	16
2. 1 .2. Shear Rate	16
2. 1. 3. Shear Viscosity.....	17
2. 1 .4. Viscoelastic Behavior	17

2. 1. 4. 1. Storage Modulus and Loss Modulus	17
2. 2. Yield Stress of MR Fluids	18
2. 2. 1. Rheological Models for Prediction of Dynamic and Static Yield Stress	19
2. 2 .2. Yield Stress Dependency on the Magnetic Field Strength	22
2. 3. Mechanism of Structures Evolution	25
References	27

Chapter 3. Suspensions of Hollow Polydivinylbenzene Nanoparticles Decorated with Fe₃O₄ Nanoparticles as Magnetorheological Fluids for Microfluidics Applications31

3. 1. Introduction	31
3. 2. Experimental Section	34
3. 2. 1. Synthesis of Hollow Polydivinylbenzene (h-PDVB) Particles	34
3. 2. 2. Deposition of Fe ₃ O ₄ onto Hollow PDVB Particles	36
3. 2. 3. Characterization	37
3. 3. Results and Discussion	41

3. 3. 1 Morphology and Structures	41
3. 3. 2. Magnetorheological Behaviors	48
3. 3. 3. Long-Term Stability of Suspensions	62
3. 4. Conclusion	65
References	67

Chapter 4. Hierarchically Structured Fe₃O₄ Nanoparticles for High-Performance Magnetorheological Fluids with Long-Term Stability

4. 1. Introduction	74
4. 2. Experimental Section	77
4. 2. 1. Synthesis of Citric Acid-Capped Fe ₃ O ₄	77
4. 2. 2. Fabrication of HS-Fe ₃ O ₄ with Electrospaying Process	78
4. 2. 3. Characterization	79
4. 3. Results and Discussion	82
4. 3. 1. Morphology and Structures	82

4. 3. 2. Magnetorheological Behaviors	89
4. 3. 3. Long-Term Stability of Suspensions	103
4. 4. Conclusion	106
References	108

Chapter 5. High-Performance Magnetorheological Fluids of Carbon Nanotube-CoFeNi Composites with Enhanced Long-Term Stability.....116

5. 1. Introduction	116
5. 2. Experimental Section	119
5. 2. 1. Functionalization of Carbon Nanotubes	119
5. 2. 2. Synthesis of $\text{Co}_{0.4}\text{Fe}_{0.4}\text{Ni}_{0.2}$ and $\text{CNT-Co}_{0.4}\text{Fe}_{0.4}\text{Ni}_{0.2}$	119
5. 2. 3. Characterization	120
5. 3. Results and Discussion	123
5. 3. 1. Morphology and Structures	123
5. 3. 2. Magnetorheological Behaviors	130

5. 3. 3. Long-Term Stability of Suspensions	142
5. 4. Conclusion	145
References	146

**Chapter 6. Sendust-CoFeNi Magnetic-Magnetic Composites-
Based Magnetorheological Fluids for Simultaneous Improvement
of Performance and Long-Term Stability154**

6. 1. Introduction	154
6. 2. Experimental Section	157
6. 2. 1. Synthesis of Citric Acid-Capped Fe ₃ O ₄	157
6. 2. 2. Characterization	157
6. 3. Results and Discussion	159
6. 3. 1. Morphology and Structures	159
6. 3. 2. Magnetorheological Behaviors	163
6. 3. 3. Long-Term Stability of Suspensions	176
6. 4. Conclusion	179

References	181
Chapter 7. Conclusions	188
7. 1. Overall conclusion	188
7. 2. Further works	194
References	195
국문초록	196
List of Publication	199
Appendix	201
Appendix A. Nonisothermal Crystallization Behaviors of Structure-Modified Polyamides (Nylon 6s)	201

List of Tables

Table 3. 1. Static Yield Stress and Dynamic Yield Stress of Fe_3O_4 , h-PDVB@ Fe_3O_4 and f-PS/ Fe_3O_4	59
Table 4. 1. Static yield stress and dynamic yield stress of Fe_3O_4 composites-based MR suspensions	99
Table 5. 1. Static yield stress and dynamic yield stress of $\text{Co}_{0.4}\text{Fe}_{0.4}\text{Ni}_{0.2}$, CNT- $\text{Co}_{0.4}\text{Fe}_{0.4}\text{Ni}_{0.2}$, and Fe_3O_4 composites-based MR suspensions	139
Table 6. 1. Static yield stress and dynamic yield stress of $\text{Co}_{0.4}\text{Fe}_{0.4}\text{Ni}_{0.2}$, FS, and $\text{Co}_{0.4}\text{Fe}_{0.4}\text{Ni}_{0.2}$ composites-based MR fluids	173

List of Figures

Figure 1. 1. Schematic diagram for reversible formation of chain-like structures in MR fluids	3
Figure 2. 1. Static and dynamic yield stress of MR fluids	24
Figure 3. 1. Schematic diagram for the synthesis of h-PDVB@Fe ₃ O ₄ particles.	39
Figure 3. 2. TGA curves of h-PDVB, h-PDVB@Fe ₃ O ₄ ($\rho = 2.51\text{g/cm}^3$) and h-PDVB@Fe ₃ O ₄ ($\rho = 1.83\text{g/cm}^3$).	40
Figure 3. 3. SEM images of (a) MPS-modified SiO ₂ , (b) SiO ₂ /PDVB, (c) h-PDVB, and (d) h-PDVB@Fe ₃ O ₄ (1.83), TEM images of (e) h-PDVB, (f) h-PDVB@Fe ₃ O ₄ (1.83) (the inset showed magnified view of the particle surface), and (g) h-PDVB@Fe ₃ O ₄ (2.51)	44
Figure 3. 4. XRD patterns for Fe ₃ O ₄ and h-PDVB@Fe ₃ O ₄	45
Figure 3. 5. Optical microscopic images of microstructural change for h-PDVB@Fe ₃ O ₄ (1.83) suspension (a) before and (b) after the application of external magnetic field.	46
Figure 3. 6. VSM data for pure Fe ₃ O ₄ , h-PDVB@Fe ₃ O ₄ (1.83) and h-PDVB@Fe ₃ O ₄ (2.51) particles ($1\text{ Oe} = 10^3/4\pi\text{ A/m}$).	47

Figure 3. 7. (a) Amplitude sweep dependence of storage modulus and (b) Frequency dependence of storage modulus and loss modulus for pure Fe ₃ O ₄ (4.52), h-PDVB@Fe ₃ O ₄ (1.83) and h-PDVB@Fe ₃ O ₄ (2.51) suspensions under 343 kA/m magnetic field (strain = 0.003 %).	56
Figure 3. 8. (a) Shear stress and (b) shear viscosity flow curves for pure Fe ₃ O ₄ , h-PDVB@Fe ₃ O ₄ (1.83) and h-PDVB@Fe ₃ O ₄ (2.51). The black solid lines and the blue dashed lines in (a) indicate predictions according to Bingham model and Seo-Seo model	57
Figure 3. 9. Shear viscosity vs shear stress curves for pure Fe ₃ O ₄ and h-PDVB@Fe ₃ O ₄ suspensions	58
Figure 3. 10. HRTEM images of (a) Fe ₃ O ₄ nanoparticles of h-PDVB@Fe ₃ O ₄ and (b) a cubic Fe ₃ O ₄ of f-PS/Fe ₃ O ₄	60
Figure 3. 11. Dimensionless apparent viscosity of the MR fluids as a function of $\dot{\gamma}/M^2$ at various magnetic field strengths	61
Figure 3. 12. Transmission [%] curve as a function of time [h] for pure Fe ₃ O ₄ , h-PDVB@Fe ₃ O ₄ (1.83), and h-PDVB@Fe ₃ O ₄ (2.51).	64
Figure 4. 1. Schematic description of the electrospray process.	81
Figure 4. 2. SEM ((a) and (b)) and TEM ((c) and (d)) images of HS-Fe ₃ O ₄ particles.	85

Figure 4. 3. (a) VSM curves for capped Fe_3O_4 and HS- Fe_3O_4 (the inset shows that all particles have a low coercive field. (b) TGA profiles of capped Fe_3O_4 and HS- Fe_3O_486

Figure 4. 4. XRD patterns for capped- Fe_3O_4 and HS- Fe_3O_487

Figure 4. 5. Optical microscopic images of microstructural change for HS- Fe_3O_4 suspension. (a) before and (b) after application of the external magnetic field of 86 kA/m.88

Figure 4. 6. (a) amplitude sweep (strain dependence) of storage modulus, G' and (b) Frequency sweep (frequency dependence) of storage modulus (G') and loss modulus(G'') for capped Fe_3O_4 and HS- Fe_3O_4 suspension at 86 kA/m and 343 kA/m.96

Figure 4. 7. (a) shear stress and (b) viscosity curves as a function of shear rate for MR fluids of capped- Fe_3O_4 and HS- Fe_3O_497

Figure 4. 8. Shear viscosity as a function of shear stress for capped- Fe_3O_4 and HS- Fe_3O_4 MR fluids at 86 kA/m and 343 kA/m.98

Figure 4. 9. Transient responses (reversibility) of the capped- Fe_3O_4 and HS- Fe_3O_4 MR fluids at shear rate of 1 s^{-1}100

Figure 4. 10. Normalized static yield stress obtained from the fits to the Seo–Seo model (Eq. (2)) versus the normalized magnetic field strength. The lines show the quadratic

dependence fits. ($\eta_{sy} = 0.543 \cdot H^2 + 0.448$ for the capped Fe_3O_4 particle suspension (●), whereas $\eta_{sy} = 0.455 \cdot H^2 + 0.544$ for the HS Fe_3O_4 particle suspension; H is the normalized magnetic field strength).101

Figure 4. 11. Dimensionless apparent viscosity of the MR fluids as a function of $\dot{\gamma}/M^2$ at various magnetic field strengths.102

Figure 4. 12. Transmission (%) curve as a function of time (h) for capped- Fe_3O_4 and HS- Fe_3O_4 particles for 24h.105

Figure 5. 1. Schematic diagram for synthesis of CNT- $Co_{0.4}Fe_{0.4}Ni_{0.2}$ 122

Figure 5. 2. SEM images of (a) CNTs (b) CNT- $Co_{0.4}Fe_{0.4}Ni_{0.2}$ (c) TEM image of CNT- $Co_{0.4}Fe_{0.4}Ni_{0.2}$ 126

Figure 5. 3. VSM curves for $Co_{0.4}Fe_{0.4}Ni_{0.2}$ and CNT- $Co_{0.4}Fe_{0.4}Ni_{0.2}$ 127

Figure 5. 4. XRD patterns for $Co_{0.4}Fe_{0.4}Ni_{0.2}$ and CNT- $Co_{0.4}Fe_{0.4}Ni_{0.2}$ 128

Figure 5. 5. Optical microscopic images of microstructural change for CNT- $Co_{0.4}Fe_{0.4}Ni_{0.2}$ suspension. (a) before and (b) after application of the external magnetic field of 86 kA/m.129

Figure 5. 6. (a) amplitude sweep (strain dependence) of storage modulus, G' and (b) Frequency sweep (frequency dependence) of storage modulus (G') and loss modulus(G'') for $Co_{0.4}Fe_{0.4}Ni_{0.2}$ and CNT- $Co_{0.4}Fe_{0.4}Ni_{0.2}$ suspension at 86 kA/m and 343

kA/m.	136
Figure 5. 7. (a) shear stress and (b) viscosity curves as a function of shear rate for MR fluids of $\text{Co}_{0.4}\text{Fe}_{0.4}\text{Ni}_{0.2}$ and CNT- $\text{Co}_{0.4}\text{Fe}_{0.4}\text{Ni}_{0.2}$	137
Figure 5. 8. Shear viscosity as a function of shear stress for $\text{Co}_{0.4}\text{Fe}_{0.4}\text{Ni}_{0.2}$ and CNT- $\text{Co}_{0.4}\text{Fe}_{0.4}\text{Ni}_{0.2}$ MR fluids at 86 kA/m and 343 kA/m.	138
Figure 5. 9. Transient responses (reversibility) of the $\text{Co}_{0.4}\text{Fe}_{0.4}\text{Ni}_{0.2}$ and CNT- $\text{Co}_{0.4}\text{Fe}_{0.4}\text{Ni}_{0.2}$ MR fluids at shear rate of 1 s^{-1}	140
Figure 5. 10. Dimensionless apparent viscosity of the MR fluids as a function of $\dot{\gamma}/\text{M}^2$ at various magnetic field strengths.	141
Figure 5. 11. Transmission (%) curve as a function of time (h) for $\text{Co}_{0.4}\text{Fe}_{0.4}\text{Ni}_{0.2}$ and CNT- $\text{Co}_{0.4}\text{Fe}_{0.4}\text{Ni}_{0.2}$ particles for 24h.	144
Figure 6. 1. SEM images of (a),(b) flake sendust ((b) is magnified image of surface)) and (c),(d) FS@ $\text{Co}_{0.4}\text{Fe}_{0.4}\text{Ni}_{0.2}$ ((d) is magnified image of surface)	161
Figure 6. 2. VSM curves for $\text{Co}_{0.4}\text{Fe}_{0.4}\text{Ni}_{0.2}$, FS, and FS@ $\text{Co}_{0.4}\text{Fe}_{0.4}\text{Ni}_{0.2}$	162
Figure 6. 3. (a) amplitude sweep (strain dependence) of storage modulus, G' and (b) Frequency sweep (frequency dependence) of storage modulus (G') and loss modulus(G'') for FS and FS@ $\text{Co}_{0.4}\text{Fe}_{0.4}\text{Ni}_{0.2}$ suspension at 86 kA/m and 343 kA/m.	170

Figure 6. 4. (a) shear stress and (b) viscosity curves as a function of shear rate for MR fluids of FS and FS@Co _{0.4} Fe _{0.4} Ni _{0.2}	171
Figure 6. 5. Shear viscosity as a function of shear stress for FS and FS@Co _{0.4} Fe _{0.4} Ni _{0.2} MR fluids at 86 kA/m and 343 kA/m.	172
Figure 6. 6. Transient responses (reversibility) of the FS and FS@Co _{0.4} Fe _{0.4} Ni _{0.2} MR fluids at shear rate of 1 s ⁻¹	174
Figure 6. 7. Dimensionless apparent viscosity of the MR fluids as a function of $\dot{\gamma}/M^2$ at various magnetic field strengths.	175
Figure 6. 8. Transmission (%) curve as a function of time (h) for Co _{0.4} Fe _{0.4} Ni _{0.2} , FS, and FS@Co _{0.4} Fe _{0.4} Ni _{0.2} particles for 24h.....	178
Figure 7. 1. Yield stress at 343 kA/m and long-term stability of composite-based MR fluids in this work.	192
Figure 7. 2. Static yield stress and Long-term stability of various MR fluids. Open symbols correspond to bare magnetic particle-based MR fluids or composite-based fluids in previous works. Closed symbols presents composite-based MR fluids in this dissertation.	193

Chapter 1. Introduction

1. 1. Magnetorheological (MR) Fluids and Applications

MR fluids are suspensions of magnetizable particles (carbonyl iron, Fe_3O_4 , Fe_2O_3 etc) in magnetically-insulating carrier medium and are class of smart materials because their properties can be varied with external magnetic field. [1-4] When magnetic field is applied to MR fluids, the magnetic particles are aligned into along the direction of magnetic field due to magnetic dipole-induced attractive interaction between the magnetic particles, forming chain-like mesostructures. [3, 5] As soon as magnetic field is removed, reverse structural change occurs and MR fluids return to their original state. During this process, the rheological properties of MR fluids are changed by three or four orders of magnitude. [1-6] Under magnetic field, chain-like structures strongly restrict the flow of MR fluids and increase the viscosity by several orders, imparting solid-like elastic properties to MR fluids. [7,8] Whereas, MR fluids are in liquid-like viscous state without external magnetic field. Besides, the rheological properties of MR fluids can be easily fine-tuned by controlling the strength of applied magnetic field. [3]

The salient field-responsive properties of MR fluids is suitable for areas where active control of vibration or transmission of torque is needed. [2] The most well-known area is automobile industries where MR fluid systems can be applied for linear dampers, rotor

dampers, rotary brakes, clutches, power steering pumps, and torque transducer. [1,2,5] MR fluids also is used for seat suspension and shock absorbers in vehicles to provide safety to drivers and passengers. [9,10] MR fluids also can be applied in industrial area as control valves, hybrid actuators, and the haptic devices. [5,8] For polishing area, MR finishing technology has been used as advanced and intelligent polishing technology which minimize surface damages of materials with various shapes. [11,12] For military application, MR fluids systems protects soldiers as bullet-resistant body armor and military vehicle's suspension systems. [13,14]. In medical area, they are used for prosthetic legs or hands, reducing external impact during walking and enabling exquisite motion through control of viscosity. [15] For medical haptic devices, MR fluids can provide tunable stiffness display, which is essential for safe robotic surgery. [16] On a larger scale, MR suspensions systems is applied as damper systems for bridges (Dong Ting lake bridge in China, Eiland bridge in Netherlands) to reduce impact caused by gust of winds. [17,18] These systems also can be applied for skyscrapers, where stabilization against wind or earthquake is needed. [19, 20]

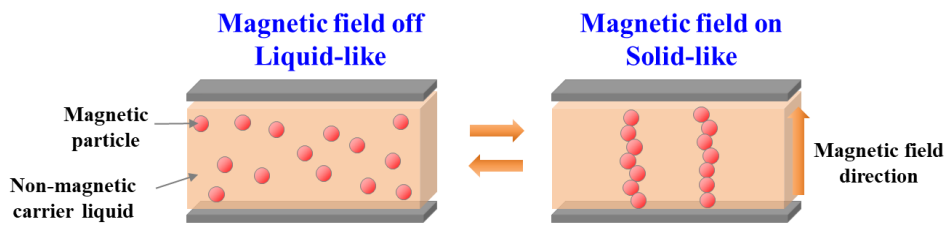


Figure 1. 1. Schematic diagram for reversible formation of chain-like structures in MR fluids

1. 2. Long-Term Stability Problem and Proposed Solutions

Despite of tremendous potential for commercialization, a major problem should be resolved for MR fluids: poor long-term stability. [1,21] This problem is mainly caused by fast sedimentation of magnetic particles in MR fluids. [15, 22] Because of huge density difference between heavy magnetic particles with ideal density higher than 5 g/cm^3 and light carrier medium with density around 1 g/cm^3 , magnetic particles quickly settle down to the bottom. Once the sedimentation occurs, the redispersion of magnetic particles in MR systems becomes very hard, and reuse of the MR fluid systems become almost impossible. [2] To maintain suspended state of magnetic particles as long as possible, considerable effort has been made.

Some research have been tried to prevent sedimentation of magnetic particles by simply replace carrier medium from conventional (water, silicone oil, mineral oil) ones to new ones. Rankin et al. tried to use viscoplastic media to inhibit the fast sedimentation of carbonyl iron particles. [23] They fabricated viscoplastic media by diluting grease with mineral oil. Due to viscoplastic media's own yield stress, the sedimentation of suspended carbonyl iron significantly decreased. [24] Guerrero-Sanchez et al. applied imidazolium-based ionic liquids with various structures of cations and anions as carrier medium. [24] The affinity between magnetic particles and ionic liquid, and steric hindrance effect coming from large ions prevent the direct contact between magnetic particles. In addition, the relatively high viscosity of ionic liquids slows down the motion of magnetic particles,

resulting in lowered sedimentation velocity.

Another common strategy is addition of some additives to MR fluids. One of those methods was to add a thickener to carrier liquid. With the addition of thickener the viscosity of MR fluids greatly increases, and prevents the settling of magnetic particles by lowering sedimentation velocity of them. [25,26] Unfortunately, with increase of viscosity at the absence of magnetic field, the range of controllable rheological properties reduces. Some researchers added surfactants to MR fluids. With addition of surfactants, the steric barrier was introduced on the surface of magnetic particles due to its large hydrophobic chains. [27,28] This barrier prevents the irreversible aggregation of magnetic particles and improve the compatibility between magnetic particles and medium. [27-30] Also, submicron-sized gap-fillers like carbon nanotubes/fibers, clays to prevent the sedimentation of micro-sized magnetic particles. [31] These fillers fill the gap between magnetic particles, preventing direct physical contact between magnetic particles and caking behavior. [32] Also, with proper proportion, fillers can reinforcement chain-like structures and improvement MR performance. [31]

A strategy recently received much attention is to fabricate magnetic composite materials for MR fluids. By combining magnetic materials with light-weight materials like polymers, silica, carbon-based materials, magnetic composite materials for MR fluids with a variety of structures have been produced. The density of the composite materials decreased much from that of bare magnetic materials, and the reduced density mismatch between particles and medium make composite-based MR fluids to have better stability than bare magnetic

particles-based MR fluids.

Core-shell structured particles are the most reported composite particles for MR fluids. One kind of core-shell structured composite particles are particles with magnetic cores and passivation layers (mesoporous silica, polymers and so on) coated on the surface. [2,5,32-36] Not only this coated layer decrease the density of magnetic particles, the layer also protect magnetic particles from oxidation and irreversible contact with other particles. [2, 37] The other kind of core-shell particles are particles with magnetically-insulating core encapsulated by magnetic particles. [21,37] Because distance between magnetic particles under magnetic field is closer compared to the case when magnetic particles in is core, the performance of MR suspensions would be better for this kind of composite particles. Besides of core-shell particles, composite particles with pores or cavity inside the structure were produced and used for MR fluids. For examples, polymer-based magnetic composites with pores inside polymeric part were synthesized by foaming polymers with supercritical carbon oxide. [2,37] Also, hollow structured polystyrene-Fe₃O₄ composite particles with big cavity inside polystyrene were used for MR fluids. [38] Due to very low density of air, those composites showed much lower density when compared to polymer-based core-shell magnetic composite particles, leading to superior long-term stability of MR fluids. There were also studies about magnetic composites with non-spherical shapes. Through the combination of magnetic particles with materials having high aspect ratio such as carbon nanotubes and sepiolite, magnetic composites with high aspect ratio were obtained. [39-41] Due to high aspect ratio, improved MR response compared to spherical-shaped

particles. [39] In addition, such tube or fiber-like composite materials would form 3-dimensional, percolated network structures in suspension when their concentration is sufficiently high, which with lowered density, contribute to long-term stability of MR fluids. [41]

1. 3 Research Objectives

With the use of magnetic composite materials, there have been significant progress for obtaining better long-term stability of MR fluids. However, due to application of magnetically-insulating materials, the magnetic properties of magnetic materials were seriously deteriorated, and this problem directly resulted in large degeneration of MR performance. The main objective of this research is to obtain composite-based MR fluids having excellent long-term stability and MR performance at the same time. For this purpose, we have fabricated magnetic composite materials with various materials and structures. Then, we applied the composite materials to MR fluids and evaluate their MR performance and long-term stability. In chapter 3, spherical-shaped hollow structured polymer-Fe₃O₄ composite materials with high content of Fe₃O₄ was synthesized and their MR suspensions were characterized. Chapter 4 describes spherical-shaped, hierarchically structured-Fe₃O₄ nanoparticles containing no polymeric materials. In chapter 5, the effect of replacement of magnetic particles and shape of composite materials in MR performance and long-term stability of MR fluid was investigated. Finally, in chapter 6, composite

materials composed of only magnetically-susceptible materials were produced, and MR performance and long-term stability of their MR suspension was examined.

References

- (1) Seo, Y. P.; Han, S.; Choi, J.; Takahara, A.; Choi, H. J.; Seo, Y. Searching for a Stable High-Performance Magnetorheological Suspension. *Adv. Mater.* 2018, *30*, 1704769.
- (2) Chuah, W. H.; Zhang, W. L.; Choi, H. J.; Seo, Y. Magnetorheology of Core-Shell Structured Carbonyl Iron/Polystyrene Foam Nanoparticles Suspension with Enhanced Stability. *Macromolecules* 2015, *48* (19), 7311–7319.
- (3) Ghaffari, A.; Hashemabadi, S.; Ashtiani, M. A review on this simulation and modeling of magnetorheological fluids. *J. Intell. Mater. Syst. Struct.* 2015, *26*, 881.
- (4) Parlak, Z.; Engin, T. Time-dependent CFD and quasi-static analysis of magnetorheological fluid dampers with experimental validation. *Int. J. Mech. Sci.* 2012, *64*, 22-31
- (5) Liu, Y. D.; Lee, J.; Choi, S. B.; Choi, H. J. Silica-coated carbonyl iron microsphere based magnetorheological fluid and its damping force characteristics. *Smart Mater. Struct.* 2013, *22* (6), 065022.
- (6) Lee, S.; Noh, J.; Hong, S.; Kim, Y. K.; Jang, J., Dual stimuli-responsive smart fluid of graphene oxide-coated iron oxide/silica core/shell nanoparticles. *Chem. Mater.* **2016**, *28* (8), 2624-2633
- (7) López-López, M. T.; Gómez-Ramírez, A.; Rodríguez-Arco, L.; Durán, J. D.; Iskakova, L.; Zubarev, A., Colloids on the frontier of ferrofluids. Rheological properties.

Langmuir **2012**, 28 (15), 6232-6245.

(8) Park, B. J.; Fang, F. F.; Choi, H. J., Magnetorheology: materials and application. *Soft Matter* 2010, 6 (21), 5246-5253.

(9) Sun, S.; Ning, D.; Yang, J.; Du, H.; Zhang, S.; Li, W., A seat suspension with a rotary magnetorheological damper for heavy duty vehicles. *Smart Mater. Struct.* 2016, 25 (10), 105032.

(10) Kim, H.-C.; Shin, Y.-J.; You, W.; Jung, K. C.; Oh, J.-S.; Choi, S.-B., A ride quality evaluation of a semi-active railway vehicle suspension system with MR damper: railway field tests. *Proc. Inst. Mech. Eng. Pt. F J. Rail Rapid Transit.* 2017, 231 (3), 306-316.

(11) Lee, J.W.; Hong, K.P.; Kwon, S.H.; Choi, H.J.; Cho, M.W. Suspension rheology and magnetorheological finishing characteristics of biopolymer-coated carbonyl Iron particles. *Ind. Eng. Chem. Res.* 2017, 56, 2416-2424.

(12) Tao, R.; Xu, X. Reducing the viscosity of crude oil by pulsed electric or magnetic field. *Energy Fuels* 2006, 20, 2046-2051.

(13) Ha, S. H.; Seong, M.-S.; Choi, S.-B., Design and vibration control of military vehicle suspension system using magnetorheological damper and disc spring. *Smart Mater. Struct.* 2013, 22 (6), 065006.

(14) Simon, D.; Ahmadian, M., Vehicle evaluation of the performance of magneto

rheological dampers for heavy truck suspensions. *J. Vib. Acoust.* 2001, *123* (3), 365-375.

(15) Park, J.; Yoon, G.-H.; Kang, J.-W.; Choi, S.-B., Design and control of a prosthetic leg for above-knee amputees operated in semi-active and active modes. *Smart Mater. Struct.* 2016, *25* (8), 085009.

(16) Yang, T.-H.; Kwon, H.-J.; Lee, S. S.; An, J.; Koo, J.-H.; Kim, S.-Y.; Kwon, D.-S., Development of a miniature tunable stiffness display using MR fluids for haptic application. *Sens. Actuator A Phys.* 2010, *163* (1), 180-190.

(17) Chen, Z.; Wang, X.; Ko, J.; Ni, Y.; Spencer, B. F.; Yang, G. MR damping system on Dongting Lake cable-stayed bridge. *Proc. SPIE* 2003, *5057*, 229–236.

(18) Weber, F.; Distl, H., Amplitude and frequency independent cable damping of Sutong Bridge and Russky Bridge by magnetorheological dampers. *Struct. Control. Health. Monit.* 2015, *22* (2), 237-254.

(19) Bitaraf, M.; Ozbulut, O. E.; Hurlebaus, S.; Barroso, L. Application of semi-active control strategies for seismic protection of buildings with MR dampers. *Engineering Structures* 2010, *32* (10), 3040–3047.

(20) Oliveira, F.; de Morais, P. G.; Suleman, A. Semi-active control of base-isolated structures. *Procedia Eng.* 2015, *114*, 401–409.

(21) Choi, H. J.; Zhang, W. L.; Kim, S.; Seo, Y. Core-Shell Structured Electro- and Magneto-Responsive Materials: Fabrication and Characteristics. *Materials* 2014, *7* (11),

7460–7471.

(22) Kim, Y. J.; Liu, Y. D.; Seo, Y.; Choi, H. J., Pickering-emulsion-polymerized polystyrene/Fe₂O₃ composite particles and their magnetoresponse characteristics. *Langmuir* 2013, 29 (16), 4959-4965.

(23) Rankin, P. J.; Horvath, A. T.; Klingenberg, D. J. Magnetorheology in viscoplastic media. *Rheol. Acta* 1999, 38 (5), 471–477.

(24) Guerrero-Sanchez, C.; Lara-Ceniceros, T.; Jimenez-Regalado, E.; Raşa, M.; Schubert, U. S., Magnetorheological fluids based on ionic liquids. *Advanced Materials* 2007, 19 (13), 1740-1747.

(25) Mrlik, M.; Ilcikova, M.; Pavlinek, V.; Mosnacěk, J.; Peer, P.; Filip, P. Improved thermooxidation and sedimentation stability of covalently-coated carbonyl iron particles with cholesteryl groups and their influence on magnetorheology. *J. Colloid Interface Sci.* 2013, 396, 146-151.

(26) Cvek, M.; Mrlik, M.; Ilcikova, M.; Mosnacěk, J.; Munster, L.; Pavlinek, V.; Pavlinek, V. Synthesis of Silicone Elastomers Containing Silyl-Based Polymer-Grafted Carbonyl Iron Particles: An Efficient Way To Improve Magnetorheological, Damping, and Sensing Performances. *Macromolecules*, 2017, 50, 2189-2200.

(27) López-López, M. T.; Kuzhir, P.; Bossis, G.; Mingalyov, P., Preparation of well-dispersed magnetorheological fluids and effect of dispersion on their magnetorheological properties. *Rheologica Acta* 2008, 47 (7), 787-796.

- (28) Fei, C.; Zuzhi, T.; Xiangfan, W., Novel process to prepare high-performance magnetorheological fluid based on surfactants compounding. *Materials and Manufacturing Processes* 2015, 30 (2), 210-215.
- (29) Lopez-Lopez, M.T.; Vicente, J.D.; Gonzalez-Caballero, F.; Duran, J.D.G. Stability of magnetizable colloidal suspensions by addition of oleic acid and silica nanoparticles. *Colloids Surf. A Physicochem. Eng. Asp.* 2005, 264 (1–3), 75–81.
- (30) Hato, M.J.; Choi, H.J.; Sim, H.H.; Park, B.O.; Ray, S.S. Magnetic carbonyl iron suspension with organoclay additive and its magnetorheological properties. *Colloids Surf. A Physicochem. Eng. Asp* 2011, 377 (1–3), 103–109.
- (31) Fang, F. F.; Choi, H. J.; Jhon, M. S., Magnetorheology of soft magnetic carbonyl iron suspension with single-walled carbon nanotube additive and its yield stress scaling function. *Colloids Surf. A Physicochem. Eng. Asp* 2009, 351 (1-3), 46-51.
- (32) Lim, S. T.; Cho, M. S.; Jang, I. B.; Choi, H. J.; Jhon, M. S., Magnetorheology of carbonyl-iron suspensions with submicron-sized filler. *IEEE Trans. Magn.* 2004, 40 (4), 3033-3035.
- (33) Fang, F. F.; Choi, H. J.; Seo, Y. Sequential Coating of Magnetic Carbonyl iron Particles with Polystyrene and Multiwalled Carbon Nanotubes and Its Effect on Their Magnetorheology. *ACS Appl. Mater. Interfaces* 2010, 2 (1), 54–60
- (34) Cvek, M.; Mrlik, M.; Ilcikova, M.; Plachy, T.; Sedlacik, M.; Mosnacek, J.; Pavlinek, V. A facile controllable coating of carbonyl iron particles with poly(glycidyl

methacrylate): a tool for adjusting MR response and stability properties. *J. Mater. Chem. C* 2015, 3 (18), 4646–4656.

(35) Liu, Y. D.; Choi, H. J.; Choi, S. B. Controllable fabrication of silica encapsulated soft magnetic microspheres with enhanced oxidation-resistance and their rheology under magnetic field. *Colloids Surf., A* 2012, 403, 133–138.

(36) Sedlacik, M.; Pavlinek, V.; Saha, P.; Svrčinová, P.; Filip, P.; Stejskal, J. Rheological properties of magnetorheological suspensions based on core-shell structured polyaniline-coated carbonyl iron particles. *Smart Mater. Struct.* 2010, 19 (11), 115008.

(37) Han, S.; Choi, J.; Seo, Y. P.; Park, I. J.; Choi, H. J.; Seo, Y. High Performance Magnetorheological Suspensions of Pickering-Emulsion-Polymerized Polystyrene/Fe₃O₄ Particles with Enhanced Stability. *Langmuir* 2018, 34 (8), 2807–2814.

(38) Pu, H. T.; Jiang, F. J.; Yang, Z. L. Preparation and properties of soft magnetic particles based on Fe₃O₄ and hollow polystyrene microsphere composite. *Mater. Chem. Phys.* 2006, 100 (1), 10–14.

(39) Dong, Y. Z.; Piao, S. H.; Choi, H. J., Fe₃O₄/sepiolite magnetic composite particles and their magneto-responsive characteristics. *Colloid Polym Sci* 2018, 296 (1), 11-19.

(40) Pu, H.; Jiang, F., Towards high sedimentation stability: magnetorheological fluids based on CNT/Fe₃O₄ nanocomposites. *Nanotechnology* 2005, 16 (9), 1486-1489

(41) Kim, H.; Kim, S.; Seo, Y., High-Performance Magnetorheological Suspensions of Fe₃O₄-deposited Carbon Nanotubes with Enhanced Stability. *MRS Adv.* 2019, *4* (3-4), 217-224.

Chapter 2. Theoretical Backgrounds

2. 1. Definition of Terms

2. 1. 1. Shear Stress

Shear stress is the stress coplanar with the cross section of materials or fluids. It is shear force per unit cross-sectional area: [1]

$$\tau = \frac{F}{A} \quad (1.1)$$

Here, τ denotes shear stress [Pa], F is applied shear force [N] and A is cross-sectional area of materials

2. 1. 2. Shear Rate

For two plates model, shear rate for a fluid is defined as ratio between velocity of plate divided by distance between two parallel plates: [2]

$$\dot{\gamma} = \frac{v}{h} \quad (1.2)$$

Where $\dot{\gamma}$ is shear rate [1/s], v is velocity of rotational plate [m/s], and h is the gap between

two parallel plates

2. 1. 3. Shear Viscosity

Shear viscosity is the ratio between shear stress and shear rate: [3]

$$\eta = \frac{\tau}{\dot{\gamma}} \quad (1.3)$$

with η is shear viscosity [Pa s], τ is shear stress [Pa] and $\dot{\gamma}$ is shear rate [1/s]. shear viscosity is a measure of resistance to flow when shear stress is applied to fluid.

2. 1. 4. Viscoelastic Behavior

When a material or fluid shows viscous behavior or elastic behavior at the same time, it is called viscoelastic material or fluid. The behavior of viscoelastic materials is described by the combination of viscous part and elastic part which follow Newton's law ($\tau = \eta \dot{\gamma}$) and Hooke's ($\sigma = E \epsilon$) law respectively. [3]

2. 1. 4. 1 Storage Modulus and Loss Modulus

Storage modulus G' is the measure for stored energy during deformation process and represents elastic property of viscoelastic material of fluid. In contrast, loss modulus G'' is the measure of energy dissipated by heat and represents viscous portion. [4] To express Storage modulus and loss modulus with one factor, complex viscosity $G^* = G' + iG''$,

where real part is storage modulus and imaginary part is loss modulus. The ratio between storage modulus and loss modulus (G'/G'') is defined as $\tan\delta$, and this express the degree of damping in materials or fluids. [3,4] When $\tan\delta$ is larger than 1 ($G' > G''$) for a material, solid-like, elastic behavior is more dominant, and when $\tan\delta$ is lower than 1 ($G' < G''$), liquid-like, viscous behavior is more apparent than elastic behavior. [4]

2. 2. Yield Stress of MR Fluids

A rheological property of MR fluids which most directly represents their performance is yield stress. Under sufficiently strong magnetic field and continuous shear condition where thermal, Brownian motion can be neglected, the behavior of MR fluids is governed by field-induced magneto-static interaction and shear-induced hydrodynamic stress. [5,6,7] When magneto-static interaction is dominant over hydrodynamic stress at low shear rate, the chain-like structures consisting of magnetic particles are robust enough and endure the hydrodynamic stress. [6,7] These structures strongly inhibit the flow of suspensions, resulting in yield stress before suspension start to flow. [6] As hydrodynamic stress increases with shear rate and overcomes the magneto-static interaction, it starts to destruct the chain-like structures and induces the flow of MR suspensions. [6] MR suspensions thus exhibit a residual stress, so called yield stress. For MR fluids, two kinds of yield stress, dynamic and static yield stress are defined. Dynamic yield stress is determined at the point where chain-like structures are completely destroyed. [8] And static yield stress of

MR fluids corresponds to shear stress where flow of MR suspensions is induced. [9] When fibril structures are strong enough before complete destruction at high shear rate range, the two yield stresses show very similar value. However, for electrorheological (ER) fluids or some MR fluids whose chain like structures are relatively weak, structure deformation with partial destruction and consecutive reformation occurs. For this case, a large difference between the two yield stresses is observed. [6,11] To predict the dynamic yield stress and static yield stress precisely, several theoretical models have been suggested.

2. 2. 1. Rheological Models for Prediction of Dynamic and Static Yield Stress

A simplest model for prediction of dynamic stress is Bingham fluid model. The relation between shear stress and shear rate in Bingham model is expressed as follows. [8,9]

$$\tau = \tau_{dy}(M) + \eta_{pl}\dot{\gamma} , \quad \tau \geq \tau_{dy}(M) \quad (2.1)$$

$$\dot{\gamma} = 0 , \quad \tau < \tau_{dy}(M)$$

In this model, M is magnetic field strength, $\tau_{dy}(M)$ is dynamic yield stress of MR suspension at the field strength M, $\dot{\gamma}$ is shear rate, and η_{pl} denotes the plastic viscosity of suspensions. Hershel–Bulkley (HB) model has very similar formula with Bingham fluid model, except for power-law dependence to shear rate for HB model. [9]

$$\tau = \tau_0 + m\dot{\gamma}^{n-1} \quad (2.2)$$

Parameter m, and n in this equation are respectively consistency parameter and the power-

law index. The Casson Rheological Model is a structure-based model and describes the flow of viscoelastic model. [7,12-14] When compared to other models, there is a more gradual transition from Newtonian to yield region. The equation for Casson model is as follows

$$\sqrt{\tau} = \sqrt{\tau_y} + \sqrt{\eta\dot{\gamma}} \quad (2.3)$$

with τ_y as Casson yield stress, η as Casson plastic viscosity, and $\dot{\gamma}$ as shear rate. For these three models, dynamic yield stress is obtained through extrapolation of shear stress curve to $\dot{\gamma} = 0$. Thus, these models have a danger that dynamic yield stress value is strongly influenced by the range of shear rates and the rheological model chosen for extrapolation. [6] Also, for plastic fluids like MR fluids in which some parts flow like liquid and while the other parts remain as solid state. [6] Thus, the three models above with a discontinuous transition before and after yielding point is unable to track such randomly distributed yielding surfaces. [13,15] To exclude the discontinuity between low shear rate range and high shear rate range, Papanastasiou proposed a model which includes the flow yield criterion. [13]

$$\tau = \tau_y (1 - 1 - \exp(-n\dot{\gamma})) + \eta\dot{\gamma} \quad (2.4)$$

Also, using Newtonian, Bingham or HM model with the weighting functions of Papanastasiou model $w_i(\dot{\gamma})$, some other cross models were presented, like

$$\tau(\dot{\gamma}) = \tau_{Newton}(\dot{\gamma})w_1(\dot{\gamma}) + \tau_{Bingham}(\dot{\gamma})w_2(\dot{\gamma}) \quad (2.5)$$

$$\tau(\dot{\gamma}) = \tau_{Newton}(\dot{\gamma})w_1(\dot{\gamma}) + \tau_{HB}(\dot{\gamma})w_2(\dot{\gamma}) \quad (2.6)$$

where $w_1(\dot{\gamma}) + w_2(\dot{\gamma}) = 1$. [16] Fitted curves using Papanastasiou model or the cross models were partially agreed at low shear rate range. However, it was unable to predict the static yield stress of MR fluids with those models, and also, there was deviation with experimental data at high shear rate range.

For prediction of static yield stress of MR fluids, Seo and Seo suggested a constitutive modelm Seo-Seo model [8]

$$\tau = \tau_{sy} \left(1 - \frac{(1 - \exp(-a\dot{\gamma}))}{(1 + (a\dot{\gamma})^\alpha)} \right) + \eta_\infty \dot{\gamma} \quad (2.7)$$

where τ_{sy} is the static yield stress η_∞ is the viscosity at high shear rate, a is the time constant (the reciprocal of the critical shear rate for an aligned mesostructure deformation), and α is the power-law index which determine the degree of shear thinning. The term $(1 - \exp(-a\dot{\gamma})) / (1 + (a\dot{\gamma})^\alpha)$ expresses the sudden decrease of shear stress due to partial disruption of the mesostructures. [17] Thus, this model can predict the static yield stress at low shear rate range where the motion of fluid is absent, and describe both flow behavior at low shear rate range with local minimum in shear stress curve and the behavior at high shear rate range. [17,18] In addition, depending on specific condition, Seo-Seo model also presents Newtonian fluids ($\tau_{sy} = 0$), Bingham model ($a = 0$), BH model ($a = 0$, $\eta_\infty = m\dot{\gamma}^{n-1}$) and De Kee-Turcotte model ($\alpha = 0$, $a \neq 0$). [8,10,12,13,19]

When chain-like structures are robust and stress variation with structural change is small, dynamic and static yield stress values are very similar to each other. However, if field-

induced polarization interaction between magnetic particles is weak, the structural change occurs strongly, thus the difference between dynamic and static yield stress can be very large. [10,15]

2. 2. 2. Yield Stress Dependency on the Magnetic Field Strength

Although the yield stress of a MR fluids is affected by several factors, the most important factor is the strength of magnetic field. The field-dependence of yield stress is expressed with power-law dependence ($\tau_y \propto H^n$), and the power-law index n become different with magnetic field strength range. [7,20-24] For a linear magnetic materials with low field strength or a magnetic materials with low permeability, n has a value of 2, and yield stress has quadratic dependence to field strength while intermediate 3/2 power law dependence was observed at intermediate field strength range. [7,20,21] Similar field strength-dependence was also observed for ER fluids where $\tau_y \propto H^2$ at low electric field strength and $\tau_y \propto H^{1.5}$ at high electric field strength. [22]

Choi et al. proposed a single hybrid equation which collapse the yield stress data at all field strength range in to a single curve. [23]

$$\tau_y(H_0) = \alpha H_0^2 \left(\frac{\tanh \sqrt{H_0/H_c}}{\sqrt{H_0/H_c}} \right) \quad (2.8)$$

Here, α is a constant related to the physical parameter of the material like susceptibility of the fluid and particle volume fraction, and H_c is the critical field strength where field-

dependence change from quadratic to 3/2 power-law dependence. At low and high field strength, the equation describes the limiting behavior as follows

$$\tau_y \propto \begin{cases} \alpha H_0^2, & H_0 \ll H_c \\ \alpha \sqrt{H_c} H_0^{3/2}, & H_0 \gg H_c \end{cases} \quad (2.9)$$

To reduce cumbersomeness in the separation of two different regions, Seo proposed a simpler equation with one parameter m' . [20]

$$(H_0) = \alpha H_0^{3/2} \left(1 - \exp \left(-m' \sqrt{H_0} \right) \right) \quad (2.10)$$

This model shows that this nonlinear function fits the field dependency of the MR fluid's (or the ER fluid's) yield stress regardless of applied magnetic (or electric) field strength with limiting behaviors at low and high magnetic field strength field as follows.

$$\tau_y \propto \begin{cases} \alpha m' \propto H_0^2, & H_0 \ll H_c \\ \alpha H_0^{3/2}, & H_0 \gg H_c \end{cases} \quad (2.11)$$

If equation (2.10) is normalized with H_c and when $\tau_y = \alpha H_c^{3/2}$, a dimensionless equation can be obtained

$$\hat{\tau} = \hat{H}^{3/2} \left(1 - \exp \left(-m \sqrt{\hat{H}} \right) \right) \quad (2.12)$$

where $\hat{H} = H/H_c$ and $m = m' \sqrt{H_c}$.

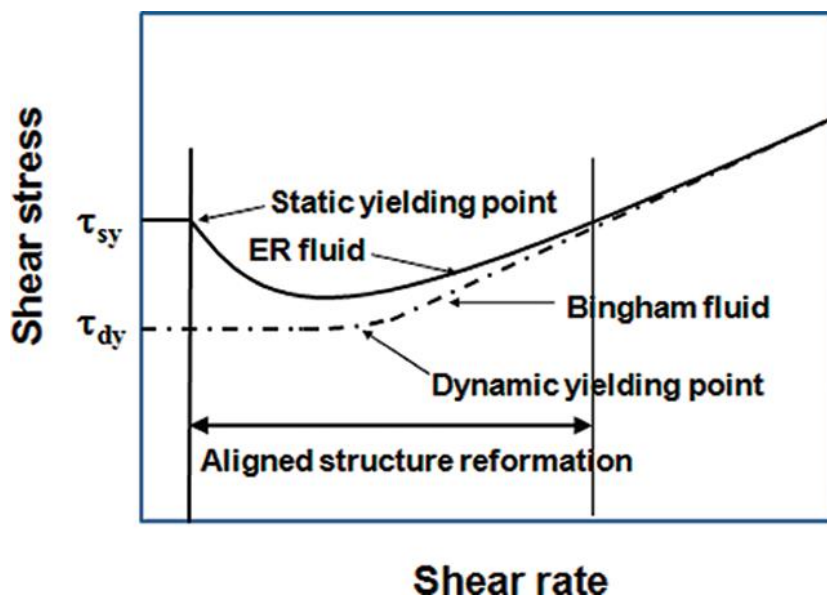


Figure 2. 1. Static and dynamic yield stress of MR fluids

2. 3. Mechanism of Structure Evolution

As stated, under strong magnetic field, the behavior of MR fluid is determined by field-induced magnetostatic polarization force and shear-induced hydrodynamic force. Then, non-dimensional rheological properties of MR fluids should depend only the ratio between polarization force and hydrodynamic force. [23] This was first applied for analysis of ER fluids' rheological properties by Marshall et al. [25] They introduced the concept of Mason number, which is the ratio between the magnitude of electrostatic polarization force and hydrodynamic force and used it as a single independent variable for the analysis. [25] After, Daniel J. Klingenberg applied Mason number for the analysis of MR fluids' rheological fluids. Mason number for MR fluids is expressed as [26]

$$Mn = 8\eta_0\dot{\gamma}/2\mu_0\mu_c\beta^2M^2 \quad (2.13)$$

Where η_0 is the medium viscosity, $\dot{\gamma}$ is the shear rate, β is the magnetic contrast factor ($= (\mu_p - \mu_c)/(\mu_p + 2\mu_c)$), μ_p is the relative magnetic permeability of the particles, μ_c is the relative magnetic permeability of the liquid medium phase), $\mu_0 = 4\pi \times 10^{-4} N/A^2$ is the vacuum permeability, and M is the magnetic field strength. The numerator term $\eta_0\dot{\gamma}$ corresponds to the hydrodynamic force under continuous shear and the denominator including M^2 is proportional to the magnetic polarization force. [27] The apparent viscosity of suspension is defined as $\eta_{app} = \tau/\dot{\gamma}$ and proportional to the reciprocal of M_n . [15,28] Thus, for viscosity curve against shear rate, by rescaling horizontal axis (shear rate) by M^2

and the vertical axis (viscosity) by a suitable factor $s(M)$, a master curve can be achieved and behavior of different MR fluids can be compared. To obtain a suitable form a $s(M)$, Fossum et al. proposed a power-law equation of the magnetic field strength [15]

$$\tau (M) = (M/M_c)^\alpha f(\dot{\gamma}/M^2) \quad (2.14)$$

where the functional relation f represents the master curve. If the behavior of different MR fluids is same, curves for dimensionless apparent viscosities of the MR fluids would collapse onto as single curve with the rescaling process. At low M_n , the slope of $\log((\eta_{app}/\eta_c)(M/M_c))$ versus $\log(\dot{\gamma}/M^2)$ curve is -1, whereas the curve smoothly approaches to unity with increasing M_n due to destruction of chain-like structures.

References

- (1) Hibbeler, R. C., *Mechanics of Materials 5th ed.* Prentice Hall, New jersey 2003.
- (2) Ron. D., *Chemical Engineering Fluid Mechanics 2nd ed.* CRC Press, Boca Raton, 2001, p. 64.
- (3) Robert. J. Y and Peter. A. L, *Introduction of polymers 3rd ed.* CRC Press, Boca Raton, 2011.
- (4) Mark. A. M. and Krishan. K. C., *Mechanical Behavior of Materials*, Cambridge University Press, Cambridge 1999, 98-103
- (5) Chuah, W. H.; Zhang, W. L.; Choi, H. J.; Seo, Y., Magnetorheology of core-shell structured carbonyl iron/polystyrene foam microparticles suspension with enhanced stability. *Macromolecules* 2015, 48 (19), 7311-7319.
- (6) Seo, Y. P.; Han, S.; Choi, J.; Takahara, A.; Choi, H. J.; Seo, Y., Searching for a stable high-performance magnetorheological suspension. *Adv. Mater.* 2018, 30 (42), 1704769.
- (7) Seo, Y. P.; Kwak, S.; Choi, H. J.; Seo, Y., Static yield stress of a magnetorheological fluid containing Pickering emulsion polymerized Fe₂O₃/polystyrene composite particles. *J. Colloid Interface Sci.* 2016, 463, 272-278.
- (8) Seo, Y. P.; Seo, Y., Modeling and analysis of electrorheological suspensions in shear flow. *Langmuir* 2012, 28 (6), 3077-3084.

- (9) Farjoud, A.; Vahdati, N.; Fah, Y. F., Mathematical model of drum-type MR brakes using Herschel-Bulkley shear model. *J. Intell. Mater. Syst. Struct.* 2008, *19* (5), 565-572.
- (10) Seo, Y. P.; Choi, H. J.; Lee, J. R.; Seo, Y., Modeling and analysis of an electrorheological flow behavior containing semiconducting graphene oxide/polyaniline composite particles. *Colloids Surf. A Physicochem. Eng. Asp.* 2014, *457*, 363-367.
- (11) Han, S.; Choi, J.; Seo, Y. P.; Park, I. J.; Choi, H. J.; Seo, Y., High-performance magnetorheological suspensions of pickering-emulsion-polymerized polystyrene/Fe₃O₄ particles with enhanced stability. *Langmuir* 2018, *34* (8), 2807-2814
- (12) De Kee, D.; Turcotte, G. Viscosity of biomaterials. *Chem. Eng. Commun.* 1980, *16*, 273-282
- (13) Papanastasiou, T.C. Flow of materials with yield. *J. Rheol.* 1987, *31*, 385-404
- (14) Folayan, J. A.; Anawe, P. A. L.; Abioye, P. O.; Elehinafe, F. B., Selecting the most appropriate model for rheological characterization of synthetic based drilling mud. *nt. J. Appl. Eng. Res.* 2017, *12* (18), 7614-7649.
- (15) Parmar, K.; Méheust, Y.; Schjelderupsen, B.; Fossum, J., Electrorheological suspensions of laponite in oil: rheometry studies. *Langmuir* 2008, *24* (5), 1814-1822.
- (16) Ghaffari, A.; Hashemabadi, S. H.; Ashtiani, M., A review on the simulation and modeling of magnetorheological fluids. *J. Intell. Mater. Syst. Struct.* 2015, *26* (8), 881-904.

- (17) Seo, Y. P.; Han, S.; Kim, J.; Choi, H. J.; Seo, Y., Analysis of the flow behavior of electrorheological fluids containing polypyrrole nanoparticles or polypyrrole/silica nanocomposite particles. *Rheol. Acta* 2020, 59 (6), 415-423.
- (18) Han, S.; Choi, J.; Kim, H.; Kim, S.; Seo, Y. In *Static yield stress of a magnetorheological fluid containing pickering emulsion polymerized Fe₃O₄/polystyrene composite particles*, AIP Conf. Proc., AIP Publishing LLC: 2019; p 140001.
- (19) Nicholas, D.T.; Noorman, M.W. Volume-constrained optimization of magnetorheological and electrorheological valves and dampers. *Smart Mater. Struct.* 2004, 13, 1303-1313
- (20) Seo, Y. A new yield stress scaling function for electrorheological fluids. *J. Nonnewton. Fluid. Mech.* 2011, 166, 241-243
- (21) Sedlacik, M.; Pavlinek, V.; Saha, P.; Svrcinova, P.; Filip, P.; Stejskal, J. Rheological properties of magnetorheological suspensions based on core-shell structured polyaniline-coated carbonyl iron particles. *Smart Mater. Struct.* **2010**, 19, 115008.
- (22) Davis, L.C.; Ginder, J.D. Science and technology of electrorheological materials. *Progress in Electrorheology*, Plenum, New York 1995, p. 107
- (23) Choi, H.J.; Cho, M.S.; Kim, J.W.; Kim, C.A.; Jhon, M.S. A yield stress scaling function for electrorheological fluids. *Appl. Phys. Lett.* 2001, 78, 3806-308.
- (24) Seo, Y.P.; Choi, H.J.; Seo, Y. A simplified model for analyzing the flow behavior of electrorheological fluids containing silica nanoparticle-decorated polyaniline nanofibers. *Soft Matter* 2012, 8, 4659-4663.

- (25) Marshall, L.; Zukoski, C. F.; Goodwin, J. W., Effects of electric fields on the rheology of non-aqueous concentrated suspensions. *J. Chem. Soc., Faraday Trans. I* 1989, 85 (9), 2785-2795.
- (26) Klingenberg, D.J.; Ulieny, J C.; Golden, M.A. Mason numbers for magnetorheology. *J. Rheol.* 2007, 51, 883-893.
- (27) De Vicente, J.; Klingenberg, D. J.; Hidalgo-Alvarez, R., Magnetorheological fluids: a review. *Soft matter* 2011, 7 (8), 3701-3710.
- (28) Becnel, A. C.; Sherman, S.; Hu, W.; Wereley, N. M., Nondimensional scaling of magnetorheological rotary shear mode devices using the Mason number. *J. Magn. Magn. Mater.* 2015, 380, 90-97.

Chapter 3. Suspensions of Hollow Polydivinylbenzene Nanoparticles Decorated with Fe₃O₄ Nanoparticles as Magnetorheological Fluids for Microfluidics Applications

3. 1. Introduction

Magnetorheological (MR) fluids, which are suspensions of magnetic particles in a magnetically insulating fluid, react to the applied magnetic field. [1,2] Once the external magnetic field is applied, the randomly dispersed particles can form fibril-like structures (mesostructures) due to the interaction between magnetic dipoles of magnetic particles. [3,4] The formation of mesostructures within less than a few milliseconds in response to the applied magnetic field results in a sudden increase in the viscosity of the suspensions by 3–4 orders of magnitude. [1,5] The reverse structural change occurs immediately when the applied field is off. These forward and reverse structural changes occur on the order of milliseconds and are therefore a kind of smart material. [4] These field-responsive properties of MR fluids make them useful in a variety of systems. They can be used for small systems such as haptic devices, vehicle suspensions, rotor dampers, power steering pumps, and so on. [3,6] MR suspension systems are also found in large-scale damper systems for large buildings to reduce the impact of earthquakes and under bridges to mitigate vibrations caused by gusts. [7–9]

Despite substantial advances in commercialization, MR fluids have long-term stability issues that significantly limit their usefulness. [1,10–12] The long-term stability problem is mainly due to the density mismatch between heavy magnetic particles (Fe_2O_3 , Fe_3O_4 , carbonyl iron, etc.) and light carrier medium (silicone oil). To overcome this serious drawback, many efforts have been made such as the addition of additives or surfactants or fillers, the use of viscoplastic medium as a carrier, or application of protective layers like polymer or passivation layer on the magnetic particles. [13–16] Among these methods, the coating of magnetic particles with a protective light layer has been shown to be an efficient strategy for improving the long-term stability of MR fluids. [1,2,16,17] This strategy can reduce the density mismatch between the magnetic particles and the fluid medium for improving the long-term stability. [2,16–19] Another effective method is to prepare core–shell type particles which is the encapsulation of low-density polymeric materials with nanometer-size magnetic particles. One method of making such particles is the Pickering-emulsion polymerization method using inorganic solid particles as surfactants. [5,20] In a previous study, PS/ Fe_2O_3 core–shell particles were prepared by Pickering-emulsion polymerization using about 50–100 nm size Fe_2O_3 nanoparticles as a surfactant. [20] The density of PS/ Fe_2O_3 core–shell particles was significantly reduced (from 5.12 g/cm^3 for Fe_2O_3 particles to 2.6 g/cm^3), improving the stability of the suspensions. More recently, our group synthesized foamed polystyrene/ Fe_3O_4 (f-PS/ Fe_3O_4) particles via the Pickering emulsion polymerization method using Fe_3O_4 nanoparticles as a surfactant followed by foaming of the PS core with supercritical carbon dioxide. [5] Because the Fe_3O_4 particles have a higher magnetization saturation value, the f-PS/ Fe_3O_4 suspension

performed better than the Fe_2O_3 suspension. The foamed particles showed very low density (1.82 g/cm^3) upon incorporation of pores in the PS core and high yield stress with the use of Fe_3O_4 instead of Fe_2O_3 . More importantly, the low density and rough surface of f-PS/ Fe_3O_4 provide much better stability than the Fe_3O_4 suspension system. [5]

Hollow particles have a large cavity inside a shell layer or multiple shells. Because of their unique structure, hollow particles have been used for targeting drug delivery systems and nanoreactor systems. [21–24] Magnetic hollow particles can impart long-term stability due to the low density of the particles which comes from the cavity. Pu et al. synthesized hollow PS/ Fe_3O_4 microspheres using SiO_2 microspheres as templates. [25] The hollow PS/ Fe_3O_4 exhibited much lower density than pure Fe_3O_4 and iron particles because of the large cavity, resulting in the improved stability of MR fluids. However, the particles had a wide particle size distribution (150–400 nm). Moreover, the aggregation mechanism and MR properties such as yield stress, storage modulus, and loss modulus of the suspension under magnetic field were not investigated, and the stability of hollow PS/ Fe_3O_4 was observed to last only 3 h. Thus, it is still necessary to investigate the details of MR performance and long-term stability of MR fluids containing hollow magnetic particles with a narrow size distribution.

In this work, hollow polydivinylbenzene@ Fe_3O_4 (h-PDVB@ Fe_3O_4) nanoparticles were synthesized by using SiO_2 particles as a template. Hollow PDVB particles were prepared by coating PDVB on modified SiO_2 via a distillation–precipitation polymerization process followed by dissolution of SiO_2 . Next, Fe_3O_4 nanoparticles were deposited on the surface

of hollow PDVB particles by solution chemistry. This process resulted in hollow magnetic particles with a relatively narrow size distribution. Because of their hollow structure, h-PDVB@Fe₃O₄ particles showed very low density despite its high Fe₃O₄ nanoparticle content. The MR properties of h-PDVB@ Fe₃O₄ were investigated by dispersing them in silicone oil. Dynamic and static yield stress values of the suspensions were investigated by using the Bingham and Seo–Seo model. [26,27] Though the particle density is similar to each other, the MR performance comparison of the h-PDVB@Fe₃O₄ (10–20 nm) suspension and the f-PS/Fe₃O₄ (50–100 nm) suspension shows a difference in yield stress values at low magnetic field strength and high magnetic field strength. The particle aggregation mechanism was also investigated by probing the universal yield stress behaviors with a Mason plot. [28,29] Because of the reduced density mismatch through the hollow structure, the h-PDVB@ Fe₃O₄ suspension exhibited significantly improved long-term stability compared to the Fe₃O₄ suspension.

3. 2. Experimental Section

3. 2. 1. Synthesis of Hollow Polydivinylbenzene (h-PDVB) Particles

Figure 3.1 shows the synthetic scheme of hollow polydivinylbenzene (h-PDVB) and hollow PDVB/Fe₃O₄ (h-PDVB/Fe₃O₄) nanoparticles. Hollow polydivinylbenzene nanoparticles were synthesized by a well-known method for the synthesis of monodisperse polymer particles or core–shell particles without using a surfactant or a stabilizer:

distillation–precipitation polymerization of divinylbenzene (DVB, 80% technical grade, Sigma-Aldrich, USA). We used PDVB instead of polystyrene since it is easier to get the uniform size particles. [30–34] To modify the SiO₂ surface with 3-methacryloxypropyltrimethoxy silane (MPS, 97% purity, Alfa-Aesar, USA), SiO₂ particles (6 g) were dispersed in ethanol/H₂O (480 mL/120 mL) by using a homogenizer. Subsequently, the mixture was placed in a 1000 mL three-neck round-bottom flask. Thereafter, ammonium hydroxide solution (12 mL) (28 wt % in H₂O, Daejung, Korea) and MPS (12 mL) were injected into the mixture. The reaction was then continued at 25 °C for 48 h. The product was collected by centrifugation, washed three times with excess ethanol and water, and then dried in a vacuum oven at room temperature. MPS-modified SiO₂ particles (1 g) were dispersed in acetonitrile (400 mL) (purity of 99.5%, Daejung, Korea), ultrasonicated, and homogenized. The solution was placed in a 1000 mL round-bottomed three-necked flask with a distillation head. DVB (4 mL) and 2,2'-azobis(isobutyronitrile) (0.8 mL) (AIBN solution, 12 wt % in acetone, Sigma-Aldrich, USA) were injected into the mixture, and the system was heated to boiling in 20 min. The reaction was allowed to proceed under an argon atmosphere, and 200 mL of acetonitrile was distilled over 80 min. After cooling to room temperature, the product was collected by centrifugation and washed three times with excess acetonitrile and ethanol to remove the excess initiator and monomer. Finally, the washed product was dried in a vacuum oven at room temperature. Hollow h-PDVB nanoparticles were obtained by etching SiO₂ with hydrogen fluoride (HF). SiO₂/PDVB particles (4.2 g) were immersed in the 3:1 mixture of hydrogen fluoride (450 mL) (48%, Alfa-Aesar, USA) and ethanol (150 mL) solution. The etching process was

continued for 4 h at 25 °C. The final product was collected by centrifugation, then washed five times with distilled water to remove SiF₄ and excess HF, and finally dried in a vacuum oven at room temperature. The TGA results in Figure 3.2 showed 3.9% of residual weight in h-PDVB particle at 800 °C, which indicates that there are some SiO₂ in PDVB shell that could block the pores in shell layer. Yoon et al. synthesized SiO₂/TiO₂ hollow nanorods by synthesizing SiO₂/TiO₂ core-shell nanorods first, followed by dissolution of SiO₂. [35] They found the existence of SiO₂ in TiO₂ shell layer due to redeposition of SiO₂, and the density measured with a pycnometer was lower for hollow nanorods than core-shell nanorods. Although the etchant for SiO₂ in their study was different than our study, it is possible to expect that residual SiO₂ blocks the pores in PDVB shell layer, leading to low density values for h-PDVB@Fe₃O₄ particles measured with a helium pycnometer.

3. 2. 2. Deposition of Fe₃O₄ onto Hollow PDVB Particles

Two types of hollow PDVB@Fe₃O₄ particles (h-PDVB@Fe₃O₄) with different Fe₃O₄ content were prepared by depositing Fe₃O₄ nanoparticles on h-PDVB. h-PDVB particles (1.2 g), polyvinylpyrrolidone (1.2 g) (PVP, Mw ~ 55000, Sigma-Aldrich, USA), and sodium dodecylbenzenesulfonate (1.2 g) (SDBS, technical grade, Sigma-Aldrich, USA) were dispersed in distilled water (120 mL) by using a homogenizer. The solution was placed in a 250 mL three-necked round-bottom flask, and FeCl₃·6H₂O (4.32 and 8.64 g) and FeSO₄·7H₂O (2.22 and 4.45 g) were put into the flask. The flask was then heated to 70 °C, and a 5 M sodium hydroxide (NaOH, purity higher than 97%, Daejung, Korea)

solution (10 and 20 mL) was slowly injected. The reaction ($\text{FeSO}_4 \cdot 7\text{H}_2\text{O} + 2\text{FeCl}_3 \cdot 6\text{H}_2\text{O} + 8\text{NaOH} = \text{Fe}_3\text{O}_4 + 6\text{NaCl} + \text{Na}_2\text{SO}_4 + 23\text{H}_2\text{O}$) proceeded for 4 h at the temperature under Ar atmosphere. The solution was then cooled to room temperature. The resulting product was collected by using a magnet, washed five times with excess distilled water and ethanol to remove excess PVP, SDBS, and NaOH, and then dried in a vacuum oven at room temperature.

3. 2. 3. Characterization

The content of Fe_3O_4 in h-PDVB@ Fe_3O_4 particles was measured by using thermogravimetric analysis (TGA; Mettler Toledo TGA DSC 1, Mettler Toledo, OH, USA). TGA measurements were performed from 25 to 800 °C with a heating rate of 10 °C/min under a nitrogen atmosphere. The densities of Fe_3O_4 and h-PDVB@ Fe_3O_4 were measured by using a helium pycnometer (AccuPyc 1330, Micromeritics Instrument Corporation, Norcross, GA). The surface morphology of the sample was observed with a scanning electron microscope (SEM; JSM-7600F, JEOL, Tokyo, Japan) and a transmission electron microscope (TEM; Tecnai F20, FEI, USA and Themis Z, ThermoFisher, USA). The crystal structures and domain size of magnetic particles were examined with an X-ray diffractometer (XRD:D8-Advance, Bruker, USA). Using a vibrating sample magnetometer (VSM; VSM-7410, Lake Shore Cryotronics, USA) over the range of -10 to 10 kOe, we measured the saturation magnetization of each sample. The MR fluids were prepared by dispersing the particles in silicone oil (KF-96, 10 cS, Shin Etsu, Japan) at a particle

concentration of 10 vol %. A rotational rheometer (Physica MCR301, Stuttgart, Germany) equipped with a magnetic generator (Physica MRD 180, Stuttgart, Germany) was used to measure the magnetorheological properties of each MR fluid. A parallel plate with a diameter of 20 mm was used with a gap distance of 1 mm. The tests were done at room temperature. Finally, Turbiscan (Classic MA2000, Formulation, France) was used to test the sedimentation stability of the MR fluids.

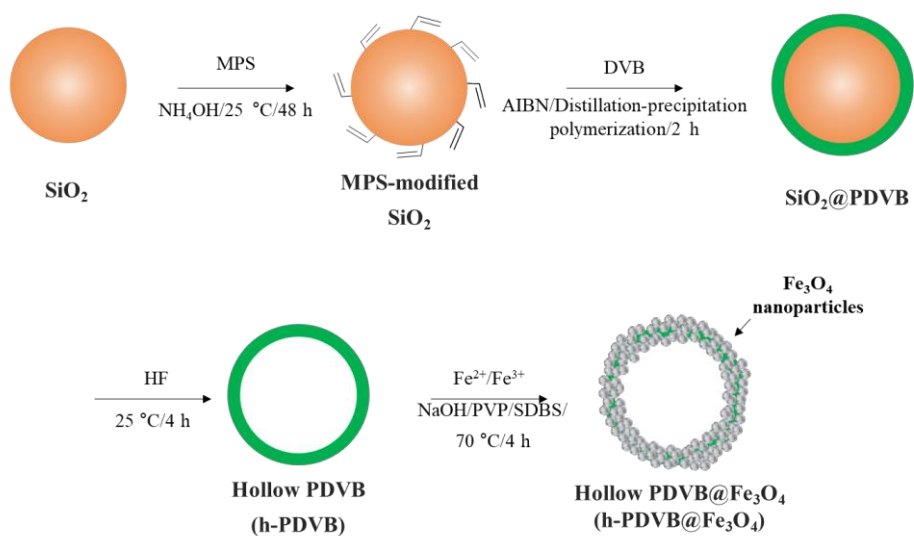


Figure 3. 1. Schematic diagram for the synthesis of h-PDVB@ Fe_3O_4 particles.

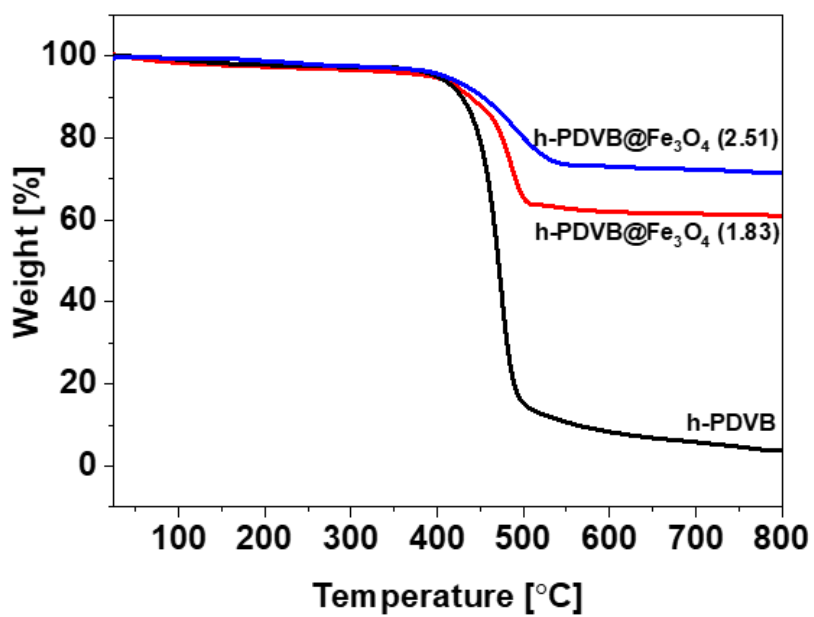


Figure 3. 2. TGA curves of h-PDVB, h-PDVB@Fe₃O₄ ($\rho = 2.51\text{g/cm}^3$) and h-PDVB@Fe₃O₄ ($\rho = 1.83\text{g/cm}^3$).

3. 3. Results and Discussion

3. 3. 1. Morphologies and Structures

The densities of pure Fe₃O₄ and two types of h-PDVB@Fe₃O₄ were measured with a helium pycnometer. The densities of two h-PDVB@Fe₃O₄ particles were 1.83 and 2.51 g/cm³, respectively, which are much lower than that of pure Fe₃O₄ ($\rho = 4.52 \text{ g/cm}^3$). The low density of h-PDVB@Fe₃O₄ is attributed to the cavity in the hollow structure. The Fe₃O₄ content in h-PDVB@Fe₃O₄ particles was measured with TGA from 25 to 800 °C under a N₂ atmosphere. TGA curves of h-PDVB, h-PDVB@Fe₃O₄ (1.83), and h-PDVB@Fe₃O₄ (2.51) are shown in Figure 3.2. The residual weight of h-PDVB at 800 °C was about 3.9%, which means that MPS-modified SiO₂ core was almost completely removed by HF. In contrast, the residual weight of h-PDVB@Fe₃O₄ (1.83) and h-PDVB@Fe₃O₄ (2.51) at 800 °C was about 59.5% and 70.4%. Thus, the contents of Fe₃O₄ in h-PDVB@Fe₃O₄ (1.83) and h-PDVB@Fe₃O₄ (2.51) were estimated to be about 59.5% and 70.4%, respectively. Because of the large volume fraction of the cavity, h-PDVB@Fe₃O₄ particles showed quite low density although they contained high contents of Fe₃O₄.

Figure 3.3 (a) shows that the MPS-modified SiO₂ particles have a very smooth surface. After coating the surface with PDVB, the surface of SiO₂@PDVB becomes relatively rough, but SiO₂@PDVB submicrometer spheres have a relatively narrow size distribution. [30–34] After etching the SiO₂ core, h-PDVB particles retained their spherical shape, and no shrinkage or collapse of the PDVB shell was observed Figure 3.3 (c)). This means that

cross-linked PDVB shell is strong enough to maintain the spherical shape. The SEM image of h-PDVB@Fe₃O₄ (1.83) (Figure 3.3 (d)) shows that Fe₃O₄ nanoparticles with a size of 10–20 nm are deposited on the surface of PDVB shell. With the deposition of Fe₃O₄, the surface became rough and bumpy. The thickness of h-PDVB from the TEM image (Figure 3.3 (e)) was approximately 59 ± 5 nm. TEM images of h-PDVB@Fe₃O₄ particles (Figure 3.3 (f),(g)) demonstrate that Fe₃O₄ nanoparticles are well deposited on the surface of h-PDVB for both h-PDVB@Fe₃O₄ (1.83) and h-PDVB@Fe₃O₄ (2.51). The Fe₃O₄ deposited particle size was 670 ± 33 and 690 ± 40 nm for PDVB@Fe₃O₄ (1.83) and h-PDVB@Fe₃O₄ (2.51), respectively. They have a relatively narrow particle size distribution compared to f-PS/Fe₃O₄ particles having a similar density. [5] More uniform size particles induce easier aggregation under the same magnetic field and hence better MR performance. [36–38] The deposition of Fe₃O₄ nanoparticles makes the surface of h-PDVB@Fe₃O₄ rougher compared to SiO₂@PDVB and h-PDVB particles.

The XRD patterns of cubic and spherical Fe₃O₄ and hPDVB@Fe₃O₄ are shown in Figure 3.4. To define the iron species, the XRD pattern of commercial cubic Fe₃O₄ used for fPS/Fe₃O₄ was compared with that of Fe₃O₄ and h-PDVB@Fe₃O₄ particles.⁵ For all samples, diffraction peaks corresponding to [220], [311], [222], [400], [422], [511], and [440] planes of Fe₃O₄ were observed. This indicates successful synthesis of Fe₃O₄ in the presence of h-PDVB during the reaction. The average crystallite sizes were calculated with the Scherrer formula ($D = K\lambda/(\beta\cos\theta)$) where K = shape factor, λ = wavelength (0.154 nm), β = line broadening at 1/2 the maximum intensity (rad), and θ = Bragg angle. The broad

peaks of the spherical MNPs compared to the sharp peaks of the cubic MNP indicate that the crystallite size of the cubic sample is larger. The crystallite sizes were 64, 13, 15, and 13 nm for cubic Fe_3O_4 , Fe_3O_4 (4.52), h-PDVB@ Fe_3O_4 (1.83), and h-PDVB@ Fe_3O_4 (2.51), respectively.

Figure 3.5 shows the optical microscope images of an MR fluid based on h-PDVB@ Fe_3O_4 (1.83) with the magnetic field off and on. Upon application of a magnetic field, the particles showed a rapid transition from a dispersed state to fibril-like structures along the direction of the applied magnetic field. These aligned structures span the gap of flow channel and thus inhibit the fluid flow. When the magnetic field is off, the particles returned to the dispersed state very rapidly.

Figure 3.6 shows the magnetic hysteresis curves of pure Fe_3O_4 and h-PDVB@ Fe_3O_4 suspensions in the magnetic field range of -10 to 10 kOe. All samples exhibit little hysteresis behavior with high saturation magnetization values (M_s) and low coercive field. The M_s values for pure Fe_3O_4 , h-PDVB@ Fe_3O_4 (1.83), and h-PDVB@ Fe_3O_4 (2.51) were 78, 41, and 52 emu/g, respectively. h-PDVB@ Fe_3O_4 hollow particles have large, nonmagnetic h-PDVB and accordingly low magnetic Fe_3O_4 content compared to pure Fe_3O_4 . This results in weakened interaction between magnetic particles and lower M_s values for h-PDVB@ Fe_3O_4 particles. h-PDVB@ Fe_3O_4 (2.51) with higher Fe_3O_4 content shows a higher M_s value than that of h-PDVB@ Fe_3O_4 (1.83). The coercive field values were not much different from each other.

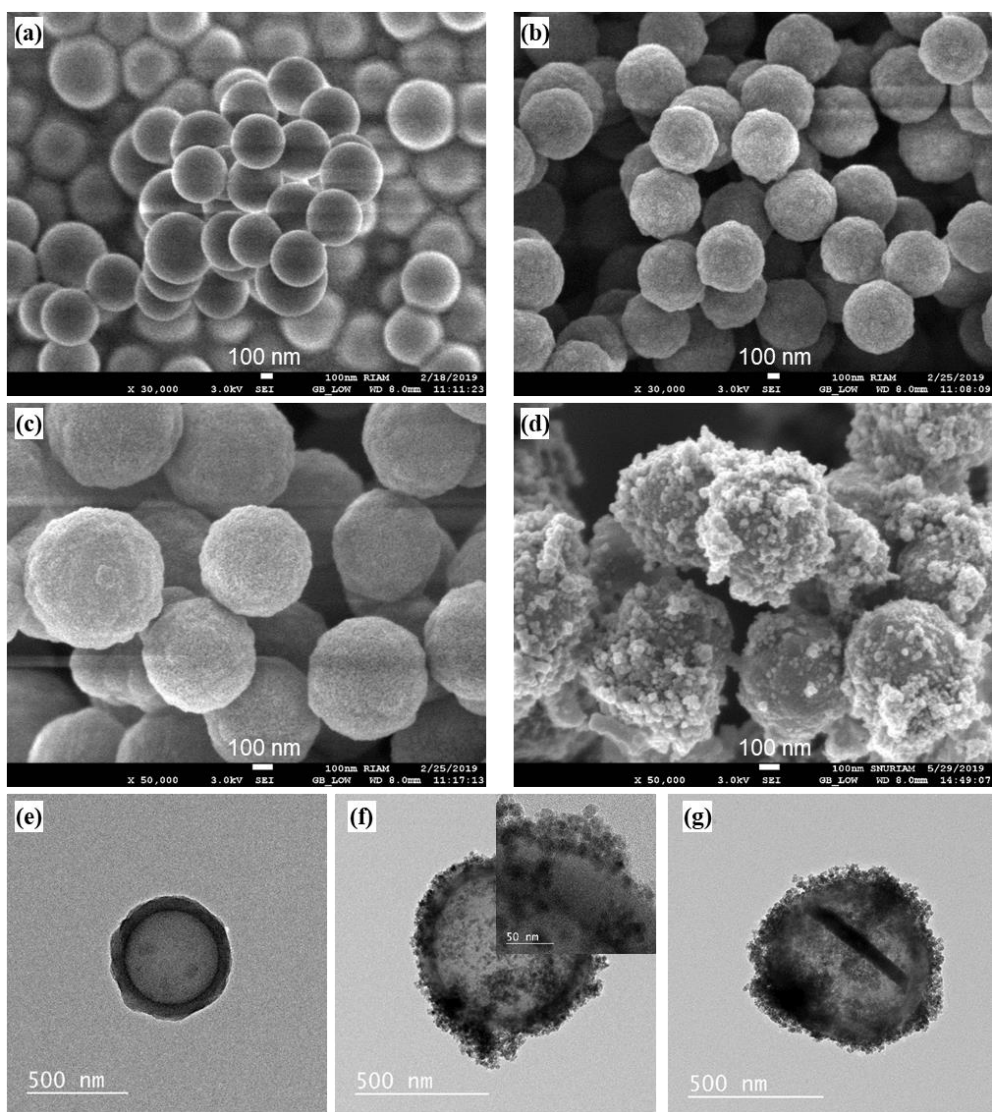


Figure 3.3. SEM images of (a) MPS-modified SiO₂, (b) SiO₂/PDVB, (c) h-PDVB, and (d) h-PDVB@Fe₃O₄ (1.83), TEM images of (e) h-PDVB, (f) h-PDVB@Fe₃O₄ (1.83) (the inset showed magnified view of the particle surface), and (g) h-PDVB@Fe₃O₄ (2.51)

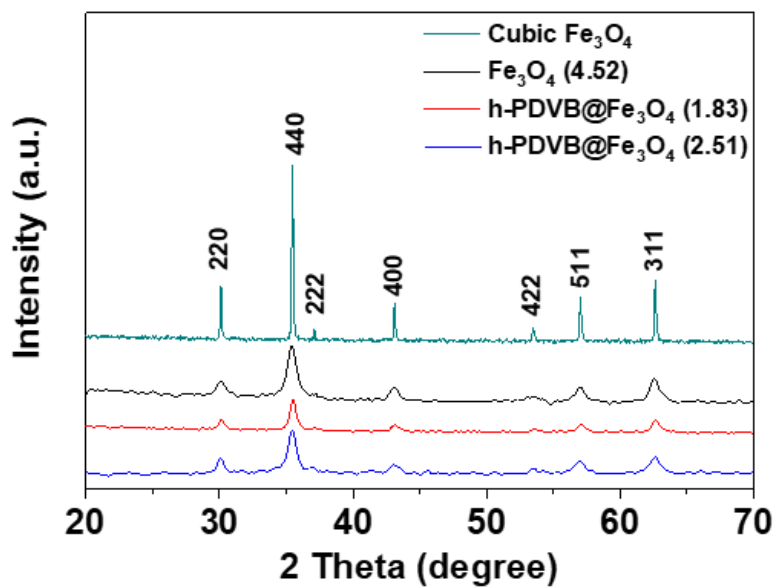


Figure 3. 4. XRD patterns for Fe_3O_4 and $\text{h-PDVB@Fe}_3\text{O}_4$

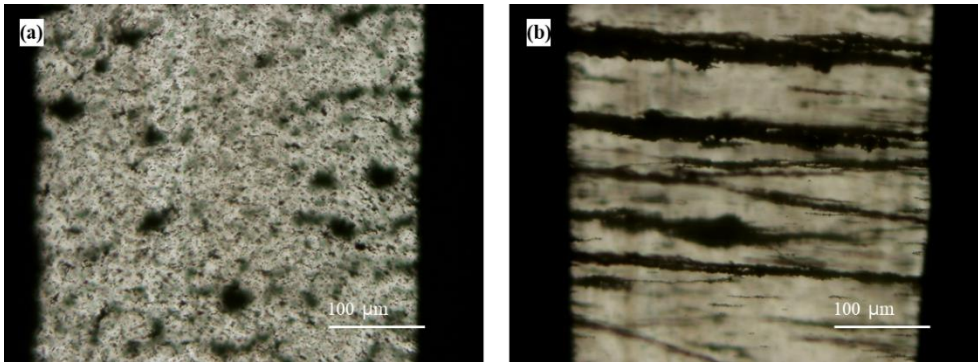


Figure 3. 5. Optical microscopic images of microstructural change for h-PDVB@Fe₃O₄ (1.83) suspension (a) before and (b) after the application of external magnetic field.

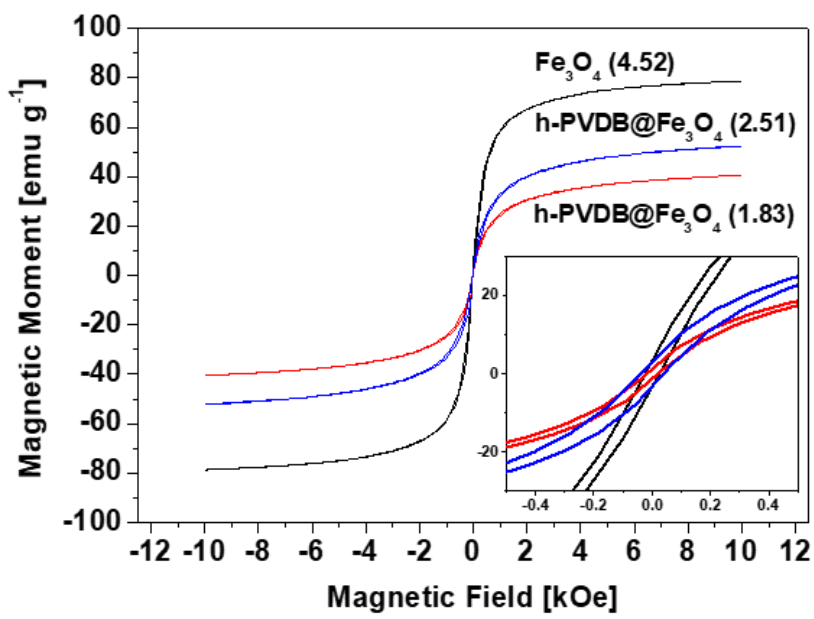


Figure 3. 6. VSM data for pure Fe₃O₄, h-PDVB@Fe₃O₄ (1.83) and h-PDVB@Fe₃O₄ (2.51) particles (1 Oe = 10³/4π A/m).

3. 3. 2. Magnetorheological Properties

Oscillatory tests (amplitude and frequency sweep) were conducted to investigate the viscoelastic behavior of the suspensions. Amplitude measurement results in Figure 3.7 (a) describing the change in storage modulus as a function of strain from 0.001 to 100% are presented. The storage modulus increased with the magnetic field strength due to the enhanced dipole–dipole interaction between magnetic particles. In the strain range from 0.001 to 0.02%, a stable plateau area was observed for both magnetic field strengths (86 and 343 kA/m). In this region where MR suspensions exhibited viscoelastic behavior, the storage modulus was independent of the applied strain due to mesostructures. The mesostructures formed under the applied magnetic field were not disturbed by the applied strain. As the strain amplitude increased, the mesostructures began to fall apart and the storage modulus gradually decreased. The frequency sweep measurement of the storage modulus and the loss modulus is illustrated in Figure 3.7 (b). For all fluids, the storage moduli were an order of magnitude higher than the corresponding loss moduli. This indicates the dominance of solid-like elastic properties of MR fluids under magnetic field due to the formation of the mesostructures. [34] Despite of nano-sized Fe_3O_4 particles on the surface of PDVB shell, the interaction between h-PDVB@ Fe_3O_4 particles was strong enough to maintain the fibril-like mesostructures over an entire frequency range.

The shear stress of MR fluids as a function of shear rate at two different magnetic field strengths (86 and 343 kA/m) is presented in Figure 3.8 (a). In general, the mesostructures at low shear rate are strong enough to withstand the applied shear stress, so that the shear

stress of each MR suspension remains at constant value. Sometimes shear stress decreases and increases again in the mid-shear rate region due to the destruction and re-forming of fibril-like structures. [26] However, such a phenomenon is not observed for all three suspensions at both field strengths, indicating the existence of strong interactions between the particles. At high shear rates, the mesostructures break apart due to the strong hydrodynamic stress and the shear stress increases with the shear rate. The suspensions of h-PDVB@Fe₃O₄ (2.51) and h-PDVB@Fe₃O₄ (1.83) show lower shear stress than the suspension of pure Fe₃O₄. Each h-PDVB@Fe₃O₄ has fewer magnetic particles (Fe₃O₄ nanoparticles) deposited on the surface of h-PDVB. Therefore, the magnetic dipole–dipole interaction between particles is weaker than that of pure Fe₃O₄, resulting in lower saturation magnetization and weakened mesostructures. For this reason, the h-PDVB@Fe₃O₄ suspensions show a faster increase in shear stress at high shear rate than the Fe₃O₄ suspension. For h-PDVB@Fe₃O₄ suspensions, the h-PDVB@Fe₃O₄ (2.51) suspension exhibits a higher shear stress than the h-PDVB@Fe₃O₄ (1.83) suspension due to its higher magnetic saturation (Figure 4). Figure 3.8 (b) shows the shear viscosity of the three suspensions as a function of the shear rate at different magnetic field strengths. The order of the magnitude of the shear viscosity was the same as the shear stress and the dynamic moduli. Similar to shear stress, the suspension with greater particle–particle interaction exhibits higher viscosity values. All fluids show shear thinning behavior at high shear rates.

Generally, MR fluids under the external magnetic field show Bingham fluid behaviors

expressed as

$$\tau = \tau_{dy} + \eta_{pl}\dot{\gamma} \quad (1)$$

where τ is the shear stress, τ_{dy} is the dynamic yield stress, η_{pl} is the plastic viscosity, and $\dot{\gamma}$ is the shear rate. [1,2,40] In the low shear rate region, both Fe_3O_4 and h-PDVB@ Fe_3O_4 suspensions exhibit a broad plateau due to the solid-like mesostructures induced by the applied magnetic field (Figure 3.8 (a)). In this region, the field-induced interaction between particles dominates the hydrodynamic interaction, which disturbs the mesostructures. The hydrodynamic interaction increases with the shear rate. When the hydrodynamic interaction surpassed the magnetic field-induced interaction at high shear rates, the hydrodynamic stress destroys the mesostructures and induces the flow of MR suspensions. [5,26] The yield stress is determined at the point where the mesostructures yield to the hydrodynamic stress. In MR suspension systems, two yield stresses are reported: a dynamic yield stress (τ_{dy}) and a static yield stress (τ_{sy}). [26–28] The dynamic yield stress is a stress of MR fluids when mesostructures are completely destroyed under continuous shearing. [5,26,41] It can be obtained by extrapolating the stress curve to zero shear rate. [27] On the other hand, the static yield stress is a minimum stress required to induce the flow of the suspension. [26] Under structural change conditions, the yield stress should be the static yield stress, rather than the dynamic yield stress. [28,29] A constitutive model to predict the static yield stress was recently proposed by Seo and Seo (Seo–Seo model [26]), expressed as

$$\tau = \tau_{sy} \left(1 - \frac{(1 - \exp(-a\dot{\gamma}))}{(1 + (a\dot{\gamma})^\alpha)} \right) + \eta_{pl}\dot{\gamma} \quad (2)$$

where τ_{sy} denotes the static yield stress at which the flow starts to flow, η_{pl} is the plastic viscosity, a is the time constant (the reciprocal of the critical shear rate for an aligned mesostructure deformation), and α is the power-law index which determine the degree of shear thinning. [26] This model predicts the static yield stress at low shear rate which corresponds to the absence of motion and a minimum in the stress curve. [26–28] The static yield stress obtained with this model shows a quadratic dependence on the magnetic field strength. [28] The static yield stress of the MR suspension can be measured experimentally by using the controlled shear stress (CSS) mode. [2,5] Figure 3.9 shows the change in the viscosity as a function of shear stress by using the CSS mode. At low shear stress, the viscosity of each suspension does not show considerable change with the shear stress. However, when the shear stress exceeds the yield stress, the viscosity suddenly drops several orders of magnitude, and the point is considered to be the static yield stress. [2,5] Static yield stress values obtained from the CSS mode, dynamic yield stress values predicted by the Bingham fluid model, and static yield stress values predicted by the Seo–Seo model are compared in Table 3.1. For all three suspensions, the experimental static yield stress values show good agreement with the values predicted by the Seo–Seo model (blue dashed lines in Figure 3.8 (a)). If the mesostructures are not strong enough, the partial destruction and re-formation of the mesostructures occur in the moderate shear rate range, while the point where fibril-like structures are completely destroyed is in the high shear rate range. This can lead to significant difference between the static yield stress

and the dynamic yield stress in electrorheological (ER) fluids. [1,5,41] In contrast, if the mesostructures are robust enough to withstand the applied shear stress at low shear rates, there appears a wide plateau in stress curve and the dynamic yield stress values obtained from Bingham fluid model are very close to static yield stress for all three suspensions (Figure 3.8 (a)). [5] In our previous study, we prepared suspensions based on foamed polystyrene (f-PS)/ Fe_3O_4 particles with core-shell structure and investigated their performance. The MR performance (yield stress values) for one of them whose density was 1.82 g/cm^3 is presented in Table 1 for comparison. By use of cubic shape Fe_3O_4 nanoparticles as a surfactant and stabilizer, submicrometer-sized f-PS/ Fe_3O_4 particles were synthesized via the Pickering-emulsion polymerization method. The size of the Fe_3O_4 nanoparticles adsorbed on the PS core was 50–100 nm. The average size of the f-PS/ Fe_3O_4 particles was ca. 660 nm, which is close to the particle size of h-PDVB@ Fe_3O_4 (~ 670 nm). The density of Fe_3O_4 in the f-PS/ Fe_3O_4 particle was 4.87 g/cm^3 , slightly higher than that of the synthesized pure Fe_3O_4 particle, 4.52 g/cm^3 in this study. It is worthy of note that two MR suspensions have apparently different MR properties depending on the magnetic field strengths, although there exists some uncertainty of sample comparison due to the density difference and Fe_3O_4 volume conversion. At low magnetic field strengths, h-PDVB@ Fe_3O_4 shows a higher yield stress than f-PS/ Fe_3O_4 , and vice versa at high magnetic yield strengths. This may be ascribable to the size difference of Fe_3O_4 nanoparticles. Fe_3O_4 nanoparticles of h-PDVB@ Fe_3O_4 have a particle size between 10 and 20 nm while that of f-PS/ Fe_3O_4 particles has a size between 50 and 100 nm. It is reported that magnetite cubic nanoparticles have a critical size of 76 nm for the formation of a multi-

domain structure whereas that for spherical Fe₃O₄ nanoparticles is 128 nm. [42–44] The crystallite size of Fe₃O₄ calculated from XRD data was 15 nm for h-PDVB@Fe₃O₄ (1.83) and 64 nm for cubic Fe₃O₄ of f-PS/Fe₃O₄. We calculated the crystallinity index (CI) value for the nanocubes and nanospheres as $CI = (\text{MNP size by SEM/TEM})/(\text{crystallite size})$. The CI was 0.8– 1.2 for the spherical Fe₃O₄ nanoparticles while that was 0.8– 1.5 for the cubic Fe₃O₄ of f-PS/Fe₃O₄ nanoparticles. The Fe₃O₄ nanoparticles synthesized in this study consist of a single domain, and those of f-PS/Fe₃O₄ nanoparticles consist of a single domain, too. High-resolution transmission electron microscopy (HRTEM) images of Fe₃O₄ nanoparticles (Figure 3.10) verified this. The HRTEM images of a spherical Fe₃O₄ particle and a cubic Fe₃O₄ particle show evidently that they are single domain particles. This is a contrary result to Li et al's report. [42] However, Lee et al. [45] also reported that magnetic properties of 100–225 nm cubic magnetic nanoparticles (MNPs) were respectively 1.4–3.0 and 1.1–8.4 times those of spherical MNPs on a same-volume and same-body diagonal/diameter basis. They also observed that the cubic Fe₃O₄ MNPs were more crystalline than the corresponding spherical MNPs. For the same size of 135 nm particles, the cubic particle showed highly single crystalline whereas the nanosphere was polycrystalline. This is a still controversial subject that needs to be studied further. [44,45] The HRTEM result indicates that the transformation of the multidomain cubic particles into single domain crystalline may not be the reason for the low yield stress value of the cubic Fe₃O₄ particles at low magnetic field strength (Figure 3.10 (b)). Instead of the domain change from the multidomain structure into the single domain, the different trends of the yield stress at low and high magnetic field strengths are due to the particles volume effect

that the large sizes of the cubic Fe₃O₄ particles compared to that of f-PS/Fe₃O₄ nanoparticles need higher magnetic field strength for the polarization. When the magnetic field strength is low, small size particles can achieve higher magnetization than the larger particles which leads to higher dipole interaction between the particles. On the other hand, high magnetic field strength can fully polarize the larger particles to induce stronger dipole interaction between the particles. Transformation of the multidomain structure of larger particles than the critical size into a single domain at high magnetic field strength to achieve higher magnetization does not seem to occur for the cubic nanoparticles in the f-PS/Fe₃O₄ nanoparticle.

For MR fluids, two main forces determine their MR behavior: magnetic polarization force and the hydrodynamic force. [26,38] The properties of MR fluids depend only on the ratio of the two forces. [41] The dependency can be expressed with a dimensionless variable, the Mason number ($M_n = 8\eta_0\dot{\gamma}/\mu_0\mu_c\beta^2 M^2$). [38,46] Here, η_0 is the medium viscosity, $\dot{\gamma}$ is the shear rate, β is the contrast factor ($= (\mu_p - \mu_c)/(\mu_p + 2\mu_c)$), μ_p is the particle relative permeability, μ_c is the relative permeability of the liquid medium phase, $\mu_0 = 4\pi \times 10^{-7} \text{ N}/\text{A}^2$ is the vacuum permeability, and M is the magnetic field strength. The Mason number is equivalent to $\dot{\gamma}/M^2$, corresponding to the ratio of hydrodynamic drag forces and magnetostatic forces acting on the particles. [1,42–44] When the particle volume fraction is fixed, the apparent viscosity of the suspension, which is the ratio of shear stress to shear rates ($=\tau/\dot{\gamma}$), is proportional to the reciprocal of the Mason number (M_n^{-1}). [41,46] Thus, the dependence of MR fluids' rheological properties on the shear rate

and the magnetic field strength can be expressed as a single variable which is proportional to the Mason number. With the Mason number as the only independent variable, a master curve for different MR fluids can be obtained by plotting the specific viscosity (ratio of the apparent viscosity to the zero-field viscosity) and volume fraction correction versus $\dot{\gamma}/M^2$ at different magnetic field strengths. [46] Figure 3.11 presents suspensions at two different magnetic field strengths. All experimental data were collapsed onto a single master curve. This means that both suspensions under external magnetic field show the same MR behavior with the same scaling law. [26,38] Though it is not shown in Figure 3.11, the aforementioned f-PS/Fe₃O₄ suspension displayed the same MR behavior as this study (see Figure 8 in ref 5). When we replot the dimensionless apparent viscosity of the Fe₃O₄ suspension at 343 kA/m in our previous study of Figure 8, we could observe a perfect overlapping with that of the present Fe₃O₄ suspension at 343 kA/m. This confirms the validity of the current MR fluid performance.

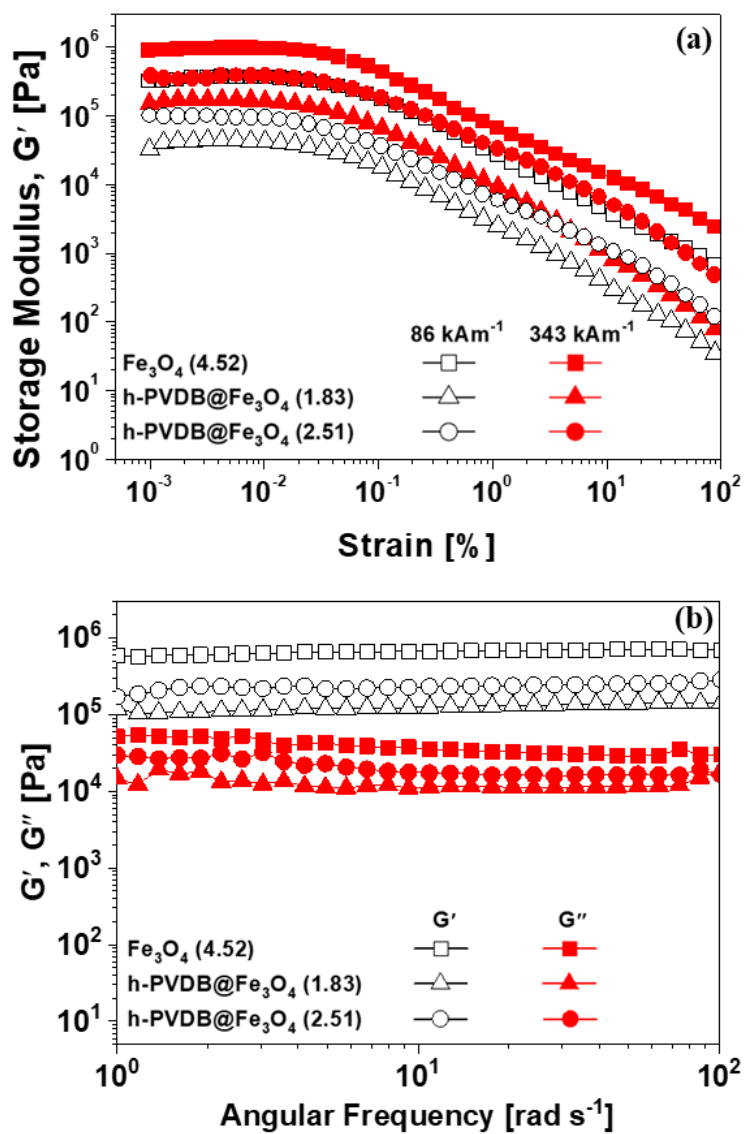


Figure 3. 7. (a) Amplitude sweep dependence of storage modulus and (b) Frequency dependence of storage modulus and loss modulus for pure Fe₃O₄ (4.52), h-PDVB@Fe₃O₄ (1.83) and h-PDVB@Fe₃O₄ (2.51) suspensions under 343 kA/m magnetic field (strain = 0.003 %).

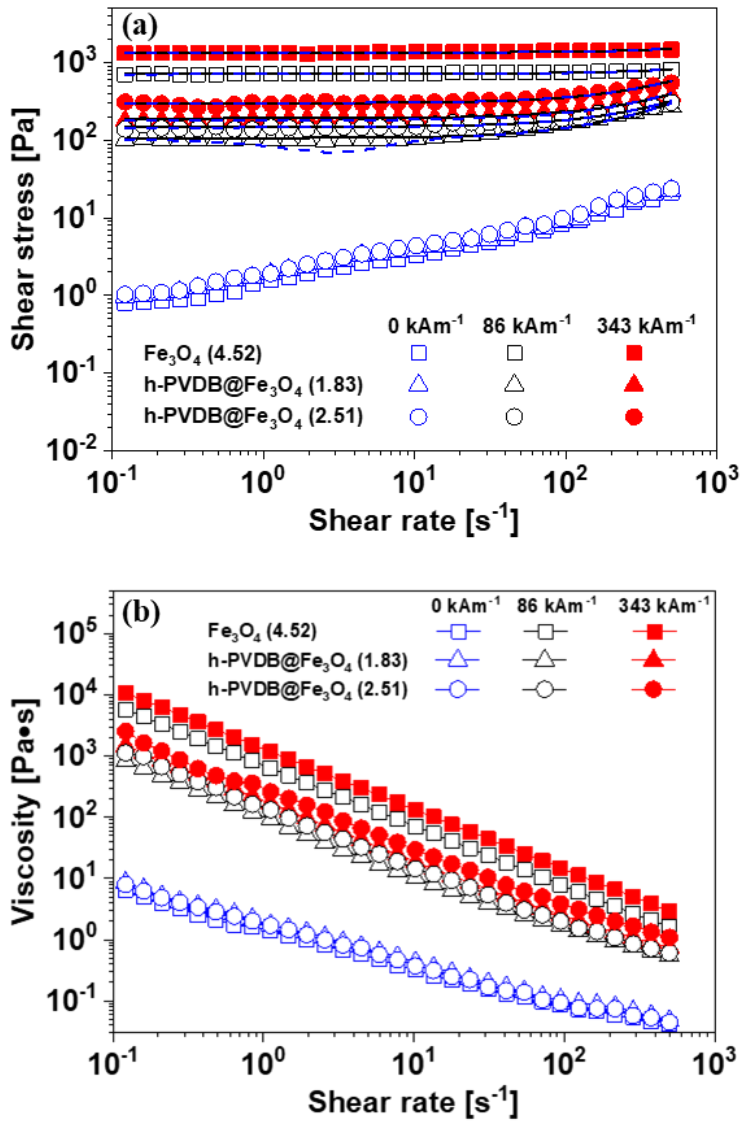


Figure 3. 8. (a) Shear stress and (b) shear viscosity flow curves for pure Fe_3O_4 , h-PDVB@ Fe_3O_4 (1.83) and h-PDVB@ Fe_3O_4 (2.51). The black solid lines and the blue dashed lines in (a) indicate predictions according to Bingham model and Seo-Seo model

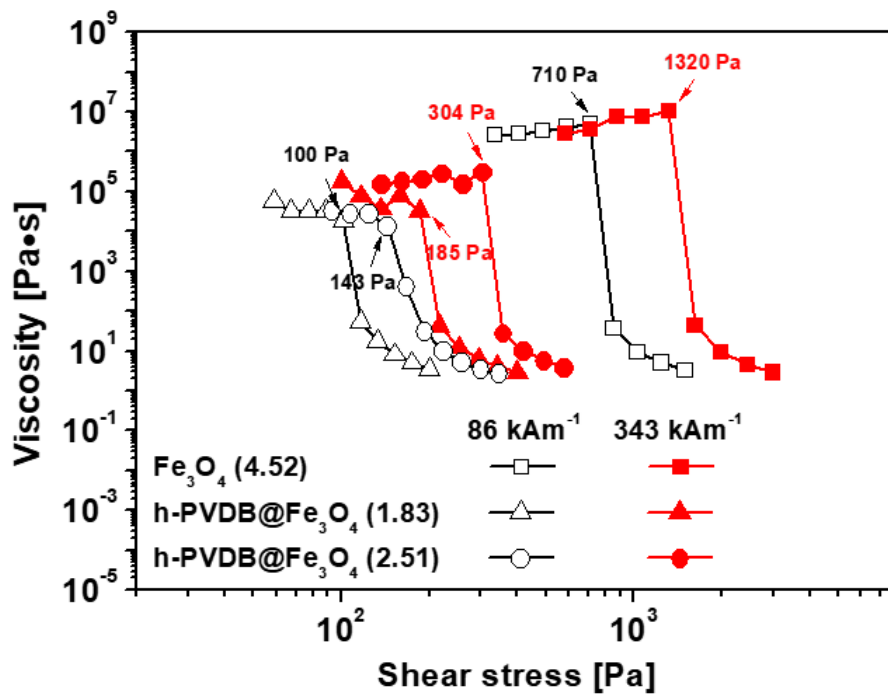


Figure 3. 9. Shear viscosity vs shear stress curves for pure Fe₃O₄ and h-PDVB@Fe₃O₄ suspensions

Table 3. 1. Static Yield Stress and Dynamic Yield Stress of Fe₃O₄, h-PDVB@Fe₃O₄ and f-PS/Fe₃O₄

	Yield stress (Pa)					
	M = 86 (kA/m)			M = 343 (kA/m)		
	Static exp (τ_{sy})	Dynamic (τ_{dy})	Static SS (τ_{sy})	Static exp (τ_{sy})	Dynamic (τ_{dy})	Static SS (τ_{sy})
Fe ₃ O ₄	710	715	710	1320	1340	1340
h-PDVB@Fe ₃ O ₄ (1.83)	100	105	105	185	190	180
h-PDVB@Fe ₃ O ₄ (2.51)	143	148	150	304	300	300
f-ps/Fe ₃ O ₄ (1.82) a)	74	70	74	293	285	297

a) The original particle concentration was converted to 10 vol% after taking into consideration of the Fe₃O₄ density difference. The average particle size was *ca.* 660nm. [5]

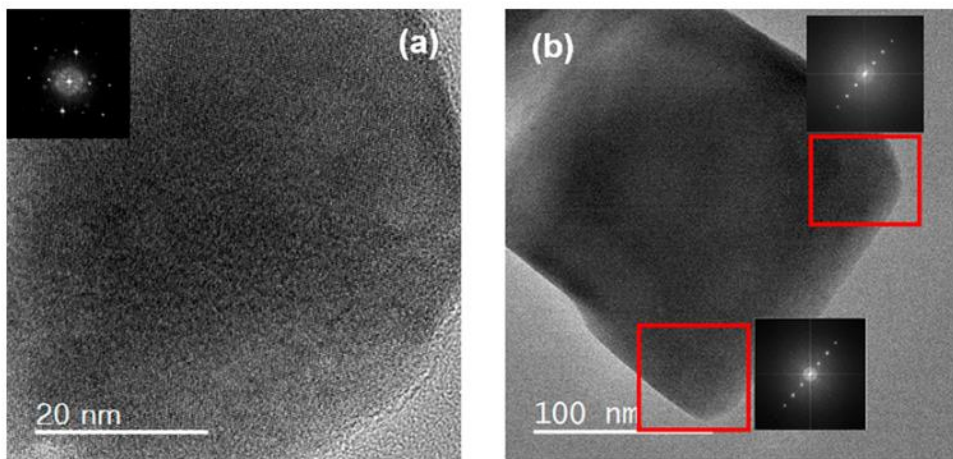


Figure 3. 10. HRTEM images of (a) Fe_3O_4 nanoparticles of $\text{h-PDVB@Fe}_3\text{O}_4$ and (b) a cubic Fe_3O_4 of $\text{f-PS/Fe}_3\text{O}_4$.

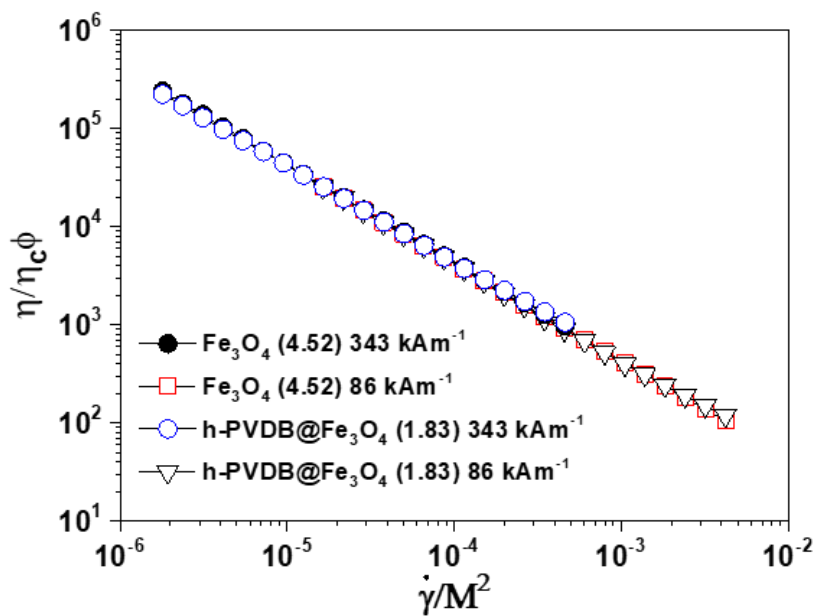


Figure 3. 11. Dimensionless apparent viscosity of the MR fluids as a function of $\dot{\gamma}/M^2$ at various magnetic field strengths

3. 3. 3. Long-Term Stability of Suspensions

The large cavity in the h-PDVB@Fe₃O₄ particles does not respond to the external magnetic field and results in a reduction in shear stress and the yield stress (Figures 8a and 9). However, the volume fraction of the cavity in the particle decreases the particle density significantly. The low particle density can contribute to a better long-term stability of the suspension. The sedimentation profile of each suspension as a function of time was measured with Turbiscan and is presented in Figure 3.12. In the suspension of pure Fe₃O₄, the light h, which means Fe₃O₄ particles settled down to bottom very quickly. Because of their large cavity, however, h-PDVB@Fe₃O₄ particles exhibit a significantly better stability against sedimentation than pure Fe₃O₄ particles. For the h-PDVB@Fe₃O₄ (2.51) suspension, light transmission reached 34% after 2 h and remained nearly the same for 24 h, while the light transmission after 2 h was only 13% for the h-PDVB@Fe₃O₄ (1.83) suspension, showing no appreciable change after 24 h. This indicates that most of the suspended h-PDVB@Fe₃O₄ (1.83) particles remain in the suspension for 24 h. The spherical particle sedimentation velocity can be described as

$$V(\phi, d) = \frac{|\rho_p - \rho_c| \times g \times d^2}{18 \times \nu \times \rho_c} \cdot \frac{[1 - \phi]}{\left[1 + \frac{4.6\phi}{(1 - \phi)^3}\right]} \quad (3)$$

where V is the particle migration velocity (m s⁻¹), ρ_p represents the particle density, ρ_c denotes the continuous phase density (kg m³), ν designates the kinematic viscosity of continuous phase, g is gravity constant (9.81 m s⁻²), d means the particle diameter, and ϕ represents the volume fraction of particles. [2,49] From the equation it can be realized that

the decrease of the density mismatch between particle and medium reduces the sedimentation velocity. Thus, it can be seen from the density measurement results that h-PDVB@Fe₃O₄ suspensions are more stable. According to the equation, larger diameter particles show a faster sedimentation velocity. However, after deposition of the Fe₃O₄ nanoparticles on the h-PDVB@Fe₃O₄, the particles have a relatively rough surface (Figure 3f,g). The bumpy and rough surface particles experience more friction in the medium, and this frictional force can offset the effect of the particle size on the sedimentation velocity. [5,46] The suspension of f-PS/Fe₃O₄ ($\rho = 1.82 \text{ g/cm}^3$) shows similar stability (10% transmission after 24 h). Taking into consideration the rougher surface due to the larger Fe₃O₄ particles on the f-PS particle surface which resists against the sedimentation and a slightly lower density, the stability agreement between them lies within the experimental error. This result confirms that not only the density mismatch but also the surface topology of the particles are significant factors for the suspension stability when the particle volume fraction and the density mismatch are the same.

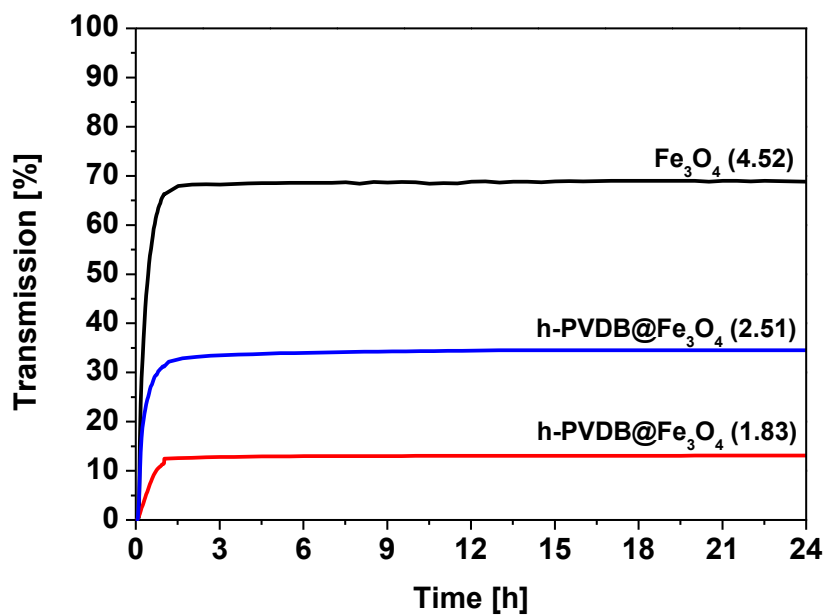


Figure 3. 12. Transmission [%] curve as a function of time [h] for pure Fe₃O₄, h-PVDB@Fe₃O₄ (1.83), and h-PVDB@Fe₃O₄ (2.51).

3. 4. Conclusions

To improve the sedimentation stability of MR suspensions, hollow nanoparticles of PDVB@Fe₃O₄ (h-PDVB@Fe₃O₄) were fabricated by the distillation–precipitation polymerization method using SiO₂ particles as a template, followed by etching the SiO₂ core and deposition of Fe₃O₄ nanoparticles having a size of 14.3 ± 2.5 nm. Nanometer-sized Fe₃O₄ particles were deposited on the PDVB hollow sphere. The incorporation of a large cavity significantly reduced the density of the nanoparticles from 4.52 g/cm³ (Fe₃O₄) to 2.51 and 1.83 g/cm³ with high Fe₃O₄ content of ca. 70.4% and 59.5%, respectively. Although the suspensions containing h-PDVB@Fe₃O₄ particles showed a lower yield stress due to the less amount of Fe₃O₄ and thus lower saturation magnetization compared to the pure Fe₃O₄ suspension, the MR behavior was well preserved, and the h-PDVB@Fe₃O₄ particle suspensions proved the advantage of long-term stability resulting from the reduced density mismatch between the particles and the liquid medium. The smaller spherical Fe₃O₄ nanoparticle suspension shows the edge when they respond to a low external magnetic field for polarization, while the larger Fe₃O₄ nanoparticles achieve higher magnetization and thus higher yield stress at high magnetic field strengths. The yield stress values manifest this size effect of the particles. HRTEM results verify that transformation of the multidomain structure in the large particle is not the reason. The sedimentation profile of pure Fe₃O₄ suspensions showed 65% light transmission within 2 h. In contrast, h-PDVB@Fe₃O₄ suspensions showed much better long-term stability.

Especially, a suspension containing h-PDVB@Fe₃O₄ (1.83) exhibited a remarkable stability with a light transmission of 13% after 24 h, which means that most of the particles remained in the dispersed state after 24 h. The results demonstrate the usefulness of the low-density hollow particles and controlled amount of magnetic particle content prepared by the method described in this work. The long-term stability results are also consistent with the previous study to elucidate the possibility of overcoming the MR fluids sedimentation problem. Depending on the particle size and applied magnetic field strength, a niche application of stable nanoparticle suspensions to microfluidics can be sought.

References

- (1) Seo, Y. P.; Han, S.; Choi, J.; Takahara, A.; Choi, H. J.; Seo, Y. Searching for a Stable High-Performance Magnetorheological Suspension. *Adv. Mater.* 2018, 30, 1704769.
- (2) Chuah, W. H.; Zhang, W. L.; Choi, H. J.; Seo, Y. Magnetorheology of Core-Shell Structured Carbonyl Iron/Polystyrene Foam Nanoparticles Suspension with Enhanced Stability. *Macromolecules* 2015, 48 (19), 7311–7319.
- (3) Ghaffari, A.; Hashemabadi, S. H.; Ashtiani, M. A review on the simulation and modeling of magnetorheological fluids. *J. Intell. Mater. Syst. Struct.* 2015, 26 (8), 881–904.
- (4) Liu, Y. D.; Lee, J.; Choi, S. B.; Choi, H. J. Silica-coated carbonyl iron microsphere based magnetorheological fluid and its damping force characteristics. *Smart Mater. Struct.* 2013, 22 (6), 065022.
- (5) Han, S.; Choi, J.; Seo, Y. P.; Park, I. J.; Choi, H. J.; Seo, Y. High Performance Magnetorheological Suspensions of Pickering-Emulsion-Polymerized Polystyrene/Fe₃O₄ Particles with Enhanced Stability. *Langmuir* 2018, 34 (8), 2807–2814.
- (6) Park, B. J.; Fang, F. F.; Choi, H. J. Magnetorheology: materials and application. *Soft Matter* 2010, 6 (21), 5246–5253.
- (7) Bitaraf, M.; Ozbulut, O. E.; Hurlebaus, S.; Barroso, L. Application of semi-active control strategies for seismic protection of buildings with MR dampers. *Engineering Structures* 2010, 32 (10), 3040–3047.
- (8) Oliveira, F.; de Moraes, P. G.; Suleman, A. Semi-active control of base-isolated structures. *Procedia Eng.* 2015, 114, 401–409.

- (9) Chen, Z.; Wang, X.; Ko, J.; Ni, Y.; Spencer, B. F.; Yang, G. MR damping system on Dongting Lake cable-stayed bridge. *Proc. SPIE* 2003, 5057, 229–236.
- (10) Choi, H. J.; Zhang, W. L.; Kim, S.; Seo, Y. Core-Shell Structured Electro- and Magneto-Responsive Materials: Fabrication and Characteristics. *Materials* 2014, 7 (11), 7460–7471.
- (11) Quan, X.; Chuah, W.; Seo, Y.; Choi, H. J. Core-Shell Structured Polystyrene Coated Carbonyl Iron Microspheres and their Magnetorheology. *IEEE Trans. Magn.* 2014, 50 (1), 1–4.
- (12) Cvek, M.; Mrlik, M.; Ilcikova, M.; Plachy, T.; Sedlacik, M.; Mosnacek, J.; Pavlinek, V. A facile controllable coating of carbonyl iron particles with poly(glycidyl methacrylate): a tool for adjusting MR response and stability properties. *J. Mater. Chem. C* 2015, 3 (18), 4646–4656.
- (13) Rankin, P. J.; Horvath, A. T.; Klingenberg, D. J. Magnetorheology in viscoplastic media. *Rheol. Acta* 1999, 38 (5), 471–477.
- (14) Chin, B. D.; Park, J. H.; Kwon, M. H.; Park, O. O. Rheological properties and dispersion stability of magnetorheological (MR) suspensions. *Rheol. Acta* 2001, 40 (3), 211–219.
- (15) Pramudya, I.; Sutrisno, J.; Fuchs, A.; Kavlicoglu, B.; Sahin, H.; Gordaninejad, F. Compressible Magnetorheological Fluids Based on Composite Polyurethane Microspheres. *Macromol. Mater. Eng.* 2013, 298 (8), 888–895.
- (16) Fang, F. F.; Choi, H. J.; Seo, Y. Sequential Coating of Magnetic Carbonyl iron Particles with Polystyrene and Multiwalled Carbon Nanotubes and Its Effect on Their

Magnetorheology. *ACS Appl. Mater. Interfaces* 2010, 2 (1), 54–60.

(17) Fang, F. F.; Liu, Y. D.; Choi, H. J.; Seo, Y. Core-Shell Structured Carbonyl Iron Microspheres Prepared via Dual-Step Functionality Coatings and Their Magnetorheological Response. *ACS Appl. Mater. Interfaces* 2011, 3 (9), 3487–3495.

(18) Sedlacik, M.; Pavlinek, V.; Saha, P.; Svrčinova, P.; Filip, P.; Stejskal, J. Rheological properties of magnetorheological suspensions based on core-shell structured polyaniline-coated carbonyl iron particles. *Smart Mater. Struct.* 2010, 19 (11), 115008.

(19) Liu, Y. D.; Choi, H. J.; Choi, S. B. Controllable fabrication of silica encapsulated soft magnetic microspheres with enhanced oxidation-resistance and their rheology under magnetic field. *Colloids Surf., A* 2012, 403, 133–138.

(20) Kim, Y. J.; Liu, Y. D.; Seo, Y.; Choi, H. J. Pickering-Emulsion-Polymerized Polystyrene/Fe₂O₃ Composite Particles and Their Magnetoresponse Characteristics. *Langmuir* 2013, 29 (16), 4959–4965.

(21) Li, G. L.; Lei, C. L.; Wang, C. H.; Neoh, K. G.; Kang, E. T.; Yang, X. L. Narrowly Dispersed Double-Walled Concentric Hollow Polymeric Microspheres with Independent pH and Temperature Sensitivity. *Macromolecules* 2008, 41 (23), 9487–9490.

(22) Li, G. L.; Tai, C. A.; Neoh, K. G.; Kang, E. T.; Yang, X. L. Hybrid nanorattles of metal core and stimuli-responsive polymer shell for confined catalytic reactions. *Polym. Chem.* 2011, 2 (6), 1368–1374.

(23) Yang, X. Y.; Chen, L.; Han, B.; Yang, X. L.; Duan, H. Q. Preparation of magnetite and tumor dual-targeting hollow polymer microspheres with pH-sensitivity for anticancer drug-carriers. *Polymer* 2010, 51 (12), 2533–2539.

- (24) Perez-Lorenzo, M.; Vaz, B.; Salgueirino, V.; Correa-Duarte, M. A. Hollow-Shelled Nanoreactors Endowed with High Catalytic Activity. *Chem. - Eur. J.* 2013, 19 (37), 12196–12211.
- (25) Pu, H. T.; Jiang, F. J.; Yang, Z. L. Preparation and properties of soft magnetic particles based on Fe₃O₄ and hollow polystyrene microsphere composite. *Mater. Chem. Phys.* 2006, 100 (1), 10–14.
- (26) Seo, Y. P.; Seo, Y. Modeling and Analysis of Electrorheological Suspensions in Shear Flow. *Langmuir* 2012, 28 (6), 3077–3084.
- (27) Seo, Y. P.; Choi, H. J.; Seo, Y. A simplified model for analyzing the flow behavior of electrorheological fluids containing silica nanoparticle-decorated polyaniline nanofibers. *Soft Matter* 2012, 8 (17), 4659–4663.
- (28) Seo, Y. P.; Kwak, S.; Choi, H. J.; Seo, Y. Static yield stress of a magnetorheological fluid containing Pickering emulsion polymerized Fe₂O₃/polystyrene composite particles. *J. Colloid Interface Sci.* 2016, 463, 272–278.
- (29) Seo, Y. P.; Choi, H. J.; Lee, J. R.; Seo, Y. Modeling and analysis of an electrorheological flow behavior containing semiconducting graphene oxide/polyaniline composite particles. *Colloids Surf., A* 2014, 457, 363–367.
- (30) Bai, F.; Yang, X. L.; Huang, W. Q. Synthesis of narrow or monodisperse poly(divinylbenzene) microspheres by distillation-precipitation polymerization. *Macromolecules* 2004, 37 (26), 9746–9752.
- (31) Bai, F.; Yang, X. L.; Huang, W. Q. Preparation of narrow or monodisperse poly(ethyleneglycol dimethacrylate) microspheres by distillation-precipitation

polymerization. *Eur. Polym. J.* 2006, 42 (9), 2088–2097.

(32) Liu, G. Y.; Li, L. Y.; Yang, X. L.; Dai, Z. Preparation of silica/ polymer hybrid microspheres and the corresponding hollow polymer microspheres with functional groups. *Polym. Adv. Technol.* 2008, 19 (12), 1922–1930.

(33) Li, G. L.; Yang, X. Y.; Wang, B.; Wang, J. Y.; Yang, X. L. Monodisperse temperature-responsive hollow polymer microspheres: Synthesis, characterization and biological application. *Polymer* 2008, 49 (16), 3436–3443.

(34) Park, S. J.; Lim, H. S.; Lee, Y. M.; Suh, K. D. Facile synthesis of monodisperse poly(MAA/EGDMA)/Fe₃O₄ hydrogel microspheres with hollow structures for drug delivery systems: the hollow structure formation mechanism and effects of various metal ions on structural changes. *RSC Adv.* 2015, 5 (13), 10081–10088.

(35) Yoon, C. M.; Noh, J.; Jang, Y.; Jang, J. Fabrication of a silica/ titania hollow nanorod and its electroresponsive activity. *RSC Adv.* 2017, 7, 19754–19763.

(36) Chiriac, H.; Stoian, G. Influence of the particles size and size distribution on the magnetorheological fluids properties. *IEEE Trans. Magn.* 2009, 45, 4049–4051. (37)

Sherman, S. G.; Wereley, N. M. Effect of particle size distribution on chain structures in magnetorheological fluids. *IEEE Trans. Magn.* 2013, 49, 3430–3433.

(38) Lemaire, E.; Meunier, A.; Bossis, G.; Liu, J.; Felt, D.; Bashtovoi, P.; Matussevitch, N. Influence of the particle size on the rheology of magnetorheological fluids. *J. Rheol.* 1995, 39, 1011–1020.

(39) Upadhyay, R. V.; Laherisheth, Z.; Shah, K. Rheological properties of soft magnetic flake shaped iron particle based magnetorheological fluid in dynamic mode.

Smart Mater. Struct. 2014, 23 (1), 015002.

(40) Farjoud, A.; Vahdati, N.; Fah, Y. F. Mathematical model of drum-type MR brakes using Herschel-Bulkley shear model. *J. Intell. Mater. Syst. Struct.* 2008, 19 (5), 565–572.

(41) Parmar, K. P. S.; Meheust, Y.; Schjelderupsen, B.; Fossum, J. O. Electrorheological suspensions of laponite in oil: Rheometry studies. *Langmuir* 2008, 24 (5), 1814–1822.

(42) Li, Q.; Kartikowati, C. W.; Horie, S.; Ogi, T.; Iwaki, T.; Okuyama, K. Correlation between particle size/domain structure and magnetic properties of highly crystalline Fe₃O₄ nanoparticles. *Sci. Rep.* 2017, 7, 9894.

(43) Butler, R. F.; Banerjee, S. K. Theoretical single-domain grain size range in magnetite and titanomagnetite. *J. Geophys. Res.* 1975, 80, 4049–4058.

(44) Wu, X.; Xiao, X.; Tian, Z.; Chen, F.; Jian, W. Effect of Particle Characteristics and Temperature on Shear Yield Stress of Magnetorheological Fluid. *J. Magn.* 2016, 21 (2), 244–248.

(45) Kolhatkar, A. G.; Chen, Y.; Chinwangso, P.; Nekrashevich, I.; Dannangoda, G. C.; Singh, A.; Jamison, A. C.; Zenasni, O.; Rusakova, I. A.; Martirosyan, K. S.; Litvinov, D.; Xu, S.; Willson, R. C.; Lee, T. R. Magnetic Sensing Potential of Fe₃O₄ Nanocubes Exceeds That of Fe₃O₄ Nanospheres. *ACS Omega* 2017, 2, 8010–8019.

(46) de Vicente, J.; Klingenberg, D. J.; Hidalgo-Alvarez, R. Magnetorheological fluids: a review. *Soft Matter* 2011, 7 (8), 3701–3710.

(47) Shah, K.; Phu, D. X.; Seong, M. S.; Upadhyay, R. V.; Choi, S. B. A low sedimentation magnetorheological fluid based on plate-like iron particles, and verification

using a damper test. *Smart Mater. Struct.* 2014, 23 (2), 015004.

(48) Becnel, A. C.; Sherman, S.; Hu, W.; Wereley, N. M. Nondimensional scaling of magnetorheological rotary shear mode devices using the Mason number. *J. Magn. Magn. Mater.* 2015, 380, 90–97.

(49) Mills, P.; Snabre, P. Settling of a suspension of hard spheres. *Europhys. Lett.* 1994, 25 (9), 651–656

Chapter 4. Hierarchically Structured Fe₃O₄ Nanoparticles for High-Performance Magnetorheological Fluids with Long-Term Stability

4. 1. Introduction

Smart materials, whose properties varies with external stimuli, have been applied in various industrial field due to their quick responsiveness. [1-4] Magnetorheological (MR) fluid, which consists of magnetic particles dispersed in a non-magnetic carrier medium, is a kind of smart material due to its rapid response to an external magnetic field. [5, 6] Once the magnetic field is turned on, the magnetic particles in MR fluids are aggregated to form chain-like structures due to magnetic dipole interactions between the particles along the field direction. [7, 8] The chain-like structures (meso-structures) increase the viscosity of MR fluids very quickly by the transformation of the MR fluids from a liquid-like state to a solid-like elastic state in milliseconds. [7-11] Since this process is reversible, the rheological properties of MR fluids can be easily controlled by the magnetic field. [12] The quick reacting properties to an external magnetic field allow MR fluids to be used for haptic devices, rotor dampers, shock absorbers in motorcycles and power steering pumps, as well as large damping systems to protect buildings and bridges from external shocks or impacts. [12-16]

One of the main obstacles to the practical use of MR systems is the long-term stability problem caused by the density mismatch between the light carrier medium and heavy magnetic particles. [5,6,17–19] It induces rapid sedimentation of magnetic particles, which makes redispersion of the particles and the reuse of MR liquids very difficult. [20] To solve this problem, much research has focused on the fabrication of composite magnetic particles. Through the combination of magnetic particles with lightweight materials such as polymers, SiO₂, and carbon materials, composite materials of various structures (core–shell structures, magnetic particle decorated fibers and tubes, and hollow structures) with low density were obtained and used for MR fluids. [21–26] These composites could improve the long-term stability in MR fluid compared to bare magnetic particles because of reduced density mismatch between particles and the carrier.

In our previous works, we made magnetic composite particles containing air inside the structures and used them for MR fluids. For example, carbonyl iron/foamed polystyrene (PS) ($\rho = 5.10 \text{ g/cm}^3$) and foamed PS/Fe₃O₄ ($\rho = 1.82 \text{ g/cm}^3$) particles were obtained by combining magnetic particles with polystyrene followed by the foaming process of PS with supercritical CO₂. [27,28] The density of the composite particles was significantly reduced by the pores formed in the PS layer, which improved the stability of their MR suspensions. To reduce the density mismatch further, we made hollow structured polydivinylbenzene (PDVB)/ Fe₃O₄ ($\rho = 1.83 \text{ g/cm}^3$) using SiO₂, as a template. [29] Although the content of Fe₃O₄ was high, the large cavity inside the PDVB core allowed the particle to have a very low density, which led to a remarkably improved stability

compared to the bare Fe_3O_4 suspension. These results demonstrate that introduction of pores or cavity into the structures is a very efficient strategy for reducing the magnetic particle density. However, since non-magnetic polymeric materials are incorporated into the composite particles, a reduction in the magnetic properties and a consequent deterioration of the MR performance (shear stress, modulus, and viscosity under a magnetic field) are inevitable due to a weakened interaction between particles. To prepare a high performance MR fluid with good long-term stability, we tried to synthesize submicrometer-sized magnetic particles that do not contain nonmagnetic materials but can contain a certain cavity in them. For this purpose, hierarchically structured Fe_3O_4 (HS- Fe_3O_4) particles were prepared. Submicrometer HS particles are secondary structured particles that consist of a large number of small primary nanoparticles. [30,31] Because of advantages such as large surface areas, light scattering effects, and rapid electron transport, HS particles composed of TiO_2 nanoparticles or ZnO nanoparticles have been widely applied in the manufacturing of solar cell electrodes. [32–36] In addition, hierarchically structured hollow TiO_2 particles fabricated by a hydrothermal method were used for electrorheological (ER) fluids. [37,38] In this study, we applied the electrospray process for efficient production of submicrometer-sized HS- Fe_3O_4 particles. Although similar methods have been used for other purposes, they have not been used for the production of submicrometer Fe_3O_4 particles for use in magnetorheological fluids. [30,38] During the ES process in the presence of an electric field between the solution and the substrate, the colloidal solution of nanoparticles is divided into many charged droplets. The solvent in the droplets evaporates while traveling to the substrate, and the HS particles remain.

[30,31,39] We propose a new method for the production of hierarchically structured Fe_3O_4 particles in the submicrometer range. Although similar methods have been used for other purposes, it has not been used for the preparation of submicrometer Fe_3O_4 particles for the magnetorheological fluids. [30–38] Because this process does not require surfactants or binders and is not a high-temperature process, it has often been widely used as an inexpensive and simple method of depositing particles on the substrate. [31,40,41] In this study, spherical HS- Fe_3O_4 particles were prepared by using a citric acid-capped Fe_3O_4 solution. Because of the pores or a cavity between Fe_3O_4 nanoparticles, the density of the HS particles was reduced by about 23% compared to bare Fe_3O_4 without the use of light materials. The MR fluids based on HS particles were prepared by dispersing submicrometer-sized HS- Fe_3O_4 particles in a silicone oil. The absence of nonmagnetic materials in HS- Fe_3O_4 allows the MR fluid to perform better than other suspensions based on Fe_3O_4 composite. In addition, the MR fluids showed better stability than capped Fe_3O_4 or bare Fe_3O_4 suspensions due to a reduced density mismatch between HS- Fe_3O_4 and silicone oil that originated from the cavity and pores in the hierarchical structure.

4. 2. Experimental Section

4. 2. 1. Synthesis of Citric Acid-Capped Fe_3O_4

Because the bare Fe_3O_4 solution cannot maintain a stable state in the ultrasonic process,

Fe₃O₄ particles must be stabilized with a capping agent to be used in the electrospray process. Citric acid was used as a capping agent to stabilize them. [42] FeCl₃ (5.6 g) (97%, Sigma-Aldrich, USA) and FeCl₂·4H₂O (3.436 g) (≥99.0%, Sigma-Aldrich, USA) were dissolved in H₂O (400 mL) bubbled with N₂ gas beforehand. All processes were performed under a nitrogen atmosphere. The solution temperature was set to 80 °C and held for 30 min to produce magnetite (not hematite), followed by injection of ammonia solution (40 mL) (28% w/w in H₂O, TCI, Japan). After the reaction (2 FeCl₃ + FeCl₂ + 8NH₃ + 4H₂O → Fe₃O₄ + 8NH₄Cl) was continued for another 30 min, aqueous citric acid solution (20 mL, concentration of 0.5 g/mL) was injected to the reaction medium. Then, the reaction proceeded for 1.5 h at 90 °C. Fe₃O₄ particles capped with citric acid were obtained after the repeated centrifugation and redispersion and washed several times with H₂O. The washed product was dried under vacuum at 25 °C.

4. 2. 2. Fabrication of HS-Fe₃O₄ with the Electrospraying Process

Figure 4.1 is the schematic diagram for electrospray process. The capped Fe₃O₄ particles were dispersed in ethanol/H₂O solution (30 mL, 9:1, v:v) at the concentration of 5% w/v. The dispersed solution was loaded onto a polypropylene syringe which was connected to a high-voltage supply. Then, the solution was electrosprayed onto the substrate under an applied electric field of 2.5 kV/cm with a distance of 8 cm between the nozzle tip and the substrate (Figure 4.1). The solution feed rate was 3 mL/h. After completion of the

electrospray process, the sprayed particles were collected and used for characterization and measurement of MR properties and long-term stability.

4. 2. 3. Characterization

Scanning electron microscopy (SEM; MERLIN Compact, ZEISS, Oberkochen, Germany) and transmission electron microscopy (TEM; JEM-2100F, JEOL Ltd., Tokyo, Japan) were used to characterize the morphologies of HS-Fe₃O₄ particles,. A thermogravimetric analysis (TGA; Mettler Toledo TGA DSC 1, Mettler Toledo, OH) was used to estimate thermal properties of the magnetic particles. TGA tests were performed from 25 to 800 °C under an N atmosphere. The heating rate was set to 10 °C/min. The density of magnetic particles was measured with a helium pycnometer (AccuPyc 1330, Micromeritics Instrument Corporation, Norcross, GA). The magnetization of capped Fe₃O₄ and HS-Fe₃O₄ was measured by using a vibrating sample magnetometer (VSM; VSM7410, Lake Shore Cryotronics, USA) in the -10 to 10 kOe magnetic field range. An optical microscope (Olympus BX-51) equipped with a CCD camera was used to take the photographs of development of chain-like structures with a magnetic field. A rotational rheometer (Physica MCR301, Stuttgart, Germany) equipped with a magnetic generator (Physica MRD 180, Stuttgart, Germany) measured the MR properties of suspensions. Silicone oil (KF-96, 10 cS, Shin Etsu, Japan) was used as an inert liquid medium, and a MR fluid with a particle concentration of 10 vol % was prepared for tests by dispersing the magnetic particles in

the silicone oil with ultrasonication. Strain amplitude sweep (storage modulus vs strain), frequency sweep (storage and loss modulus vs angular frequency), flow curves (shear stress and viscosity vs strain rate), controlled shear stress (viscosity vs shear stress), and reversibility tests were conducted. Finally, Turbiscan (Classic MA2000, Formulation, France) measured the long-term stability of suspensions by observing the change in light transmission over 24 h.

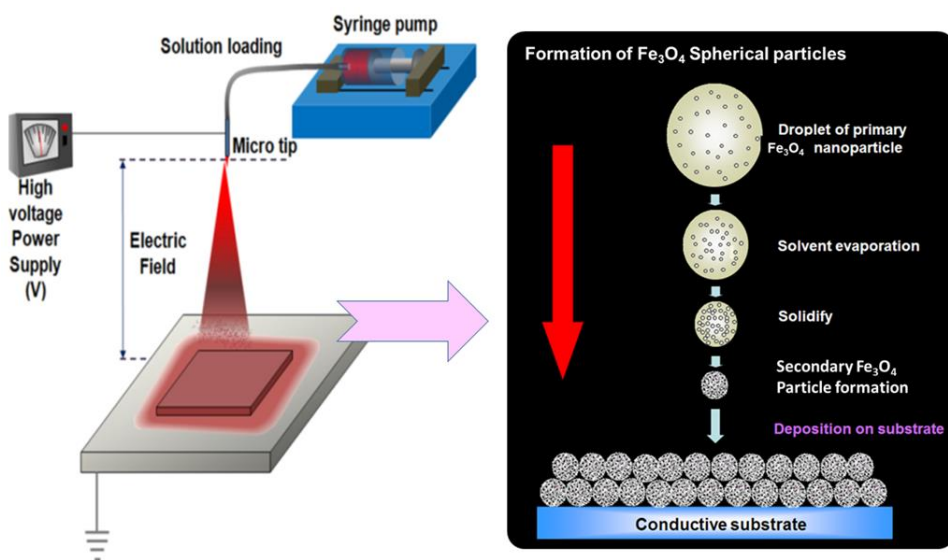


Figure 4. 1. Schematic description of the electro spray process.

4. 3. Results and Discussions

4. 3. 1. Morphologies and Structures

Figures 4.2 (a),(b) show SEM images and Figures 2c,d show TEM images of HS-Fe₃O₄ particles. SEM images of HS- Fe₃O₄ clearly show the formation of submicrometer-sized spherical HS particles composed of capped Fe₃O₄ particles by the ES process. However, a certain size distribution is observed (the average particle size is roughly 356 ± 72 nm, but it varies widely depending on the sample preparation condition). [30,33] The TEM image (Figure 4.2 (c)) more clearly shows HS-Fe₃O₄ composed of capped Fe₃O₄. The particle size of capped Fe₃O₄ from the enlarged TEM image of HS-Fe₃O₄ (Figure 2d) was 11.7 ± 2.8 nm. With the formation of HS particles by the ES process, the density of the magnetic particles decreased from 4.29 g/cm³ for capped Fe₃O₄ to 3.32 g/cm³ for HS-Fe₃O₄. Because no polymers or other binders were used in the ES process, the reduction in density is obviously attributed to the formation of pores in HS-Fe₃O₄ with aggregation of nanoparticles during the evaporation of solvents. For electrospayed HS-TiO₂ particles, it is known that inter-particle connectivity between primary particles is improved compared to non-structured TiO₂, resulting in better electron transport within the structure. [30,33] For submicrometer-sized HS-Fe₃O₄, such connectivity between primary capped Fe₃O₄ particles can contribute to the formation of closed pores or a cavity, which cannot be reached by gases, leading to a reduced density of HS-Fe₃O₄. From the images and results of the density measurement, it is certain that hierarchically structured particles with low

density can easily be obtained with a very simple electrospray technique. The magnetic properties of capped Fe_3O_4 and HS- Fe_3O_4 were examined with VSM (Figure 4.3 (a)). Both particles show a typical superparamagnetic behavior with a very narrow hysteresis curve and a small coercive field. The saturation magnetization (M_s) value of capped Fe_3O_4 is 73 emu/g, while that of HS- Fe_3O_4 is 70 emu/g, close to that of capped Fe_3O_4 . Because the density of air in the pores or a cavity is much lower than all other materials, the weight percentage of the pores in HS- Fe_3O_4 is very low. Thus, the M_s of HS- Fe_3O_4 is comparable to that of capped Fe_3O_4 while its density is only ca. 77% of capped Fe_3O_4 . This M_s value of HS- Fe_3O_4 is much higher than that of other Fe_3O_4 composites in our previous work, which contain a large portion of magnetically inactive polymers (PS and PDVB). [28,29]

To check the weight change in capped Fe_3O_4 and HS- Fe_3O_4 with the temperature, TGA for both samples were conducted. (Figure 4.3(b)). Because both particles are composed of Fe_3O_4 and citric acid, the residual weight at the final temperature and weight change profile with their temperature were very similar. The residual weight at 800 °C was 91.8% and 91.0% for capped Fe_3O_4 and HS- Fe_3O_4 , respectively. The weight loss for these particles is attributed to removal of physically adsorbed water and chemical water (surface hydroxyl groups on Fe_3O_4) and the decomposition of citric acid. The removal of water takes place over the whole temperature range, and decomposition of citric acid at the surface is known to occur in the temperature range of 180–270 °C. [43,44] However, the weight change due to degradation of citric acid was not distinct from the removal of water, which indicates that the amount of citric acid on the surface is quite small.

To check whether synthesized iron-oxide particles are Fe_3O_4 XRD measurements for capped- Fe_3O_4 and HS- Fe_3O_4 were conducted (Figure 4.4). Both XRD patterns showed characteristic diffraction peaks corresponding to [220], [440], [400], [422], [511] and [311] planes of Fe_3O_4 . Although $\gamma\text{-Fe}_2\text{O}_3$ could show same XRD peaks, the M_s values of capped- Fe_3O_4 and HS- Fe_3O_4 prove that main iron species comprising them are Fe_3O_4 . The average crystallite size of primary Fe_3O_4 nanoparticles calculated with Scherrer formula ($D = K\lambda/(\beta\cos\theta)$) for [440] peaks was 9.3 nm and 10.6 nm for capped- Fe_3O_4 and HS- Fe_3O_4 , respectively, slightly smaller than particle size measured from TEM images.

The formation of a chain-like structure in HS- Fe_3O_4 MR fluids under a magnetic field was observed with an optical microscope (Figure 4.5). The HS- Fe_3O_4 particles were in the dispersed state without a magnetic field. Once the magnetic field was applied, HS- Fe_3O_4 particles formed chain-like structures very quickly, showing a rapid transition from a liquid-like state to a solid-like state. As soon as the magnetic field is turned off, the particles return to their original state, which means that the formation of chain-like structures is a reversible process (this reversibility is discussed again later).

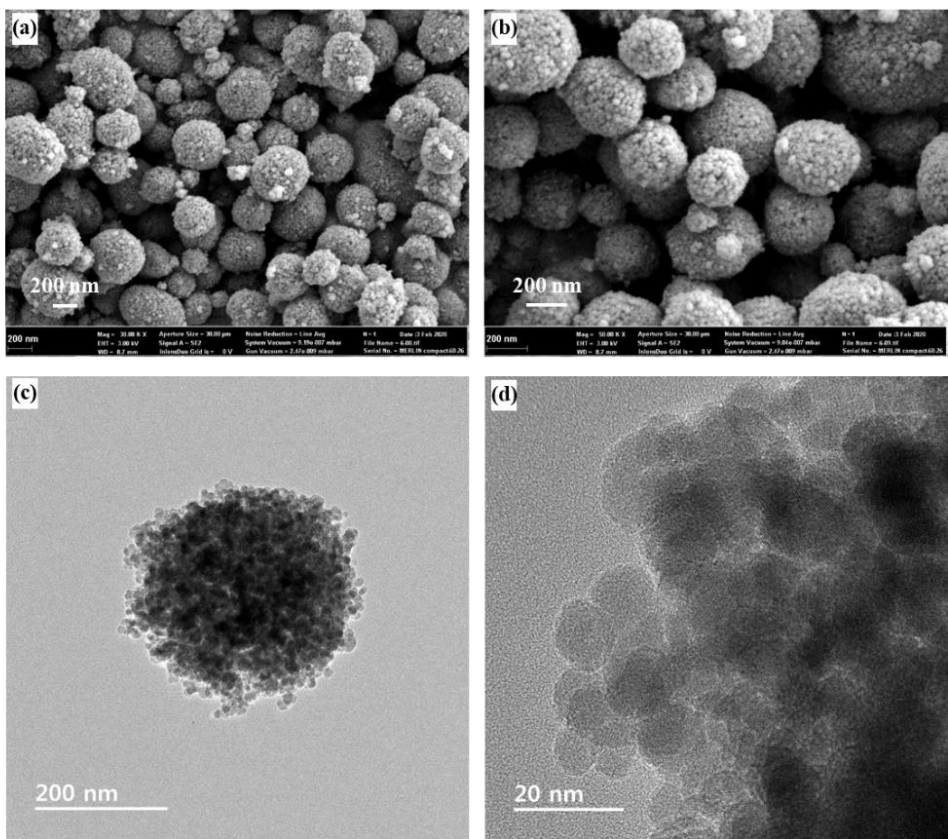


Figure 4. 2. SEM ((a) and (b)) and TEM ((c) and (d)) images of HS- Fe_3O_4 particles.

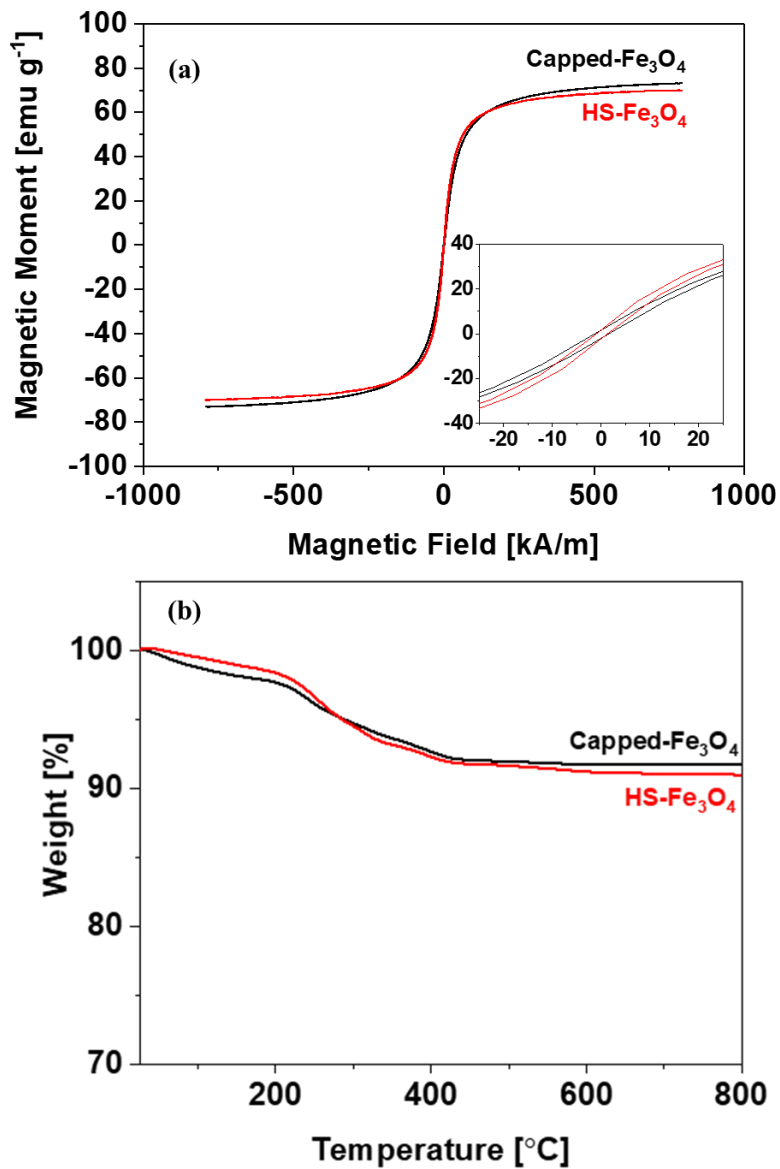


Figure 4. 3. (a) VSM curves for capped Fe₃O₄ and HS-Fe₃O₄ (the inset shows that all particles have a low coercive field). (b) TGA profiles of capped Fe₃O₄ and HS-Fe₃O₄.

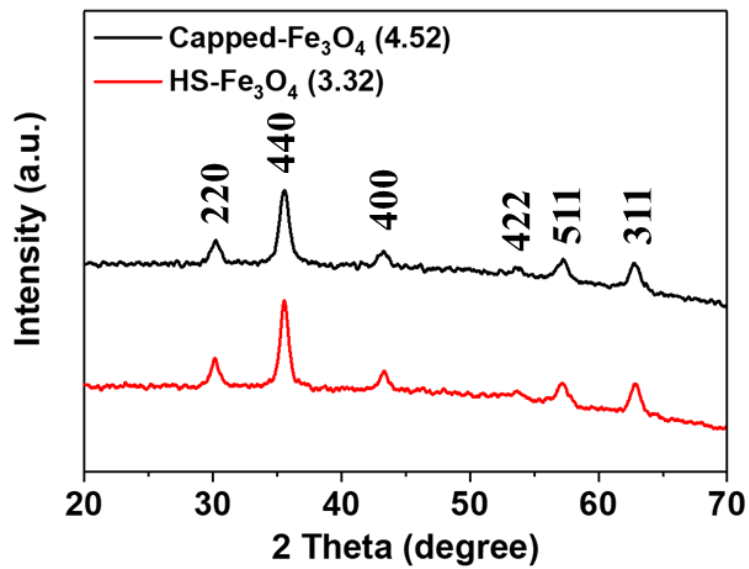


Figure 4. 4. XRD patterns for capped-Fe₃O₄ and HS-Fe₃O₄.

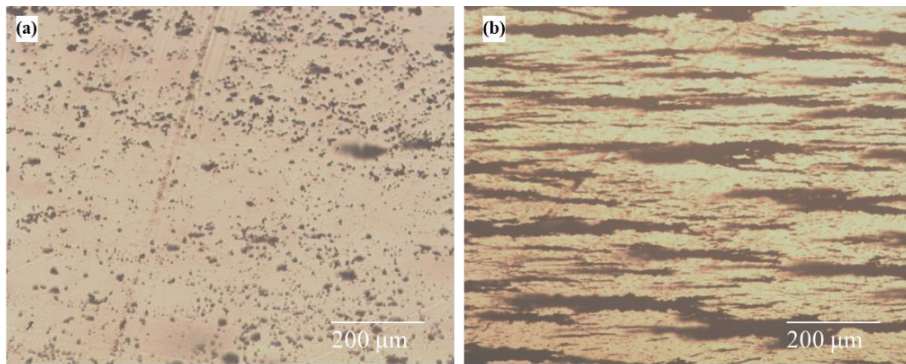


Figure 4. 5. Optical microscopic images of microstructural change for HS-Fe₃O₄ suspension. (a) before and (b) after application of the external magnetic field of 86 kA/m.

4. 3. 2. Magnetorheological properties

Viscoelastic properties of the two suspensions were investigated by observing the change in the modulus of the two suspensions with shear strain (amplitude sweep) and angular frequency (frequency sweep). Figure 4.6 (a) illustrates the results of amplitude sweep measurements under two magnetic field strengths (86 and 343 kA/m) in the strain range from 0.001% to 100%. As observed, the storage modulus for the capped Fe_3O_4 suspension was higher for both field strengths due to the higher magnetization and density for capped Fe_3O_4 . The storage modulus increased with the field strength due to the increased magnetic dipole–dipole interaction between particles. For a low strain range from 0.001 to 0.02%, a plateau region, called the linear viscoelastic (LVE) region where the storage modulus is independent of the strain, was observed for both suspensions in two field strengths. [5] The chain-like structures are maintained in the LVE range, regardless of the external strain. After the LVE range, the storage modulus decreased with strain as the structures start to be destroyed. [5,27] Figure 4.6 (b) shows the frequency sweep results of the two suspensions with a frequency from 1 to 100 rad/s. Like the amplitude sweep results, the storage modulus was higher for the suspension of the capped Fe_3O_4 particles. For both suspensions, the storage modulus of each suspension was 1 order higher than its loss modulus, which demonstrates that the solid-like elastic properties dominate in the formation of chain-like structures under a magnetic field. [45] These structures were not disturbed during the frequency sweep tests regardless of the sample species due to the strong magnetic polarization in the particles, so that the storage moduli of both suspensions did not show

remarkable change with angular frequency. [27]

The shear stress and viscosity of MR suspensions are shown in Figure 4.7 (a) as a function of shear rate at two different magnetic field strengths. The MR behavior is determined by field-induced dipole interaction between particles and hydrodynamic stress due to the external shear stress. [5,46] The behavior can be explained by dividing the shear rate into two areas. If the field-induced interaction dominates the hydrodynamic stress in the low shear rate region, the fibril-like structures retain their structures and an apparent change in shear stress with the shear rate is not observed, as in the viscoelastic region in the strain amplitude sweep test (Figure 4.6 (a)). [5,27] In some cases, the chain-like structures are destroyed and re-formed, which leads to a distinct decrease and subsequent recovery of shear stress. [28] Though this is not observed in our result, it is usually observed in electrorheological (ER) fluids where chain-like structures are not strong enough. This shows robustness of the meso-structures in the low shear rate region. [47,48] The hydrodynamic stress increases with the shear rate, and when the hydrodynamic stress exceeds the field-induced interaction, the fibril structures are completely destroyed and the shear stress increases with the shear rate. [27] Similar to the results of strain amplitude and angular frequency tests, shear stress of the HS-Fe₃O₄ suspension at low shear rate region was lower than that of the capped Fe₃O₄ suspension due to the lower magnetization and the lower Fe₃O₄ content in the suspension. Figure 4.7 (b) shows the viscosity of the two suspensions with the shear rate. In both suspensions, the viscosity decreases with the shear rate, which corresponds to the shear thinning behavior. Because the viscosity is expressed

as $\tau/\dot{\gamma}$ (shear stress/shear rate), the shear viscosity of the suspensions has the same order as the shear stress. The magnitude of the viscosity for capped Fe_3O_4 was larger, the same as the shear stress.

To assess the MR performance of the two suspensions more directly, the suspensions' yield stresses were obtained by using both theoretical and experimental methods. In MR fluid systems, two different yield stresses (static yield stress (τ_{sy}) and dynamic yield stress (τ_{dy})) can be determined depending on the theoretical model. The dynamic yield stress is the stress when the suspension is under the condition of the complete destruction of chain-like structures. [46,49] Theoretically, it can be predicted by the Bingham fluid model:

$$\tau = \tau_{dy} + \eta_{pl}\dot{\gamma} \quad (1)$$

where τ is the shear stress in shear stress vs shear rate curve, τ_{dy} is the dynamic yield stress, η_{pl} is the plastic viscosity, and $\dot{\gamma}$ is the shear rate [49,50]. The dynamic yield stress can be obtained by extrapolating the shear stress curve to zero shear rate. [28,29] However, this model cannot reflect the structural change of destruction and re-formation in the low shear rate range [51]. As we explained in our previous study, the yield stress of the MR fluid should be the static yield stress because it is the minimum stress required to start the flow of the suspension [46]. To determine the static yield stress at which flow of suspension starts, the Seo–Seo model was proposed: [47,51,52]

$$\tau = \tau_{sy} \left(1 - \frac{(1 - \exp(-a\dot{\gamma}))}{(1 + (a\dot{\gamma})^\alpha)} \right) + \eta_{pl}\dot{\gamma} \quad (2)$$

where τ_{sy} is the static yield stress at low shear rate, η_{pl} is the plastic viscosity, α is the

time constant corresponding to the reciprocal of the critical shear rate for an aligned mesostructure deformation, and α is the power-law index for the degree of shear thinning. [19,46] This model can correctly predict the static yield stress as well as it includes the dynamic yield stress predicted by the Bingham fluid model for $a = 0$. [47,50] The static yield stress can be measured experimentally with the controlled shear stress (CSS) mode. The CSS test measures the viscosity of the MR fluid against the shear stress and determines the static yield stress at the point of the sudden decrease in viscosity where the suspensions starts to flow. [27,28] Figure 4.8 shows the result of CSS tests for capped Fe_3O_4 and HS- Fe_3O_4 fluids. At low shear stress, the viscosity maintains a high value and then suddenly drops by a few orders of magnitude at a static yield point. Theoretically predicted dynamic and static yield stresses and experimentally observed static yield stress values are summarized and compared in Table 4.1. For both suspensions, all the three yield stress values were similar to one another, which means the robustness of chain-like structures at low shear stress. If the chain-like structures are strong enough to withstand the shear stress, the destruction and re-formation do not occur at low shear rate range. Thus, the dynamic and static yield stress values are close to each other. [29] The suspension starts to flow when the structures start to be destroyed. When compared to our previous results on h-PDVB/ Fe_3O_4 and f-PS/ Fe_3O_4 MR suspensions, the yield stresses of the present HS- Fe_3O_4 suspension are much higher. [28,29] At a field strength of 86 kA/m, the measured static yield stress of the HS- Fe_3O_4 fluid is 340 and 450% larger than that of h-PDVB@ Fe_3O_4 and f-PS/ Fe_3O_4 fluids, respectively. Although the density of HS- Fe_3O_4 ($\rho = 3.32 \text{ g/cm}^3$) is higher than that of the h-PDVB@ Fe_3O_4 ($\rho = 1.83 \text{ g/cm}^3$) and f-PS/ Fe_3O_4 ($\rho = 1.82$

g/cm³) particles, the ratio of the yield stress between HS-Fe₃O₄ suspension and the other two suspensions is higher than the ratio of the densities. As mentioned with VSM results, M_s of Fe₃O₄ is comparable to that of capped Fe₃O₄ because only air in the pores or cavity is the reason for density decrease. In contrast, since polymers occupy a considerable portion of h-PDVB@Fe₃O₄ and f-PS/Fe₃O₄, they have much lower M_s than the primary Fe₃O₄ particles. Such a difference in the composition of magnetic particles causes the large difference in their magnetization and the ensuing yield stress of MR fluids.

To check whether the formation of chain-like structures and the resulting change in the rheological properties are reversible with the magnetic field, a change in the shear stress when the magnetic field is switched on and off was observed. Figure 4.9 shows results of reversibility tests with the magnetic field at a shear rate of 1 s⁻¹. When the magnetic field is applied, a sudden increase in the shear stress was observed which ascribes the transition from the liquid-like state to the solid-like state was occurring whereas the reverse transition occurs once the magnetic field is turned off. When the maximum shear stresses for each turn are compared, they show very similar values to each other. They are in agreement with the static yield stress values in Table 4.1.

Figure 4.10 shows the yield stress vs the magnetic field strength on a log–log scale. Both suspensions yield stresses following the power-law relationship $\tau_{\sigma y} \propto H^m$. [5-7,27] They show the same magnetic field strength dependence with the slope of 2.0 ($\tau_{\sigma y} \propto H^2$), which implies that they follow the magnetic polarization model. [5,52]. Although the HS-Fe₃O₄ particles contain pores or voids, the polarization properties of Fe₃O₄ particles were not

affected by the pores or a cavity in the HS composite particles. The vertical movement of the static yield stress of HS-Fe₃O₄ particle suspension makes an exact overlap with that of the capped Fe₃O₄ particle suspension. This is a natural outcome since the pore or a cavity in the HS-Fe₃O₄ particle shows no MR activity at all, while the entire MR response originates from the Fe₃O₄ phase. The presence of the pore or a cavity in the HS-Fe₃O₄ particle only changed the magnitude of the yield stress, but its MR response remains the same. By the same token, the change in the yield stress with the magnetic field strength for HS-Fe₃O₄ fluid was more similar to that of the h-PDVB/Fe₃O₄ suspension than that of foamed PS/Fe₃O₄. [28,29] The change in yield stress for h-PDVB/Fe₃O₄ with field strength was smaller than that of foamed PS/Fe₃O₄. The differences between Fe₃O₄ particles that make up these composite particles are the shape and domain size of the Fe₃O₄ particles. For h-PDVB/Fe₃O₄, it is spherical Fe₃O₄ particles of relatively small size (10–20 nm), while foamed PS/Fe₃O₄ contains cubic Fe₃O₄ of larger size (50–100 nm). [28,29] Capped Fe₃O₄ particles which comprise the HS-Fe₃O₄ are spherical particles with a similar size to h-PDVB@Fe₃O₄, which leads to a similar response of the HS-Fe₃O₄ suspension to the magnetic field strength with the h-PDVB@Fe₃O₄ suspension.

Under a sufficiently strong magnetic field, the behavior of an MR fluid is governed by the magneto-polarization force and the hydrodynamic force. This dependence can be represented as the ratio of the hydrodynamic drag and the magneto static forces acting on the particles, called the Mason number, $M_n = 8\eta_0\dot{\gamma}/\mu_0\mu_c\beta^2 M^2$, where $\dot{\gamma}$ is the shear rate, η_0 is the medium viscosity, β is the contrast factor ($= (\mu_p - \mu_c)/(\mu_p + 2\mu_c)$), μ_p is the

particle relative permeability, μ_c is the relative permeability of the liquid medium phase, $\mu_0 = 4\pi \times 10^{-7} \text{ N}/\text{\AA}^2$ is the vacuum permeability, and M is the magnetic field strength. [52,54] In this equation, the numerator term $\eta_0\dot{\gamma}$ corresponds to the hydrodynamic force under continuous shear and the denominator including M^2 is proportional to the magnetic polarization force. [54] Thus, it is possible to express the behavior of suspensions with a single independent variable corresponding to $\dot{\gamma}/M^2$, a ratio between the hydrodynamic force and the polarization force. [54,55] Under a fixed particle concentration, a master curve for the specific viscosity (ratio of the apparent viscosity to medium viscosity) and volume fraction correction versus $\dot{\gamma}/M^2$ at different magnetic field strengths can be obtained, and the behaviors of different MR fluids can be compared. [55,56] Figure 4.11 shows the corrected viscosity curve versus $\dot{\gamma}/M^2$ for the capped Fe_3O_4 and the HS- Fe_3O_4 suspensions at two different magnetic field strengths. All the data could be overlapped with each other, which means the behaviors of the two suspensions were the same as following the same scaling law. This verifies that the ES process does not affect the MR behavior of suspensions. If we compare these data with our previous studies of f-PS/ Fe_3O_4 and h-PDVB@ Fe_3O_4 suspensions, we could observe that those curves overlapped well with the MR data in the present work, confirming the validity of the MR performance of these fluids. [27,29]

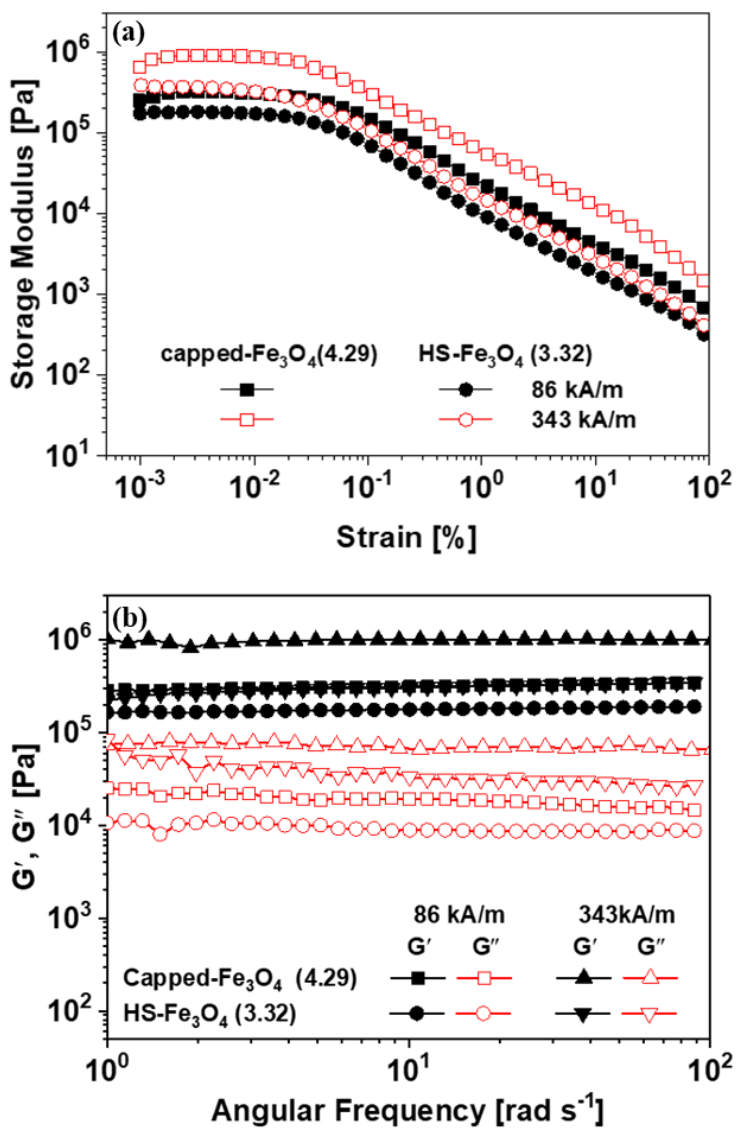


Figure 4. 6. (a) amplitude sweep (strain dependence) of storage modulus, G' and (b) Frequency sweep (frequency dependence) of storage modulus (G') and loss modulus(G'') for capped Fe₃O₄ and HS-Fe₃O₄ suspension at 86 kA/m and 343 kA/m.

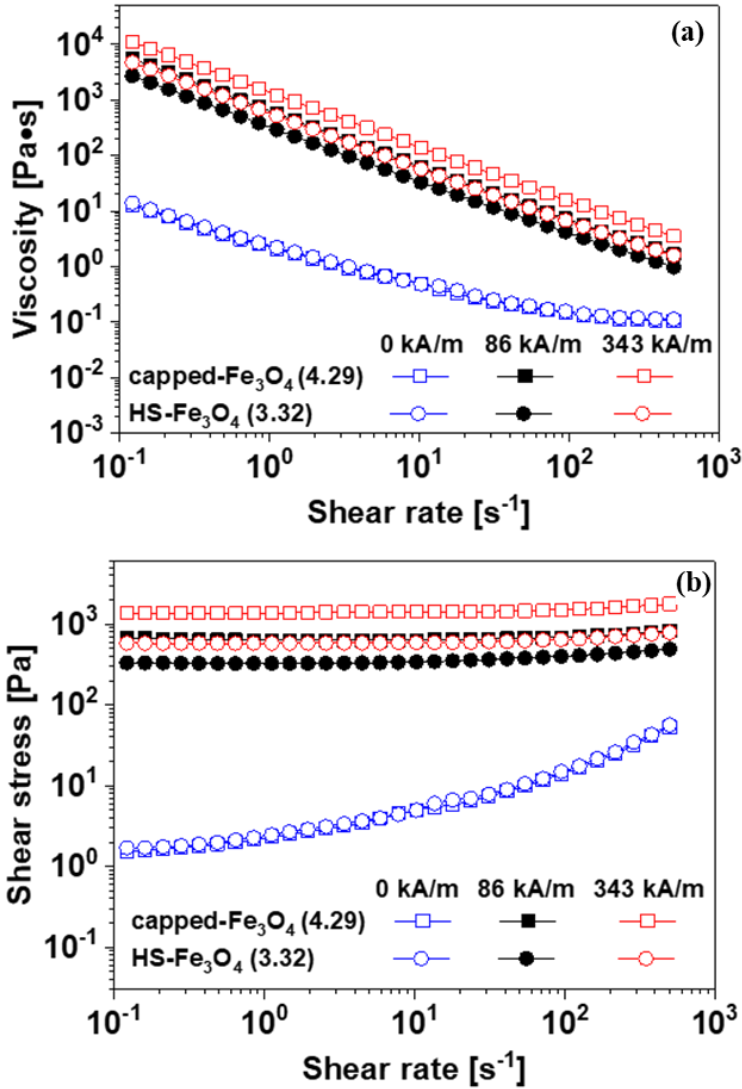


Figure 4. 7. (a) shear stress and (b) viscosity curves as a function of shear rate for MR fluids of capped-Fe₃O₄ and HS-Fe₃O₄.

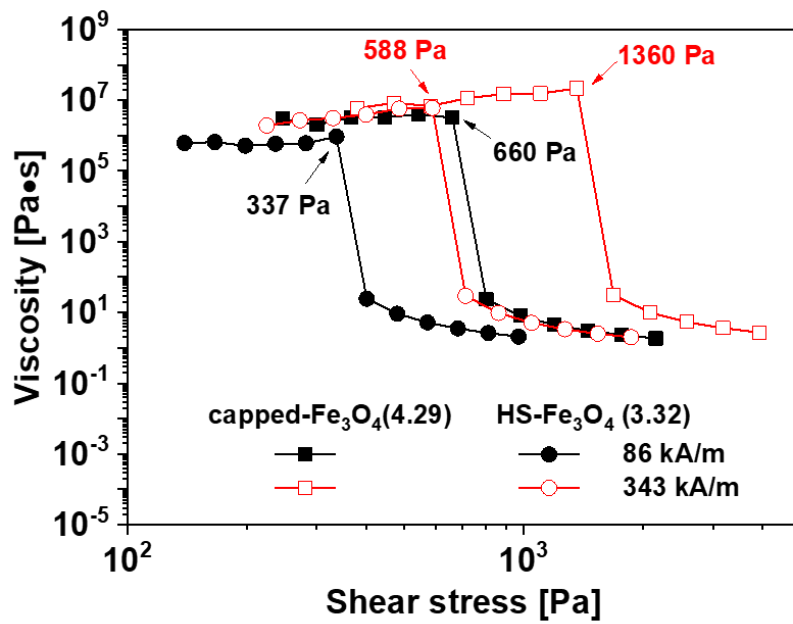


Figure 4. 8. Shear viscosity as a function of shear stress for capped-Fe₃O₄ and HS-Fe₃O₄ MR fluids at 86 kA/m and 343 kA/m.

Table 4. 1. Static yield stress and dynamic yield stress of Fe₃O₄ composites-based MR suspensions

	Yield stress (Pa)					
	M = 86 (kA/m)			M = 343 (kA/m)		
	Static exp (τ_{sy})	Dynamic (τ_{dy})	Static SS (τ_{sy})	Static exp (τ_{sy})	Dynamic (τ_{dy})	Static SS (τ_{sy})
Capped Fe ₃ O ₄ (4.29 g/cm ³)	660	640	684	1360	1394	1391
HS-Fe ₃ O ₄ (3.32 g/cm ³)	337	338	338	588	584	585
f-PS/Fe ₃ O ₄ (1.82 g/cm ³) ^{33, a)}	74	70	74	293	285	297
h-PDVB@Fe ₃ O ₄ (1.83 g/cm ³) ³⁴	100	105	105	185	190	180

^{a)} The original particle concentration for f-PS/Fe₃O₄ was converted to 10 vol% after taking into consideration of the Fe₃O₄ density difference.

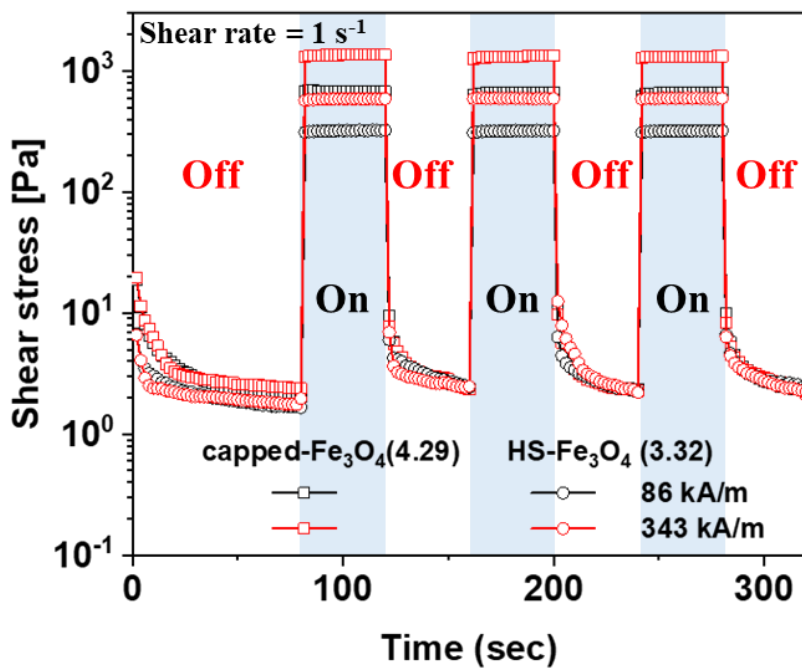


Figure 4. 9. Transient responses (reversibility) of the capped- Fe_3O_4 and HS- Fe_3O_4 MR fluids at shear rate of 1 s^{-1} .

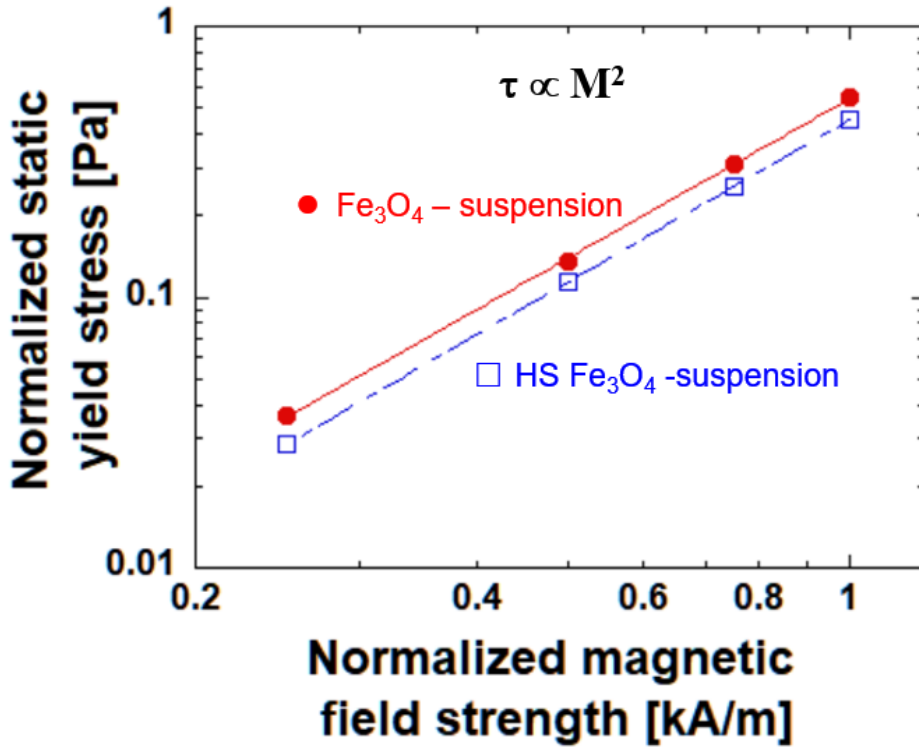


Figure 4. 10. Normalized static yield stress obtained from the fits to the Seo–Seo model (Eq. (2)) versus the normalized magnetic field strength. The lines show the quadratic dependence fits. ($\tau_{sy} = 0.543 \cdot H^2 + 0.448$ for the capped Fe_3O_4 particle suspension (\bullet), whereas $\tau_{sy} = 0.455 \cdot H^2 + 0.544$ for the HS- Fe_3O_4 particle suspension; H is the normalized magnetic field strength).

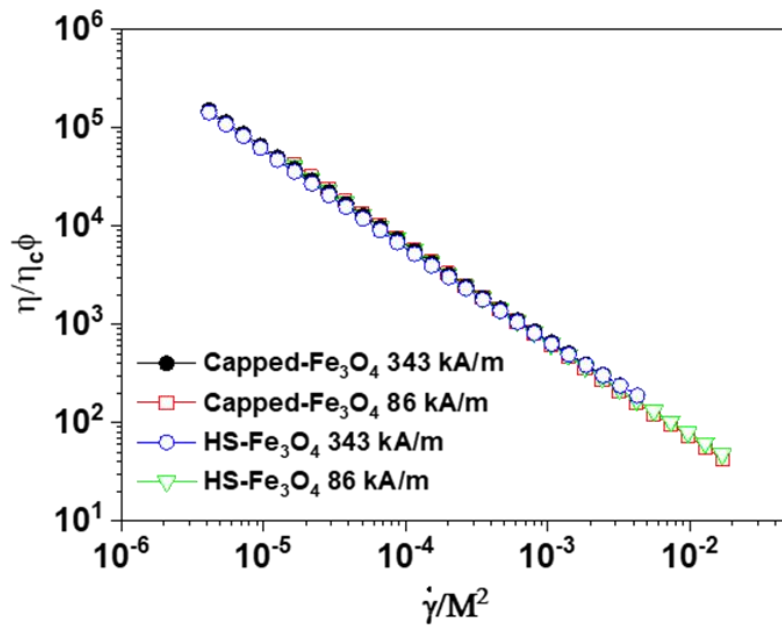


Figure 4. 11. Dimensionless apparent viscosity of the MR fluids as a function of $\dot{\gamma}/M^2$ at various magnetic field strengths.

4. 3. 3. Long-term Stability of Suspensions

The stability of capped Fe₃O₄ and HS-Fe₃O₄ MR suspensions was checked with the time change of the light transmission through the Turbiscan. For suspension in which spherical particles are dispersed, the particle's sedimentation velocity is theoretically expressed as the equation. [27,57]

$$V(\phi, d) = \frac{|\rho_p - \rho_c| \times g \times d^2}{18 \times \nu \times \rho_c} \cdot \frac{[1 - \phi]}{\left[1 + \frac{4.6\phi}{(1 - \phi)^3}\right]}$$

where V is the particle migration velocity (m s⁻¹), ρ_p presents the particle density, ρ_c is the continuous phase density (kg m⁻³), ν denotes the kinematic viscosity of continuous phase, g is the gravity constant (9.81 m s⁻²), d is the particle diameter, and ϕ represents the volume fraction of the particles. According to the preceding equation, the particle size has a big influence on the particle's settling velocity in the case of a hard sphere. However, the surface morphology of HS-Fe₃O₄ is quite bumpy and rough because they are the secondary particles made of the primary Fe₃O₄ particles. Taking into account the rough surface of HS- Fe₃O₄ particles (Figure 4.2) which resists against the sedimentation because of more friction in the liquid medium, it offsets the effect of the larger particle size. [27,29] Another important factor determining the sedimentation velocity of particles in MR fluids is the density mismatch between the magnetic particles and the carrier, $|\rho_p - \rho_c|$, term. [28,54. The sedimentation profiles of the capped Fe₃O₄ and HS-Fe₃O₄ are shown in Figure 4.12. In both samples, the light transmission increases very quickly within 2 h and remains almost unchanged up to 24 h. The final transmission value of the capped Fe₃O₄ suspension was

82%, while that of HS-Fe₃O₄ was only 45% due to the reduced density of HS- Fe₃O₄. Low-density particles are naturally more stable due to smaller density mismatch; they are suspended longer in the liquid medium than bare Fe₃O₄ nanoparticles. Although the stability of HS-Fe₃O₄ in suspension is worse than the Fe₃O₄-based composite particles in our previous works, [28,29] it is certainly better than the MR fluid of capped Fe₃O₄ particles, and its performance is much better than those of Fe₃O₄-based composite particle suspensions. This result opens up the possibility of producing structured particles with better stability and high performance in MR fluids without using lightweight materials.

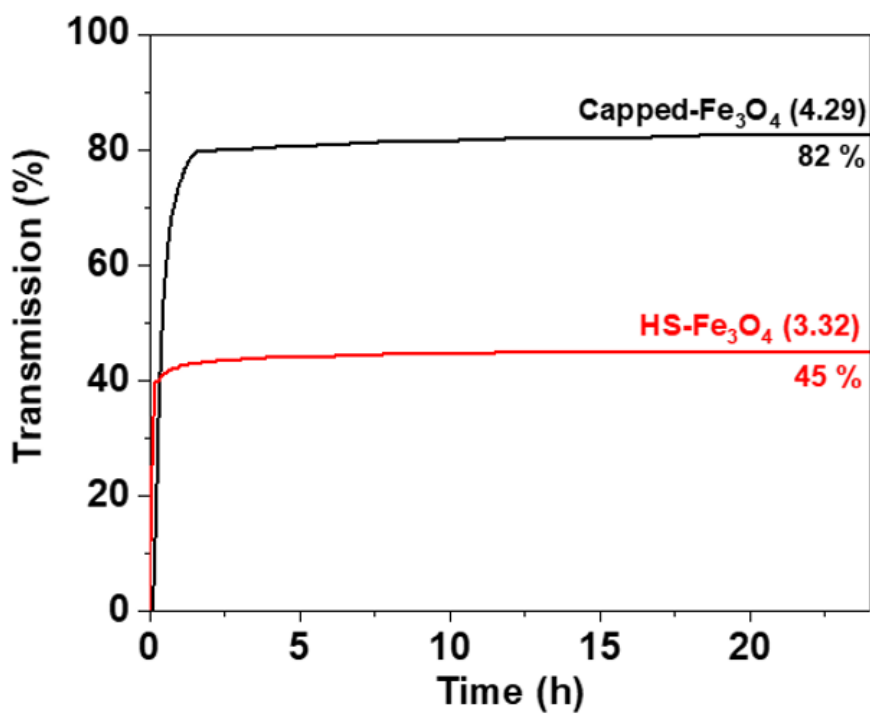


Figure 4. 12. Transmission (%) curve as a function of time (h) for capped-Fe₃O₄ and HS-Fe₃O₄ particles for 24h.

4. 4. Conclusions

In this study, a viable method for the preparation of well-performing and quite stable MR suspensions is offered. A simple electrospray technique enables easy preparation of hierarchically structured (HS)-Fe₃O₄ particles without using any light materials such as polymers, SiO₂ or carbon materials. Submicrometer-sized HS- Fe₃O₄ particles have a density of 3.32 g cm⁻³, significantly lower than that of capped Fe₃O₄ particles (4.29 g cm⁻³) due to the pores in the hierarchical structure. No inclusion of magnetically inactive materials in the structure makes HS-Fe₃O₄ particles have a high magnetization value, very close to the primary capped Fe₃O₄ nanoparticles. While maintaining the magnetization, the MR suspension of HS-Fe₃O₄ particles shows high yield stress values of 337 and 588 Pa at the field strength of 86 and 343 kA/m, respectively. The yield stress value at 86 kA/m is about 450 and 340% greater than that of foamed PS/Fe₃O₄ and h-PDVB@Fe₃O₄ MR fluids in our previous works. [29,48] At the same time, reducing the density of magnetic particles enables submicrometer-sized HS-Fe₃O₄ to have a better long-term stability (more than 3 times) than the MR suspension of capped Fe₃O₄ particles. These results illustrate the usefulness of the electrospray process, which does not require a high temperature process or additional materials, in the production of submicrometer-sized HS particles with pores or a cavity therein. They are very useful for making MR fluids with high performance and good long-term stability. Nevertheless, there is a need for improvement in the production of hierarchically structured magnetic particles with

lower density to achieve better long-term stability and higher performance, which will expand the practical application of more diverse MR fluid systems.

References

- (1) Ahamed R.; Choi S.B.; Ferdous M., A state of art on magneto-rheological materials and their potential applications, *J. Intellig. Mat. Syst. Struct.* **2018**, 29(10) 2051-2095
- (2) Lee, S.; Noh, J.; Hong, S.; Kim, Y. K.; Jang, J., Dual stimuli-responsive smart fluid of graphene oxide-coated iron oxide/silica core/shell nanoparticles. *Chem. Mater.* **2016**, 28 (8), 2624-2633.
- (3) Seiffert, S.; Thiele, J.; Abate, A. R.; Weitz, D. A., Smart microgel capsules from macromolecular precursors. *J. Am. Chem. Soc.* **2010**, 132 (18), 6606-6609.
- (4) Tavacoli, J. W.; Thijssen, J. H.; Clegg, P. S., Particle-stabilized oscillating diver: a self-assembled responsive capsule. *Soft Matter* **2011**, 7 (18), 7969-7972.
- (5) Seo, Y. P.; Han, S.; Choi, J.; Takahara, A.; Choi, H. J.; Seo, Y., Searching for a stable high-performance magnetorheological suspension. *Adv. Mater.* **2018**, 30 (42), 1704769.
- (6) Kim, Y. J.; Liu, Y. D.; Seo, Y.; Choi, H. J., Pickering-emulsion-polymerized polystyrene/Fe₂O₃ composite particles and their magnetoresponsive characteristics. *Langmuir* **2013**, 29 (16), 4959-4965.
- (7) Ghaffari, A.; Hashemabadi, S. H.; Ashtiani, M., A review on the simulation and modeling of magnetorheological fluids. *J. Intell. Mater. Syst. Struct.* **2015**, 26 (8), 881-904.

- (8) Kim, Y. J.; Liu, Y. D.; Seo, Y.; Choi, H. J., Pickering-Emulsion-Polymerized Polystyrene/Fe₂O₃ Composite Particles and Their Magnetoresponse Characteristics. *Langmuir* **2013**, 29 (16), 4959-4965.
- (9) Tian, Y.; Jiang, J.; Meng, Y.; Wen, S., A shear thickening phenomenon in magnetic field controlled-dipolar suspensions. *Appl. Phys. Lett.* **2010**, 97 (15), 151904.
- (10) Santiago-Quiñonez, D. I.; Rinaldi, C., Enhanced rheological properties of dilute suspensions of magnetic nanoparticles in a concentrated amphiphilic surfactant solution. *Soft Matter* **2012**, 8 (19), 5327-5333.
- (11) López-López, M. T.; Gómez-Ramírez, A.; Rodríguez-Arco, L.; Durán, J. D.; Iskakova, L.; Zubarev, A., Colloids on the frontier of ferrofluids. Rheological properties. *Langmuir* **2012**, 28 (15), 6232-6245.
- (12) Park, B. J.; Fang, F. F.; Choi, H. J., Magnetorheology: materials and application. *Soft Matter* **2010**, 6 (21), 5246-5253.
- (13) Bitaraf, M.; Ozbulut, O. E.; Hurlebaus, S.; Barroso, L., Application of semi-active control strategies for seismic protection of buildings with MR dampers. *Eng. Struct.* **2010**, 32 (10), 3040-3047.
- (14) Chen, Z.; Wang, X.; Ko, J.; Ni, Y.; Spencer Jr, B. F.; Yang, G. In *MR damping system on Dongting Lake cable-stayed bridge*, Smart Structures and Materials 2003: Smart Systems and Nondestructive Evaluation for Civil Infrastructures, International Society for Optics and Photonics: 2003; pp 229-235.

- (15) Oliveira, F.; de Morais, P. G.; Suleman, A., Semi-active control of base-isolated structures. *Procedia Eng.* **2015**, *114*, 401-409.
- (16) Ashtiani, M.; Hashemabadi, S.; Ghaffari, A., A review on the magnetorheological fluid preparation and stabilization. *J. Magn. Magn. Mater.* **2015**, *374*, 716-730.
- (17) Choi, H. J.; Zhang, W. L.; Kim, S.; Seo, Y., Core-shell structured electro-and magneto-responsive materials: Fabrication and characteristics. *Materials* **2014**, *7* (11), 7460-7471.
- (18) Pu, H.; Jiang, F., Towards high sedimentation stability: magnetorheological fluids based on CNT/Fe₃O₄ nanocomposites. *Nanotechnology* **2005**, *16* (9), 1486.
- (19) Seo, Y. P.; Choi, H. J.; Seo, Y. , Analysis of the flow behavior of electrorheological fluids with the aligned structure reformation , *Polymer* , **2011**, *52* (25), 5695-5698
- (20) Cvek, M.; Mrlík, M.; Ilčíková, M.; Mosnačková, J.; Münster, L.; Pavlínek V.; Pavlínek, V.; Synthesis of Silicone Elastomers Containing Silyl-Based Polymer- Grafted Carbonyl Iron Particles: An Efficient Way To Improve Magnetorheological, Damping, and Sensing Performances. *Macromolecules* **2017**, *50* (5), 2189-2200.
- (21) Fang, F. F.; Choi, H. J.; Seo, Y., Sequential coating of magnetic carbonyliron particles with polystyrene and multiwalled carbon nanotubes and its effect on their magnetorheology. *ACS Appl. Mater. Interfaces.* **2010**, *2* (1), 54-60.

- (22) Cvek, M.; Mrlik, M.; Ilcikova, M.; Plachy, T.; Sedlacik, M.; Mosnacek, J.; Pavlinek, V., A facile controllable coating of carbonyl iron particles with poly(glycidyl methacrylate): a tool for adjusting MR response and stability properties. *J. Mater. Chem. C* **2015**, *3* (18), 4646-4656.
- (23) Pu, H. T.; Jiang, F. J.; Yang, Z.-l., Preparation and properties of soft magnetic particles based on Fe₃O₄ and hollow polystyrene microsphere composite. *Materials Chemistry and Physics* **2006**, *100* (1), 10-14.
- (24) Kim, H.; Kim, S.; Seo, Y., High-Performance Magnetorheological Suspensions of Fe₃O₄-deposited Carbon Nanotubes with Enhanced Stability. *MRS Adv.* **2019**, *4* (3-4), 217-224.
- (25) Du, Z.; Qiu, Y.; Niu, T.; Wang, W.; Ye, X.; Wang, J.; Zhang, W. L.; Choi, H. J.; Zeng, H., Bio-inspired passion fruit-like Fe₃O₄@C nanospheres enabling high-stability magnetorheological performances. *Langmuir* **2020**, *36* (26), 7706-7714.
- (26) Fang, F. F.; Kim, J. H.; Choi, H. J., Synthesis of core-shell structured PS/Fe₃O₄ microbeads and their magnetorheology. *Polymer* **2009**, *50* (10), 2290-2293.
- (27) Chuah, W. H.; Zhang, W. L.; Choi, H. J.; Seo, Y., Magnetorheology of core-shell structured carbonyl iron/polystyrene foam microparticles suspension with enhanced stability. *Macromolecules* **2015**, *48* (19), 7311-7319.
- (28) Han, S.; Choi, J.; Seo, Y. P.; Park, I. J.; Choi, H. J.; Seo, Y., High-performance magnetorheological suspensions of pickering-emulsion-polymerized polystyrene/Fe₃O₄ particles with enhanced stability. *Langmuir* **2018**, *34* (8), 2807-2814.

- (29) Choi, J.; Han, S.; Kim, H.; Sohn, E. H.; Choi, H. J.; Seo, Y., Suspensions of Hollow Polydivinylbenzene Nanoparticles Decorated with Fe₃O₄ Nanoparticles as Magnetorheological Fluids for Microfluidics Applications. *ACS Appl. Nano Mater.* **2019**, *2* (11), 6939-6947.
- (30) Hwang, D.; Lee, H.; Jang, S.-Y.; Jo, S. M.; Kim, D.; Seo, Y.; Kim, D. Y., Electro spray preparation of hierarchically-structured mesoporous TiO₂ spheres for use in highly efficient dye-sensitized solar cells. *ACS Appl. Mater. Interfaces.* **2011**, *3* (7), 2719-2725.
- (31) Lee, H.; Hwang, D.; Jo, S. M.; Kim, D.; Seo, Y.; Kim, D. Y., Low-temperature fabrication of TiO₂ electrodes for flexible dye-sensitized solar cells using an electro spray process. *ACS Appl. Mater. Interfaces.* **2012**, *4* (6), 3308-3315.
- (32) Chou, T. P.; Zhang, Q.; Fryxell, G. E.; Cao, G., Hierarchically Structured ZnO Film for Dye-Sensitized Solar Cells with Enhanced Energy Conversion Efficiency. *Adv. Mater.* **2007**, *19* (18), 2588-2592.
- (33) Kim, J.; Lee, H.; Kim, D. Y.; Seo, Y. Resonant Multiple Light Scattering for Enhanced Photon Harvesting in Dye-Sensitized Solar Cells. *Adv. Mater.* **2014**, *26* (30), 5192–5197
- (34) Huang, F.; Chen, D.; Zhang, X. L.; Caruso, R. A.; Cheng, Y. B., Dual-function scattering layer of submicrometer-sized mesoporous TiO₂ beads for high-efficiency dye-sensitized solar cells. *Adv. Funct. Mater.* **2010**, *20* (8), 1301-1305.

- (35) Zhang, Q.; Chou, T.; Russo, B.; Jenekhe, S.; Cao, G., Light scattering enhanced energy conversion efficiency in hierarchically-structured ZnO dye-sensitized solar cells. *Adv. Funct. Mater.* **2008**, *18*, 1654-1660.
- (36) Wang, C.; Zhang, X.; Cao, D.; Yin, H.; Li, X.; Cheng, P.; Mi, B.; Gao, Z.; Deng, W., In situ preparation of hierarchically structured dual-layer TiO₂ films by E-spray method for efficient dye-sensitized solar cells. *Org. Electron.* **2017**, *49*, 135-141.
- (37) Cheng, Q.; Pavlinek, V.; He, Y.; Yan, Y.; Li, C.; Saha, P., Synthesis and electrorheological characteristics of sea urchin-like TiO₂ hollow spheres. *Colloid. Polym. Sci.* **2011**, *289* (7), 799-805.
- (38) Li, C.; He, K.; Sun, W.; Wang, B.; Yu, S.; Hao, C.; Chen, K., Synthesis of hollow TiO₂ nanobox with enhanced electrorheological activity. *Ceram. Int.* **2020**.
- (39) Jaworek, A., Micro-and nanoparticle production by electrospraying. *Powder Technol.* **2007**, *176* (1), 18-35.
- (40) Li, X.; Zhang, Y.; Zhang, Z.; Zhou, J.; Song, J.; Lu, B.; Xie, E.; Lan, W., Electrospraying tuned photoanode structures for dye-sensitized solar cells with enhanced energy conversion efficiency. *J. Power Sources* **2011**, *196* (3), 1639-1644.
- (41) Zhang, Y. C.; You, Y.; Xin, S.; Yin, Y.-X.; Zhang, J.; Wang, P.; Zheng, X.-s.; Cao, F.-F.; Guo, Y. G., Rice husk-derived hierarchical silicon/nitrogen-doped carbon/carbon nanotube spheres as low-cost and high-capacity anodes for lithium-ion batteries. *Nano Energy* **2016**, *25*, 120-127.

- (42) Răcuci, M.; Creangă, D.; Airinei, A., Citric-acid-coated magnetite nanoparticles for biological applications. *Eur. Phys. J. E* **2006**, *21* (2), 117-121.
- (43) Mohammadi, A.; Barikani, M., Synthesis and characterization of superparamagnetic Fe₃O₄ nanoparticles coated with thiodiglycol. *Mater. Charact.* **2014**, *90*, 88-93.
- (44) Munjal, S.; Khare, N.; Sivakumar, B.; Sakthikumar, D. N., Citric acid coated CoFe₂O₄ nanoparticles transformed through rapid mechanochemical ligand exchange for efficient magnetic hyperthermia applications. *J. Magn. Magn. Mater.* **2019**, *477*, 388-395.
- (45) Upadhyay, R.; Laherisheth, Z.; Shah, K., Rheological properties of soft magnetic flake shaped iron particle based magnetorheological fluid in dynamic mode. *Smart Mater. Struct.* **2013**, *23* (1), 015002.
- (46) Seo, Y. P.; Seo, Y., Modeling and analysis of electrorheological suspensions in shear flow. *Langmuir* **2012**, *28* (6), 3077-3084.
- (47) Seo, Y. P.; Han, S.; Kim, J.; Choi, H. J.; Seo, Y., Analysis of the flow behavior of electrorheological fluids containing polypyrrole nanoparticles or polypyrrole/silica nanocomposite particles. *Rheol. Acta* **2020**, *59* (6), 415-423.
- (48) Han, S.; Choi, J.; Kim, H.; Kim, S.; Seo, Y. In *Static yield stress of a magnetorheological fluid containing pickering emulsion polymerized Fe₃O₄/polystyrene composite particles*, AIP Conf. Proc., AIP Publishing LLC: 2019; p 140001.
- (49) Farjoud, A.; Vahdati, N.; Fah, Y. F., Mathematical model of drum-type MR brakes using Herschel-Bulkley shear model. *J. Intell. Mater. Syst. Struct.* **2008**, *19* (5), 565-572.

- (50) Seo, Y. P.; Choi, H. J.; Seo, Y., A simplified model for analyzing the flow behavior of electrorheological fluids containing silica nanoparticle-decorated polyaniline nanofibers. *Soft Matter* **2012**, *8* (17), 4659-4663.
- (51) Seo, Y. P.; Choi, H. J.; Lee, J. R.; Seo, Y., Modeling and analysis of an electrorheological flow behavior containing semiconducting graphene oxide/polyaniline composite particles. *Colloids Surf. A Physicochem. Eng. Asp.* **2014**, *457*, 363-367.
- (52) Seo, Y. P.; Kwak, S.; Choi, H. J.; Seo, Y., Static yield stress of a magnetorheological fluid containing Pickering emulsion polymerized Fe₂O₃/polystyrene composite particles. *J. Colloid Interface Sci.* **2016**, *463*, 272-278.
- (53) Ruiz-López, J. A.; Fernández-Toledano, J. C.; Hidalgo-Alvarez, R.; de Vicente, J., Testing the mean magnetization approximation, dimensionless and scaling numbers in magnetorheology. *Soft Matter* **2016**, *12* (5), 1468-1476.
- (54) De Vicente, J.; Klingenberg, D. J.; Hidalgo-Alvarez, R., Magnetorheological fluids: a review. *Soft matter* **2011**, *7* (8), 3701-3710.
- (55) Shah, K.; Seong, M.-S.; Upadhyay, R.; Choi, S.-B., A low sedimentation magnetorheological fluid based on plate-like iron particles, and verification using a damper test. *Smart Mater. Struct.* **2013**, *23* (2), 027001.
- (56) Becnel, A. C.; Sherman, S.; Hu, W.; Wereley, N. M., Nondimensional scaling of magnetorheological rotary shear mode devices using the Mason number. *J. Magn. Magn. Mater.* **2015**, *380*, 90-97.
- (57) Mills, P.; Snabre, P., Settling of a suspension of hard spheres. *EPL* **1994**, *25* (9), 651-656.

Chapter 5. High-Performance Magnetorheological Fluids of Carbon Nanotube-CoFeNi Composites with Enhanced Long-Term Stability

5. 1. Introduction

Magnetorheological (MR) fluid is a suspension of magnetic particles in non-magnetic carrier medium and classified as a smart material due to its unique response to external magnetic field. [1-4] With external magnetic field, magnetic particles in MR fluid are aligned to the field direction due to magnetic dipole-dipole interaction, forming chain-like structures. [5,6] These structures inhibit the flow of MR fluid and increase the viscosity by several orders in very short time, resulting in transition from liquid-like to solid-like state. [5-9] This transition is reversible, and the rheological properties of MR fluid are easily controllable with magnetic field strength. [10,11] Such unique responsiveness and modifiability of rheological properties make MR fluid to be applicable to various devices like haptic devices, rotor dampers, power steering pumps where flow of fluids need to be controlled, and shock absorbers in motorcycles and large damping systems in building and bridges to protect the systems from external impacts. [11-16]

Despite of potential for industrial use, there is a major problem that inhibit the practical

use of MR fluid: poor long-term stability due to the fast sedimentation of magnetic particles. [1,3,16,17] Because of large density mismatch between magnetic particles and carrier medium, the particles quickly settle down to bottom, shortening MR fluid's life-time significantly. [18] As a solution for this problem many researchers have tried to magnetic composites by combining magnetic materials with low-density materials. [19-30] With this strategy, the researches fabricated magnetic composite particles with spherical shape and successfully reduced the density of magnetic particles and improved the long-term stability of MR suspensions. Of the composites, carbon nanotube (CNTs)-based magnetic composites have some distinct characteristics compared to composites with spherical shapes. CNT-based magnetic composites have very high aspect ratio, and this can contribute to long-term stability of MR fluids. When CNTs are dispersed in carrier medium with sufficiently high volume concentration, it is known that they can form 3-dimensional network-like structures. [31,32] For MR fluids, this phenomenon was observed for CNT-Fe₃O₄-based MR suspensions, which exhibit enormously excellent long-term stability due to self-supporting effect of CNT-Fe₃O₄ composites. [33,34]

Another issue about composites for MR fluids is their MR performance. The use of magnetically-inactive materials for fabrication of the composites leads to deterioration in magnetic properties, and resultant declination of MR performance (storage modulus, yield stress and viscosity etc.). As a solution for this problem, we fabricated hierarchically-structured Fe₃O₄ (HS-Fe₃O₄) nanoparticles which does not have non-magnetic polymers using simple electrospray process. [35] The secondary HS-Fe₃O₄ showed saturation

magnetization value comparable to its primary Fe_3O_4 nanoparticles while having lower density due to pores among the primary particles. These characteristics enabled HS- Fe_3O_4 -based MR suspensions to have high MR performance and excellent long-term stability at the same time.

An easier way to obtain high performance for MR fluids would be the use of magnetic materials with superior magnetic properties like carbonyl iron (CI) which has been used for MR fluids in previous researches. [19,28,36] However, unlike iron-based oxide materials (Fe_3O_4 , CoFe_2O_4 and NiFe_2O_4), CI is hard to synthesize in nano size. Thus, it is hard to prepare CI-based composites with various morphologies. In a previous study, Reddy et al have fabricated CoFeNi alloy nanoparticles with different stoichiometric ratio of Co Fe and Ni using hydrazine monohydrate as reducing agent. [37] Not only these alloys had very high magnetization values with maximum of 138 eum/g for $\text{Co}_{0.4}\text{Fe}_{0.4}\text{Ni}_{0.2}$, the synthesis procedure was very simple, similar to co-precipitation method with just additional injection of hydrazine monohydrate.

In this study, for simultaneous achievement of high performance and long-term stability in MR fluids, we fabricated CNT- $\text{Co}_{0.4}\text{Fe}_{0.4}\text{Ni}_{0.2}$ composite. With the use of $\text{Co}_{0.4}\text{Fe}_{0.4}\text{Ni}_{0.2}$, the composite showed much higher saturation magnetization value than Fe_3O_4 composites and bare Fe_3O_4 particles we have previously used for MR suspensions, leading to greatly enhanced MR performance of CNT- $\text{Co}_{0.4}\text{Fe}_{0.4}\text{Ni}_{0.2}$ suspension. In addition, CNTs made CNT- $\text{Co}_{0.4}\text{Fe}_{0.4}\text{Ni}_{0.2}$ to have relatively lower density compared to $\text{Co}_{0.4}\text{Fe}_{0.4}\text{Ni}_{0.2}$ and high aspect ratio. The reduced density mismatch between the composite and carrier medium,

combined with formation of network structures in suspension resulted in greatly enhanced long-term stability.

5. 2. Experimental Section

5. 2. 1. Functionalization of Carbon Nanotubes

To introduce sites for anchoring of $\text{Co}_{0.4}\text{Fe}_{0.4}\text{Ni}_{0.2}$, multi-walled carbon nanotubes (MWCNTs) were oxidized with mixed solution of H_2SO_4 and HNO_3 . [34] 1 g of MWCNTs were added in 400 ml of $\text{H}_2\text{SO}_4/\text{HNO}_3$ (3:1, v:v ratio) mixed solution and the mixture was heated to 60 °C for 8 h. The oxidized sample was filtered, washed with water and ethanol several times, and finally dried in vacuum at room temperature. Oxidized CNTs (1 g) was dispersed in ethylenediamine (500 ml) for additional functionalization with amine groups. [38] The dispersion was mildly sonicated for 3 h at 35 °C. After functionalization, the sample was filtered, washed and dried under vacuum.

5. 2. 2. Synthesis of $\text{Co}_{0.4}\text{Fe}_{0.4}\text{Ni}_{0.2}$ and CNT- $\text{Co}_{0.4}\text{Fe}_{0.4}\text{Ni}_{0.2}$

Figure 5.1 is the schematic diagram for synthesis of CNT- $\text{Co}_{0.4}\text{Fe}_{0.4}\text{Ni}_{0.2}$ composites. $\text{Co}_{0.4}\text{Fe}_{0.4}\text{Ni}_{0.2}$ nanoparticles were synthesized according to a previous study with some modification to the process. [37] Stoichiometric amount of $\text{CoCl}_2 \cdot 6\text{H}_2\text{O}$ (4.953 g), FeCl_2

4H₂O (4.137 g), and Ni(NO₃)₂ 6H₂O (3.027 g) were dissolved to mixture of ethanol and H₂O (300 ml, 3:1 v:v ratio) under nitrogen atmosphere. The molar ratio of CoCl₂ 6H₂O, FeCl₂ 4H₂O, and Ni(NO₃)₂ 6H₂O was 0.4:0.4:0.2. After complete dissolution, 6 M NaOH solution (5.8 ml) was injected to the solution and heated to 80 °C. When the temperature reached 80 °C, hydrazine monohydrate (30 ml) was slowly injected, nitrogen flow was removed, and the reaction was progressed for 45 mins. After the reaction mixture was cooled, Co_{0.4}Fe_{0.4}Ni_{0.2} were collected with permanent magnet, washed with water and ethanol repeatedly to remove residual NaOH and hydrazine, and dried in vacuum at room temperature. CNT-Co_{0.4}Fe_{0.4}Ni_{0.2} composites were synthesized with same process with functionalized CNTs (1.5 g) dispersed in ethanol/H₂O beforehand. The expected weight ratio between CNT and Co_{0.4}Fe_{0.4}Ni_{0.2} in CNT-Co_{0.4}Fe_{0.4}Ni_{0.2} was 1:2.

5. 2. 3. Characterization

The surface morphologies of Co_{0.4}Fe_{0.4}Ni_{0.2} and CNT-Co_{0.4}Fe_{0.4}Ni_{0.2} were observed with scanning electron microscopy (SEM; JSM-7600F, JEOL, Tokyo, Japan) and transmission electron microscopy (TEM; JEM-2100F, JEOL Ltd, Tokyo, Japan). The densities of magnetic particles were measured with helium pycnometer (AccuPyc 1330, Micromeritics Instrument Corporation, Norcross, USA). The metal species of Co_{0.4}Fe_{0.4}Ni_{0.2} were characterized with X-ray diffractometer (XRD; D8-Advance, Bruker, USA). The magnetic properties of Co_{0.4}Fe_{0.4}Ni_{0.2} and CNT-Co_{0.4}Fe_{0.4}Ni_{0.2} were measured using a vibrating sample magnetometer (VSM; VSM-7410, Lake Shore Cryotronics, USA) from -10 kOe to

10 kOe magnetic field range.

MR fluids for further tests were fabricated by dispersing $\text{Co}_{0.4}\text{Fe}_{0.4}\text{Ni}_{0.2}$ or CNT- $\text{Co}_{0.4}\text{Fe}_{0.4}\text{Ni}_{0.2}$ in silicone oil (KF-96, 10 cS, Shin Etsu, Japan) as a medium with particles concentration of 10 vol%. Formation of chain-like structures under magnetic field was observed with optical microscope (Olympus BX-51) equipped with a CCD camera. MR properties of the suspensions were characterized using a rotational rheometer (Physica MCR301, Stuttgart, Germany) equipped with a magnetic generator (Physica MRD 180, Stuttgart, Germany). Strain amplitude and frequency sweep (storage and loss modulus vs strain and angular frequency, respectively), flow (shear stress and viscosity vs strain rate), controlled shear stress (viscosity vs shear stress) and reversibility tests (shear stress with turning on and off magnetic field) were conducted. Finally, long-term stability of the MR fluids were examined with observing light transmission change for 24h using turbiscan (Classic MA2000, Formulation, France).

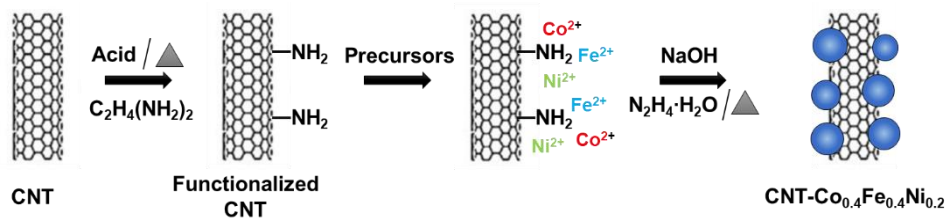


Figure 5. 1. Schematic diagram for synthesis of CNT-Co_{0.4}Fe_{0.4}Ni_{0.2}

5. 3. Results and Discussions

5. 3. 1. Morphologies and Structures

Figure 5.2 shows SEM and TEM images for functionalized CNTs and CNT-Co_{0.4}Fe_{0.4}Ni_{0.2}. SEM image (figure 5.2 (a)) of oxidized CNTs shows rather smooth surface of CNTs. When Co_{0.4}Fe_{0.4}Ni_{0.2} nanoparticles were synthesized with oxidized CNTs dispersed in solution mixture, (figure 5.2 (b)) they started to grow at specific surface site of oxidized CNTs and formed fruits' cluster-like aggregations. The functional groups introduced during oxidation and additional amination of CNTs acted as anchoring sites for Co_{0.4}Fe_{0.4}Ni_{0.2} nanoparticles, enabling attachment of Co_{0.4}Fe_{0.4}Ni_{0.2} particles on the surface of oxidized CNTs. With CNTs having density of 1.5 g/cm³, the density of CNT-Co_{0.4}Fe_{0.4}Ni_{0.2} decreased to 4.12 g/cm³ from 7.85 g/cm³ for Co_{0.4}Fe_{0.4}Ni_{0.2}.

The magnetic properties for Co_{0.4}Fe_{0.4}Ni_{0.2} and CNT-Co_{0.4}Fe_{0.4}Ni_{0.2} were examined with VSM profile (Figure 5.3). Unlike Fe₃O₄ and its composites which are superparamagnetic with a very narrow hysteresis curve and a small coercive field, Co_{0.4}Fe_{0.4}Ni_{0.2} and CNT-Co_{0.4}Fe_{0.4}Ni_{0.2} showed ferromagnetic character with some coercive field and remnant magnetization. The saturation magnetization (M_s) value for Co_{0.4}Fe_{0.4}Ni_{0.2} is 165 emu/g, which is much higher than Fe₃O₄ with M_s around 70-80 emu/g in our previous works. [30, 35] This value is even higher than Co_{0.4}Fe_{0.4}Ni_{0.2} in a previous work. [37] The reason for this improvement in M_s is attributed to nitrogen flow in the early stage of the synthesis which can prevent possible oxidation of intermediate

formed with the injection of NaOH solution during the reaction process. Due to very high M_s value of $\text{Co}_{0.4}\text{Fe}_{0.4}\text{Ni}_{0.2}$, CNT- $\text{Co}_{0.4}\text{Fe}_{0.4}\text{Ni}_{0.2}$ also shows high M_s value of 108 emu/g, which is much higher than Fe_3O_4 -based composite particles. The M_s value of 108 emu/g CNT- $\text{Co}_{0.4}\text{Fe}_{0.4}\text{Ni}_{0.2}$ is higher by over 2.5 times than CNT- Fe_3O_4 ($M_s = 42$ emu/g) in our previous work. [34] The weight ratio of CNT and $\text{Co}_{0.4}\text{Fe}_{0.4}\text{Ni}_{0.2}$ in the composite calculated from the M_s value is about 1:1.9, which is close to the ratio calculated from the amount of CNTs and precursors of $\text{Co}_{0.4}\text{Fe}_{0.4}\text{Ni}_{0.2}$ used in the synthesis.

To check whether the synthesis of $\text{Co}_{0.4}\text{Fe}_{0.4}\text{Ni}_{0.2}$ with the modification in this work was successful, crystal structure of $\text{Co}_{0.4}\text{Fe}_{0.4}\text{Ni}_{0.2}$ and CNT- $\text{Co}_{0.4}\text{Fe}_{0.4}\text{Ni}_{0.2}$ was investigated with XRD (Figure 5.4). For $\text{Co}_{0.4}\text{Fe}_{0.4}\text{Ni}_{0.2}$, peaks corresponding to (111), (110), (200), (022), (112), (113), (222) crystal planes were examined, showing successful synthesis of $\text{Co}_{0.4}\text{Fe}_{0.4}\text{Ni}_{0.2}$ species. Although peak for (113), (222) were not observed for CNT- $\text{Co}_{0.4}\text{Fe}_{0.4}\text{Ni}_{0.2}$ due to very weak signal, other peaks for $\text{Co}_{0.4}\text{Fe}_{0.4}\text{Ni}_{0.2}$ were observed, especially a BCC peak around 65° , which was not observed for other stoichiometric Co-Fe-Ni alloys in previous work. [37] Also, a peak around 25° for MWCNT was designated, proving successful synthesis of CNT- $\text{Co}_{0.4}\text{Fe}_{0.4}\text{Ni}_{0.2}$ composites.

The change in arrangement of CNT- $\text{Co}_{0.4}\text{Fe}_{0.4}\text{Ni}_{0.2}$ in suspension with magnetic field was observed with optical microscopy and shown in Figure 5.5. When magnetic field is off, CNT- $\text{Co}_{0.4}\text{Fe}_{0.4}\text{Ni}_{0.2}$ is in dispersed state while chain-like structures were formed along magnetic field direction as soon as magnetic field is turned on. These structures fill the gap between plates in rotational rheometer system, exhibiting transition of MR suspensions

from liquid-like to solid-like state. [28] Also, the suspension returned to their original state when magnetic field is turned off, meaning the transition is reversible process. The reversibility of the structure formation will be discussed further in the reversibility tests part.

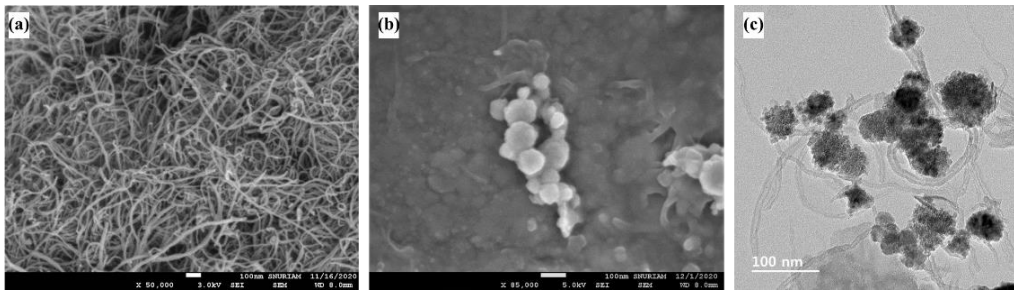


Figure 5. 2. SEM images of (a) functionalized CNTs (b) CNT-Co_{0.4}Fe_{0.4}Ni_{0.2} (c) TEM image of CNT-Co_{0.4}Fe_{0.4}Ni_{0.2}

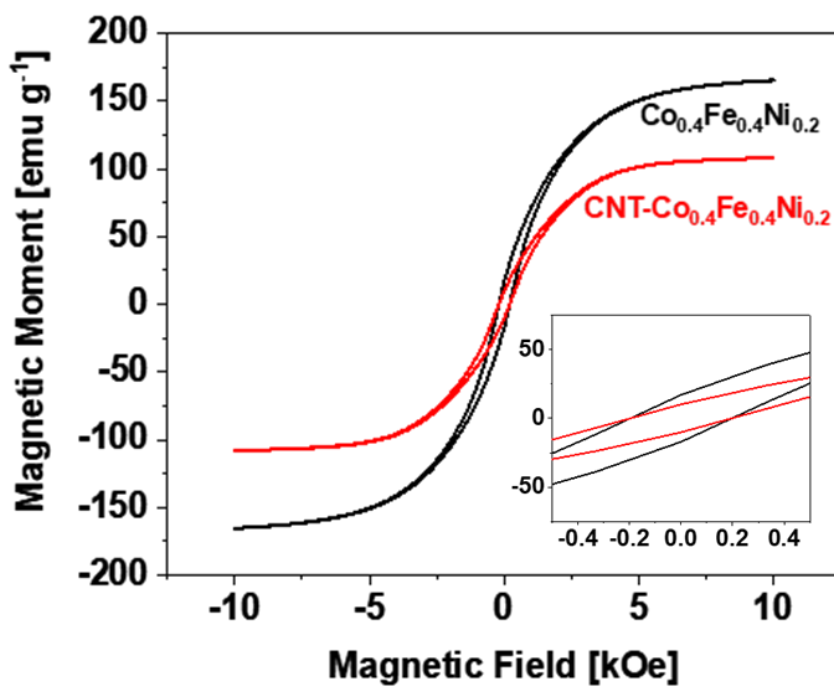


Figure 5. 3. VSM curves for $\text{Co}_{0.4}\text{Fe}_{0.4}\text{Ni}_{0.2}$ and $\text{CNT-Co}_{0.4}\text{Fe}_{0.4}\text{Ni}_{0.2}$

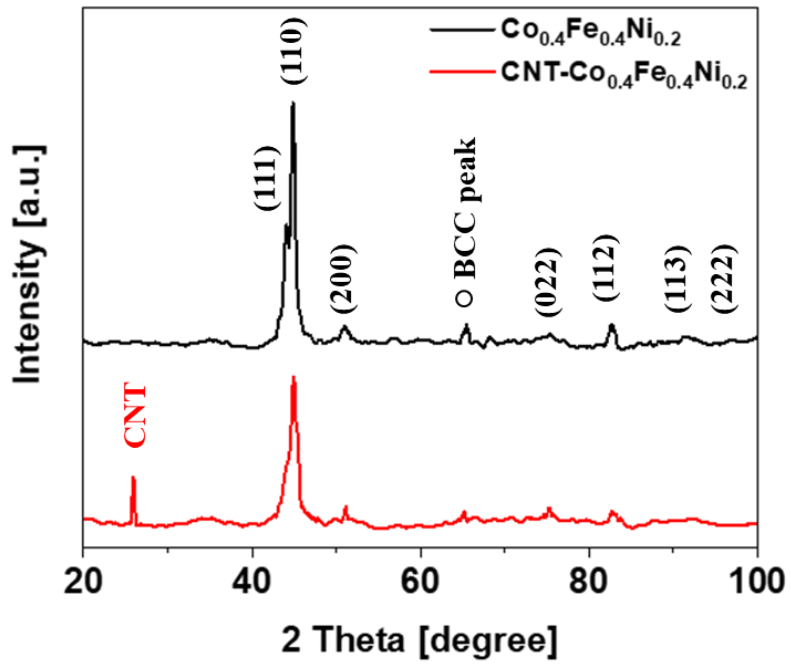


Figure 5. 4. XRD patterns for $\text{Co}_{0.4}\text{Fe}_{0.4}\text{Ni}_{0.2}$ and CNT- $\text{Co}_{0.4}\text{Fe}_{0.4}\text{Ni}_{0.2}$

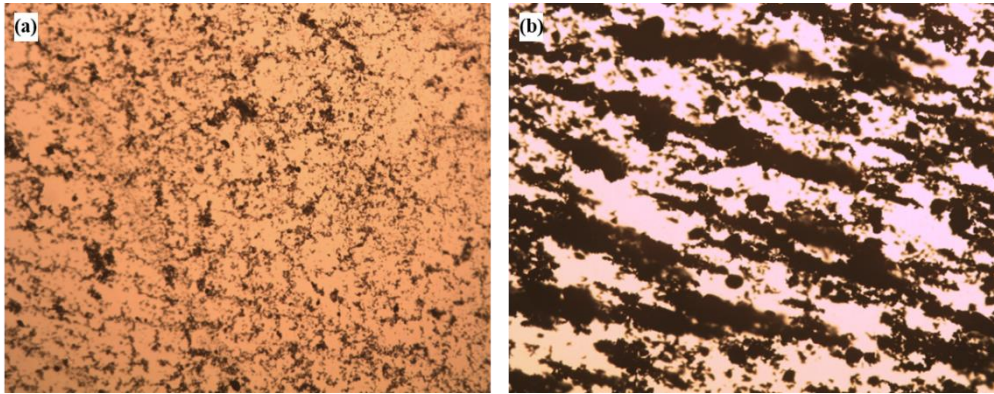


Figure 5. 5. Optical microscopic images of microstructural change for CNT- $\text{Co}_{0.4}\text{Fe}_{0.4}\text{Ni}_{0.2}$ suspension. (a) before and (b) after application of the external magnetic field of 86 kA/m.

5. 3. 2. Magnetorheological properties

MR properties of $\text{Co}_{0.4}\text{Fe}_{0.4}\text{Ni}_{0.2}$ and $\text{CNT-Co}_{0.4}\text{Fe}_{0.4}\text{Ni}_{0.2}$ were measured with rotational rheometer under magnetic field. Under strong magnetic field where Brownian motion of magnetic particles can be neglected, the behavior of MR suspensions is determined by magneto polarization force between the particles and the hydrodynamic force induced by external shear. [1,39] When polarization force is dominant, chain-like structures remain undisturbed, and MR suspensions show solid-like properties. Whereas, when hydrodynamic force is dominant MR suspensions show liquid-like properties due to destruction of the structures. [1,28] Figure is the illustration of change in modulus with shear strain (amplitude sweep) and angular frequency (frequency sweep). Figure shows the results of amplitude sweep test at two magnetic field strength (86 and 343 kA/m) with the strain range from 0.001 to 100 %. For all tests, linear viscoelastic (LVE) region where storage modulus is independent was observed at low strain stage (until about 0.03 %). In LVE region, chain-like structures endure the hydrodynamic stress and retain their structure, showing solid-like properties. [1] After LVE region, the moduli of each suspension decreases with strain due to destruction of the chain-like structures. [1,28] As observed, storage moduli in LVE region was higher for $\text{Co}_{0.4}\text{Fe}_{0.4}\text{Ni}_{0.2}$ with higher M_s and increased with magnetic field strength due to reinforced magnetic dipole-dipole strength. Figure 5.6 shows the frequency sweep results in the range of 1 to 100 rad/s with 0.01 % of shear strain. All results show that storage modulus is higher than loss modulus by more than an order, indicating the dominance of solid-like properties. [40] Storage modulus was higher for

Co_{0.4}Fe_{0.4}Ni_{0.2} suspension and increased with field strength, similar to the results of amplitude sweep LVE region. However, unlike the amplitude sweep results, storage modulus did not change significantly in whole frequency range, showing chain-like structures were not disturbed under the condition of frequency sweep test. [28, 29, 35]

Figure 5.7 shows the shear stress and viscosity versus shear rate in range of 0.1 to 500 s⁻¹ under two different magnetic field strength. In figure 5.7 (a), shear stress at low shear rate range does not reveal significant change with polarization force dominant over hydrodynamic stress. [28,29] Sometimes, the decrease of stress followed by subsequent recovery with partial destruction and reformation of chain-like structures were observed, which is frequently examined for electrorheological fluids. [29] However, this was not observed for all tests in this work, presenting robustness of the chain-like structures. Like storage modulus in viscoelastic measurements, due to weakened interaction between particles, shear stress for CNT-Co_{0.4}Fe_{0.4}Ni_{0.2} suspension was the inferior of the two suspensions. With hydrodynamic increasing with shear rate, the chain-like structures were completely broken apart, and shear stress increases with shear rate at high shear rate range. [28, 29, 30] This was clearly observed for CNT-Co_{0.4}Fe_{0.4}Ni_{0.2} suspension with magnetic field strength of 86 kA/m, because the strength of chain-like structures is weakest for this case. The viscosity for all tests (Figure 5.7 (b)) showed shear-thinning behavior and linearly decreasing tendency with shear rate. Because viscosity is the ratio between shear stress and shear rate, viscosity of each suspension has the same order with its shear stress. And like storage modulus and shear stress, the viscosity increased with magnetic field, and

higher for $\text{Co}_{0.4}\text{Fe}_{0.4}\text{Ni}_{0.2}$.

For direct comparison of MR performance, yield stress of the suspensions was predicted and measured with theoretical and experimental methods. For theoretical estimation of yield stress, dynamic yield stress, where complete destruction of chain-like structures occurs and static yield stress, where flow of MR suspensions is induced was calculated with Bingham fluid model and Seo-Seo model, respectively. [39, 41, 42] Bingham fluid model is expressed as follows

$$\tau = \tau_{dy} + \eta_{pl}\dot{\gamma} \quad (1)$$

where τ is the shear stress in shear stress vs shear rate curve, τ_{dy} is the dynamic yield stress, η_{pl} is the plastic viscosity, and $\dot{\gamma}$ is the shear rate. [41] In this model, with extrapolation of shear stress to zero shear rate, dynamic yield stress of MR suspensions can be obtained. However, this model cannot predict yield stress properly when the structural deformation of partial destruction and reformation occurs at low shear rate range. [42] To cover the structural change, static yield stress where suspension starts to flow should be considered, and this was predicted with Seo-Seo model [39, 44, 45]

$$\tau = \tau_{sy} \left(1 - \frac{(1-\exp(-a\dot{\gamma}))}{(1+(a\dot{\gamma})^\alpha)} \right) + \eta_{pl}\dot{\gamma} \quad (2)$$

where τ_{sy} is the static yield stress at low shear rate, η_{pl} is the plastic viscosity, a is the time constant (the reciprocal of the critical shear rate for an aligned mesostructure deformation), and α is the power-law index which determines the degree of shear thinning.

[39] When $a = 0$, this equation became same with Bingham fluid model, which means this model also include the dynamic yield stress for this case. [43, 44] The experimental measurement of static yield stress was conducted with controlled shear stress (CSS) mode, where viscosity of MR suspension is measured with changing shear stress. [28] Static yield stress of each suspension was determined at shear stress value where sudden drop of viscosity occurs. [29,30] The yield stress measurement results at two different field strengths are illustrated in Figure 5.8. For all samples, the viscosities were decreased tremendously by more than 3 orders at their static yield stress.

The three yield stress values for $\text{Co}_{0.4}\text{Fe}_{0.4}\text{Ni}_{0.2}$, CNT- $\text{Co}_{0.4}\text{Fe}_{0.4}\text{Ni}_{0.2}$, and other Fe_3O_4 composites-based suspensions were compared in table 5.1. For all sample, theoretical and measured static yield stress showed similar value to each other. This means that chain-like structures for the MR suspensions are strong enough and flow is induced when chain-like structures are completely destroyed. When yield stress values of CNT- $\text{Co}_{0.4}\text{Fe}_{0.4}\text{Ni}_{0.2}$ and Fe_3O_4 composites-based suspensions in our previous works were compared, CNT- $\text{Co}_{0.4}\text{Fe}_{0.4}\text{Ni}_{0.2}$ showed much better performance. Under magnetic field strength of 343 kA/m, measured static yield stress of CNT- $\text{Co}_{0.4}\text{Fe}_{0.4}\text{Ni}_{0.2}$ suspension is 1901 Pa, which is 1028 % and 323 % of yield stress of h-PDVB@ Fe_3O_4 and HS- Fe_3O_4 suspension respectively [30,35]. Especially when the static yield stress of CNT- $\text{Co}_{0.4}\text{Fe}_{0.4}\text{Ni}_{0.2}$ suspension was compared to that of CNT- Fe_3O_4 suspension in previous work, it was 1372 % at 343 kA/m. [34] As mentioned with VSM results, CNT- $\text{Co}_{0.4}\text{Fe}_{0.4}\text{Ni}_{0.2}$ have M_s much higher than the Fe_3O_4 composites in previous works (41, 70 and 42 emu/g for h-

PDVB@Fe₃O₄, HS-Fe₃O₄ and CNT-Fe₃O₄ respectively) due to very high M_s value of Co_{0.4}Fe_{0.4}Ni_{0.2}. Also, the density of CNT-Co_{0.4}Fe_{0.4}Ni_{0.2} is higher than the Fe₃O₄ composites, thus the weight proportion of magnetic particles in MR fluids is higher for CNT-Co_{0.4}Fe_{0.4}Ni_{0.2} under same volume concentration. Such high magnetization and contents of CNT-Co_{0.4}Fe_{0.4}Ni_{0.2} in suspension directly result in much higher yield stress of CNT-Co_{0.4}Fe_{0.4}Ni_{0.2} suspension compared to the Fe₃O₄ composite-based suspensions.

To check the reversibility of formation of chain-like structures and MR properties under magnetic field, change in shear stress of Co_{0.4}Fe_{0.4}Ni_{0.2} and CNT-Co_{0.4}Fe_{0.4}Ni_{0.2} suspension were examined with switching magnetic field. Figure 5.9 is the results for the reversibility tests at two different magnetic field strengths with shear rate of 1 s⁻¹. For both suspensions, shear stress increased abruptly when magnetic field is turned on, then decreased when the field is removed. This behavior repeated for three cycles of switching field, proving the reversibility of response to external magnetic field. When maximum shear stress value is compared to static yield stress values measured with CSS mode, they are very close to each other, showing the validity of these tests. Also, there was no lag for response to magnetic field when compared with the reversibility tests for HS-Fe₃O₄ in previous chapter, meaning that aspect ratio of composite particles does not have effect on responsiveness of MR suspension.

As stated earlier, MR properties under sufficiently strong magnetic field strength are governed by magneto polarization force and hydrodynamic force, and this dependence is represented by the ratio between hydrodynamic drag and the magneto static forces. This

ratio is called Mason number, $M_n = 8\eta_0\dot{\gamma}/\mu_0\mu_c\beta^2 M^2$, where η_0 is the medium viscosity, $\dot{\gamma}$ is the shear rate, β is the contrast factor ($= (\mu_p - \mu_c)/(\mu_p + 2\mu_c)$), μ_p is the particle relative permeability, μ_c is the relative permeability of the liquid medium phase, and $\mu_0 = 4\pi \times 10^{-7} \text{ N}/\text{A}^2$ is the vacuum permeability, and M is the magnetic field strength. [46, 47] Here, $\eta_0\dot{\gamma}$ term in numerator and M^2 term in denominator correspond to hydrodynamic force under continuous shear and magnetic polarization force, respectively. [47] Thus, Mason number is equivalent to a single independent variable $\dot{\gamma}/M^2$, and behavior of MR fluids can be evaluated with $\dot{\gamma}/M^2$. [47] When volume fraction of suspensions is fixed, the behavior of different MR fluids can be compared with a master curve for the specific viscosity (apparent viscosity/medium viscosity) and volume fraction correction versus $\dot{\gamma}/M^2$. Corrected viscosities for $\text{Co}_{0.4}\text{Fe}_{0.4}\text{Ni}_{0.2}$ and $\text{CNT-Co}_{0.4}\text{Fe}_{0.4}\text{Ni}_{0.2}$ against $\dot{\gamma}/M^2$ at two different magnetic field strength were shown in Figure 5.10. [48,49] As clearly seen, all four curves were overlapped well with each other regardless of $\text{Co}_{0.4}\text{Fe}_{0.4}\text{Ni}_{0.2}$ content and magnetic field strength, showing these two factors does not affect MR behavior and scaling law. In addition, when these curves were compared with those of Fe_3O_4 composite based-MR suspensions in our previous works, they showed excellent overlap. [30,35] This proves that the species and shapes of magnetic particles do not alter the scaling law for MR suspensions.

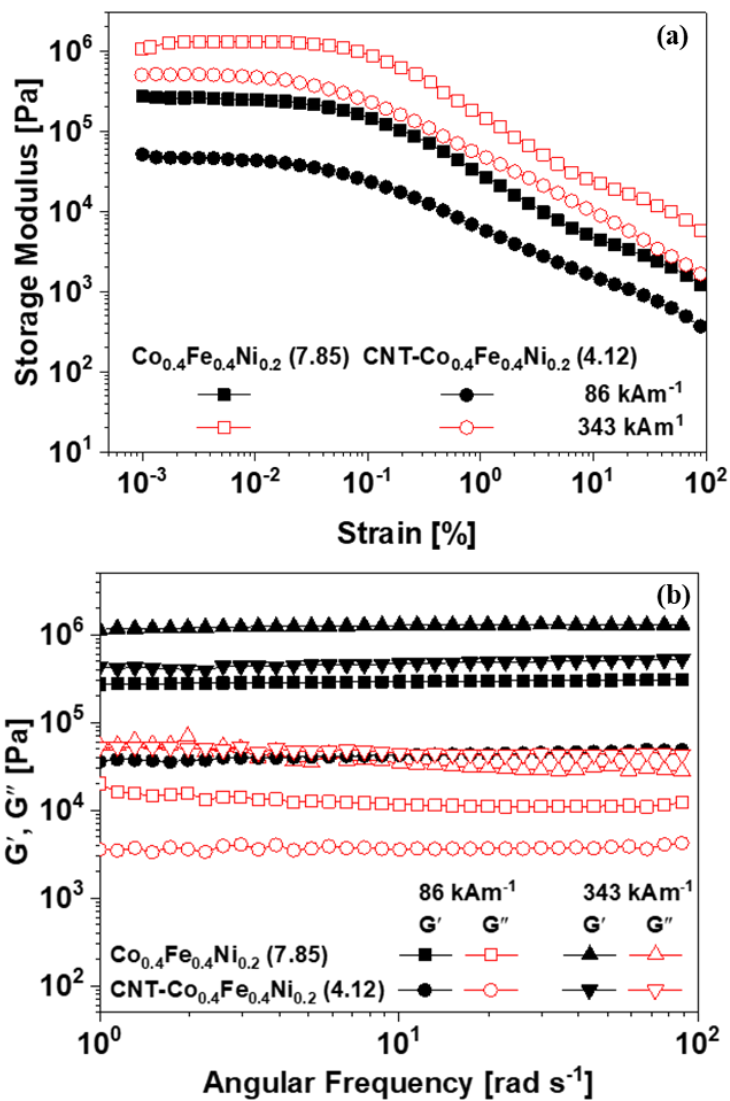


Figure 5. 6. (a) amplitude sweep (strain dependence) of storage modulus, G' and (b) Frequency sweep (frequency dependence) of storage modulus (G') and loss modulus (G'') for $\text{Co}_{0.4}\text{Fe}_{0.4}\text{Ni}_{0.2}$ and CNT- $\text{Co}_{0.4}\text{Fe}_{0.4}\text{Ni}_{0.2}$ suspension at 86 kA/m and 343 kA/m.

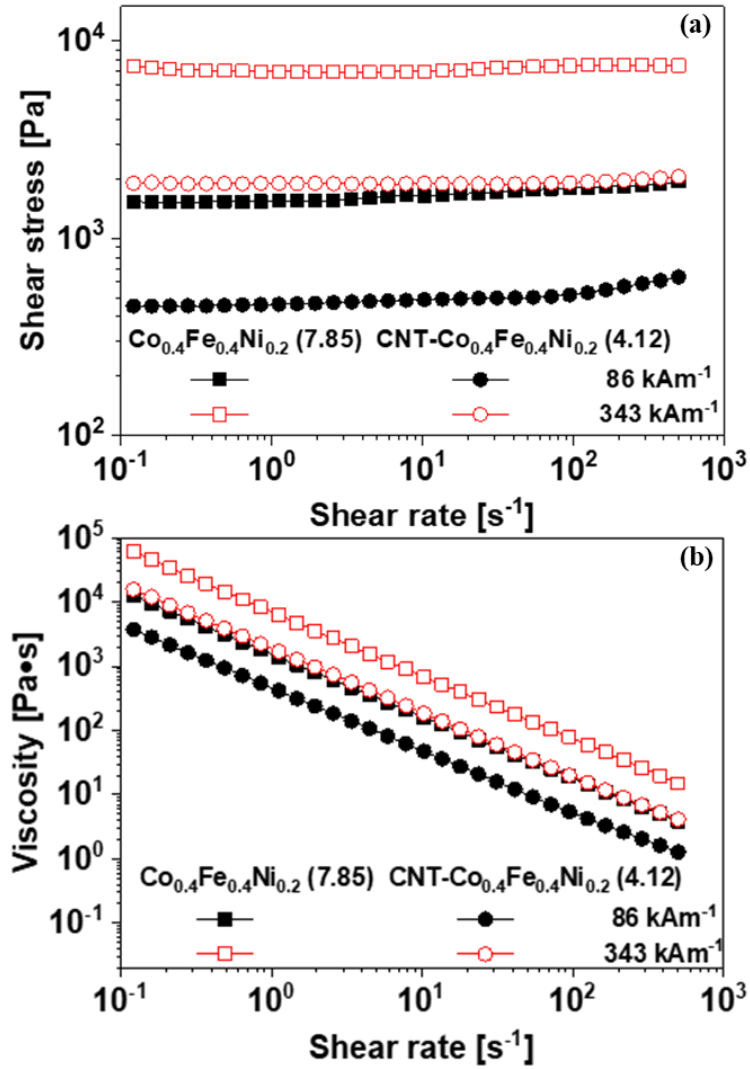


Figure 5. 7. (a) shear stress and (b) viscosity curves as a function of shear rate for MR fluids of $Co_{0.4}Fe_{0.4}Ni_{0.2}$ and $CNT-Co_{0.4}Fe_{0.4}Ni_{0.2}$

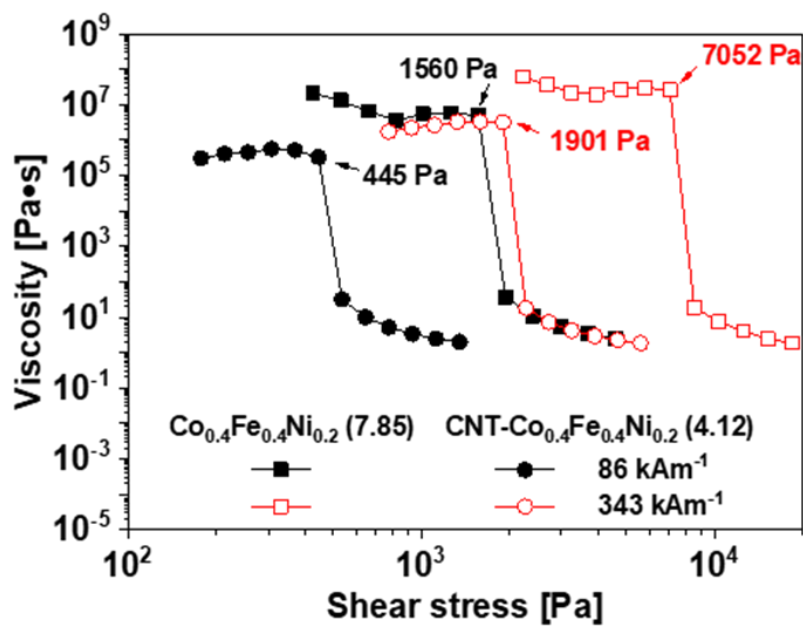


Figure 5. 8. Shear viscosity as a function of shear stress for $\text{Co}_{0.4}\text{Fe}_{0.4}\text{Ni}_{0.2}$ and $\text{CNT-Co}_{0.4}\text{Fe}_{0.4}\text{Ni}_{0.2}$ MR fluids at 86 kA/m and 343 kA/m .

Table 5.1. Static yield stress and dynamic yield stress of $\text{Co}_{0.4}\text{Fe}_{0.4}\text{Ni}_{0.2}$, CNT- $\text{Co}_{0.4}\text{Fe}_{0.4}\text{Ni}_{0.2}$, and Fe_3O_4 composites-based MR suspensions

	Yield stress (Pa)					
	M = 86 (kA/m)			M = 343 (kA/m)		
	Static exp (τ_{sy})	Dynamic (τ_{dy})	Static SS (τ_{sy})	Static exp (τ_{sy})	Dynamic (τ_{dy})	Static SS (τ_{sy})
$\text{Co}_{0.4}\text{Fe}_{0.4}\text{Ni}_{0.2}$ (7.85 g/cm ³)	1560	1601	1561	7052	7120	7150
CNT- $\text{Co}_{0.4}\text{Fe}_{0.4}\text{Ni}_{0.2}$ (4.12 g/cm ³)	445	472	485	1901	1887	1889
h-PDVB@ Fe_3O_4 (1.83 g/cm ³) [31]	100	105	105	185	190	180
HS- Fe_3O_4 (3.32 g/cm ³) [36]	337	338	338	588	584	585
CNT/ Fe_3O_4 (2.94 g/cm ³) [34]	28.8	24.1	33	138.5	139.4	145

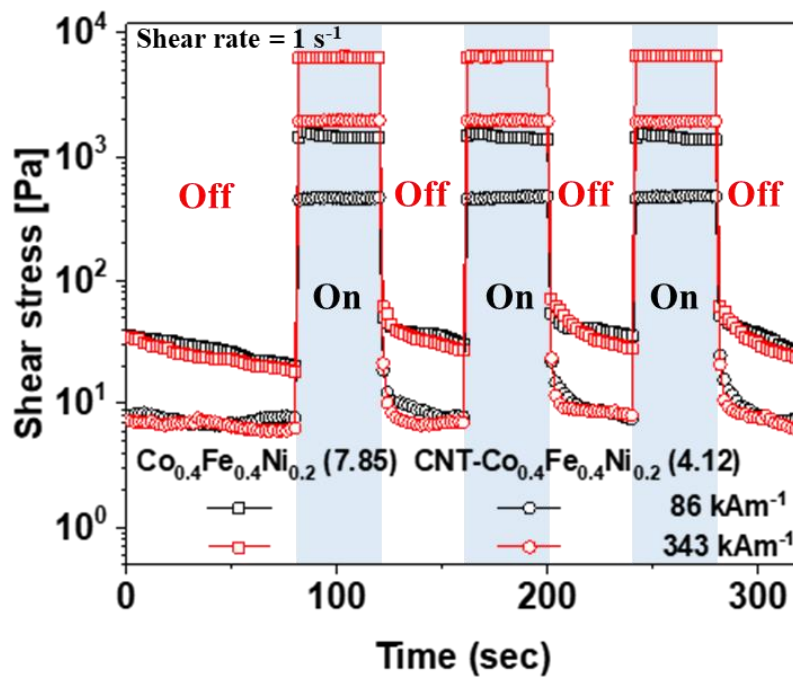


Figure 5. 9. Transient responses (reversibility) of the $\text{Co}_{0.4}\text{Fe}_{0.4}\text{Ni}_{0.2}$ and CNT- $\text{Co}_{0.4}\text{Fe}_{0.4}\text{Ni}_{0.2}$ MR fluids at shear rate of 1 s^{-1} .

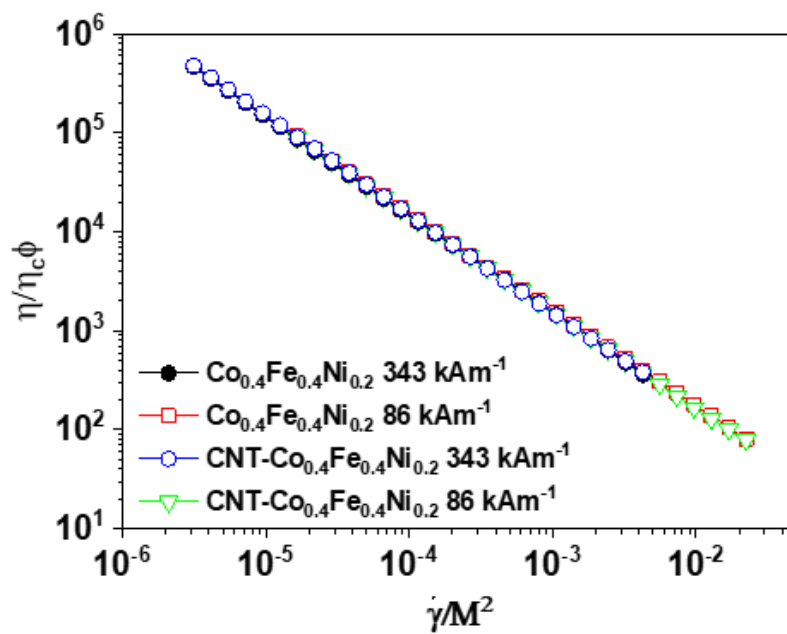


Figure 5. 10. Dimensionless apparent viscosity of the MR fluids as a function of $\dot{\gamma}/M^2$ at various magnetic field strengths.

5. 3. 3. Long-Term Stability of Suspensions

The long-term stability of $\text{Co}_{0.4}\text{Fe}_{0.4}\text{Ni}_{0.2}$ and $\text{CNT-Co}_{0.4}\text{Fe}_{0.4}\text{Ni}_{0.2}$ was observed with change in light transmission with time using Turbiscan (Figure 5.11). For both samples, light transmission increased quickly at the early stage of the tests, and then became almost unchanged until 24 h. The light transmission after 24 h $\text{Co}_{0.4}\text{Fe}_{0.4}\text{Ni}_{0.2}$ fluid was 81 %, while that of $\text{CNT-Co}_{0.4}\text{Fe}_{0.4}\text{Ni}_{0.2}$ was only 22 %. Considering that the density of $\text{CNT-Co}_{0.4}\text{Fe}_{0.4}\text{Ni}_{0.2}$ is comparable to that of bare Fe_3O_4 particles, this transmission value is extremely low.

For hard spheres, the sedimentation velocity of the particles is expressed.

$$V(\phi, d) = \frac{|\rho_p - \rho_c| \times g \times d^2}{18 \times \nu \times \rho_c} \cdot \frac{[1 - \phi]}{\left[1 + \frac{4.6\phi}{(1 - \phi)^3}\right]}$$

where V is the particle migration velocity (m s^{-1}), ρ_p presents the particle density, ρ_c is the continuous phase density (kg m^{-3}), ν denotes the kinematic viscosity of continuous phase, g is gravity constant (9.81 m s^{-2}), d means the particle diameter, and ϕ represents the volume fraction of the particles. [50] In this equation, the effect of particle diameter can be offset by surface friction for spherical particles with rough surface. Thus, the sedimentation velocity is mainly determined with density mismatch between particles and carrier medium. However, this equation is only applied to spherical particles. Unlike Fe_3O_4 -based composite particles with spherical shape in our previous works, or bare $\text{Co}_{0.4}\text{Fe}_{0.4}\text{Ni}_{0.2}$ particles, another factor other than density mismatch should be considered: self-supporting effect from CNTs. When CNTs are

dispersed in fluid with enough volume concentration, they can form percolation network structures due to their high aspect ratio. [31, 32] These structures can support the composites and prevent them from sedimentation to the bottom of suspensions. [33] This was also observed for MR fluids containing CNT-Fe₃O₄ composite as magnetic particles, resulting in excellent long-term stability with light transmission of 4 % after 24 h. [34] Although light transmission for CNT-Co_{0.4}Fe_{0.4}Ni_{0.2} suspension was higher than CNT-Fe₃O₄ due to higher density of CNT-Co_{0.4}Fe_{0.4}Ni_{0.2} (4.12 g/cm³) than CNT-Fe₃O₄ (2.94 g/cm³), it is much better than HS-Fe₃O₄ (45 % of light transmission) with spherical shape and lower density (3.32 g/cm³). In addition, the MR performance of CNT-Co_{0.4}Fe_{0.4}Ni_{0.2} in terms of yield stress was much better than the Fe₃O₄ composites. This shows the potential for production of MR fluids possessing high MR performance and long-term stability at the same time.

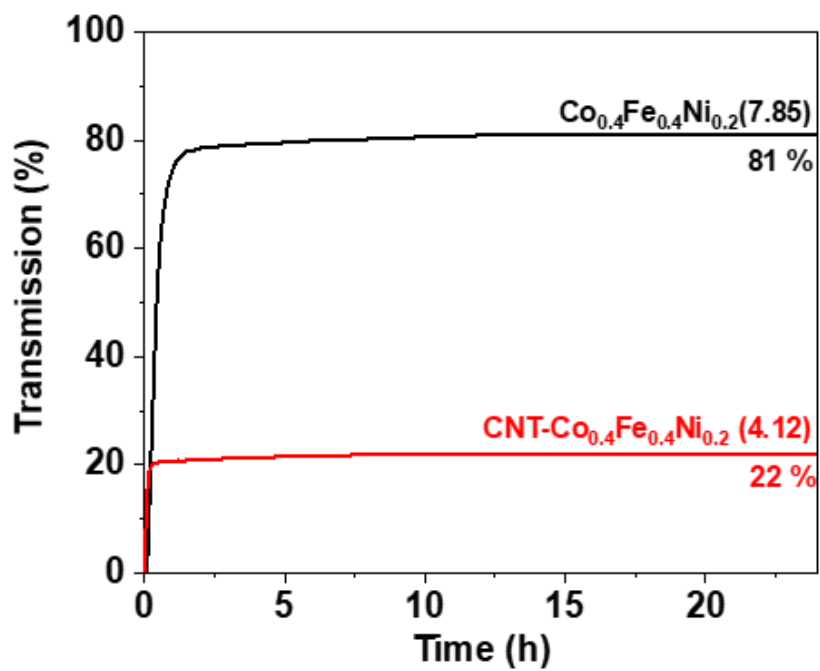


Figure 5. 11. Transmission (%) curve as a function of time (h) for $\text{Co}_{0.4}\text{Fe}_{0.4}\text{Ni}_{0.2}$ and $\text{CNT-Co}_{0.4}\text{Fe}_{0.4}\text{Ni}_{0.2}$ particles for 24h.

5. 4. Conclusions

In this study, for the objective of achieving high-performance and excellent long-term stability of MR fluids, preparation and use of CNT-Co_{0.4}Fe_{0.4}Ni_{0.2} composite were suggested. By synthesizing Co_{0.4}Fe_{0.4}Ni_{0.2} nanoparticles on the surface of functionalized CNTs, CNT-Co_{0.4}Fe_{0.4}Ni_{0.2} composite tubes could be obtained. With replacement of magnetic materials from Fe₃O₄ to Co_{0.4}Fe_{0.4}Ni_{0.2}, CNT-Co_{0.4}Fe_{0.4}Ni_{0.2} have very high magnetization of 108 emu/g, which is higher by more than two times of CNT-Fe₃O₄. This directly resulted in excellent MR performance of CNT-Co_{0.4}Fe_{0.4}Ni_{0.2} suspension, with yield stress of 445 Pa and 1901 Pa at the field strength of 86 and 343 kA/m. The yield stress at 343 kA/m is 1358 % greater than previous results of CNT-Fe₃O₄-based MR systems. In addition, the MR behavior and reversibility of CNT-Co_{0.4}Fe_{0.4}Ni_{0.2} was conserved when compared with Fe₃O₄-based suspensions. Simultaneously, the high aspect ratio of CNTs make CNT-Co_{0.4}Fe_{0.4}Ni_{0.2} to form a percolated network structure, supporting themselves in suspension. This supporting effect enables CNT-Co_{0.4}Fe_{0.4}Ni_{0.2} to have excellent long-term stability with 22 % light transmission after 24h despite of its much higher density compared to other Fe₃O₄ composite-based suspensions. These results suggests that problem of strong trade-off between MR performance and long-term stability can be solved through choice of appropriate magnetic materials and change of particle morphology, expanding application MR fluids in microfluidic area.

References

- (1) Seo, Y. P.; Han, S.; Choi, J.; Takahara, A.; Choi, H. J.; Seo, Y., Searching for a stable high-performance magnetorheological suspension. *Adv. Mater.* 2018, 30 (42), 1704769.
- (2) Lee, S.; Noh, J.; Hong, S.; Kim, Y. K.; Jang, J., Dual stimuli-responsive smart fluid of graphene oxide-coated iron oxide/silica core/shell nanoparticles. *Chem. Mater.* 2016, 28 (8), 2624-2633.
- (3) Kim, Y. J.; Liu, Y. D.; Seo, Y.; Choi, H. J., Pickering-emulsion-polymerized polystyrene/Fe₂O₃ composite particles and their magnetoresponse characteristics. *Langmuir* 2013, 29 (16), 4959-4965
- (4) Ahamed R.; Choi S.B.; Ferdaus M., A state of art on magneto-rheological materials and their potential applications, *J. Intellig. Mat. Syst. Struct.* 2018, 29(10) 2051-2095
- (5) Ghaffari, A.; Hashemabadi, S. H.; Ashtiani, M., A review on the simulation and modeling of magnetorheological fluids. *J. Intell. Mater. Syst. Struct.* 2015, 26 (8), 881-904.
- (6) Liu, Y.; Lee, J.; Choi, S.; Choi, H., Silica-coated carbonyl iron microsphere based magnetorheological fluid and its damping force characteristics. *Smart Mater. Struct.* 2013, 22 (6), 065022..
- (7) Tian, Y.; Jiang, J.; Meng, Y.; Wen, S., A shear thickening phenomenon in magnetic

field controlled-dipolar suspensions. *Appl. Phys. Lett.* 2010, 97 (15), 151904.

(8) Santiago-Quiñonez, D. I.; Rinaldi, C., Enhanced rheological properties of dilute suspensions of magnetic nanoparticles in a concentrated amphiphilic surfactant solution. *Soft Matter* 2012, 8 (19), 5327-5333.

(9) López-López, M. T.; Gómez-Ramírez, A.; Rodríguez-Arco, L.; Durán, J. D.; Iskakova, L.; Zubarev, A., Colloids on the frontier of ferrofluids. Rheological properties. *Langmuir* 2012, 28 (15), 6232-6245.

(10) Cheng, H.; Zuo, L.; Song, J.; Zhang, Q.; Wereley, N., Magnetorheology and sedimentation behavior of an aqueous suspension of surface modified carbonyl iron particles. *J. Appl. Phys.* **2010**, 107 (9), 09B507.

(11) Park, B. J.; Fang, F. F.; Choi, H. J., Magnetorheology: materials and application. *Soft Matter* 2010, 6 (21), 5246-5253.

(12) Bitaraf, M.; Ozbulut, O. E.; Hurlebaus, S.; Barroso, L., Application of semi-active control strategies for seismic protection of buildings with MR dampers. *Eng. Struct.* 2010, 32 (10), 3040-3047.

(13) Chen, Z.; Wang, X.; Ko, J.; Ni, Y.; Spencer Jr, B. F.; Yang, G. In MR damping system on Dongting Lake cable-stayed bridge, *Smart Structures and Materials* 2003: Smart Systems and Nondestructive Evaluation for Civil Infrastructures, International Society for Optics and Photonics: 2003; pp 229-235.

- (14) Oliveira, F.; de Moraes, P. G.; Suleman, A., Semi-active control of base-isolated structures. *Procedia Eng.* 2015, 114, 401-409.
- (15) Ashtiani, M.; Hashemabadi, S.; Ghaffari, A., A review on the magnetorheological fluid preparation and stabilization. *J. Magn. Magn. Mater.* 2015, 374, 716-730.
- (16) Choi, H. J.; Zhang, W. L.; Kim, S.; Seo, Y., Core-shell structured electro-and magneto-responsive materials: Fabrication and characteristics. *Materials* 2014, 7 (11), 7460-7471..
- (17) Seo, Y. P.; Choi, H. J.; Seo, Y., Analysis of the flow behavior of electrorheological fluids with the aligned structure reformation, *Polymer*, 2011, 52 (25), 5695-5698
- (18) Cvek, M.; Mrlik, M.; Ilcikova, M.; Mosnacek, J.; Munster, L.; PavlinekV.; Pavlinek, V.; Synthesis of Silicone Elastomers Containing Silyl-Based Polymer- Grafted Carbonyl Iron Particles: An Efficient Way To Improve Magnetorheological, Damping, and Sensing Performances. *Macromolecules* 2017, 50 (5), 2189-2200.
- (19) Fang, F. F.; Choi, H. J.; Seo, Y., Sequential coating of magnetic carbonyliron particles with polystyrene and multiwalled carbon nanotubes and its effect on their magnetorheology. *ACS Appl. Mater. Interfaces.* 2010, 2 (1), 54-60.
- (20) Cvek, M.; Mrlik, M.; Ilcikova, M.; Plachy, T.; Sedlacik, M.; Mosnacek, J.; Pavlinek, V., A facile controllable coating of carbonyl iron particles with poly(glycidyl methacrylate): a tool for adjusting MR response and stability properties. *J. Mater. Chem.*

C 2015, 3 (18), 4646-4656.

(21) Pu, H. T.; Jiang, F. J.; Yang, Z.-l., Preparation and properties of soft magnetic particles based on Fe_3O_4 and hollow polystyrene microsphere composite. *Materials Chemistry and Physics* 2006, 100 (1), 10-14.

(22) Du, Z.; Qiu, Y.; Niu, T.; Wang, W.; Ye, X.; Wang, J.; Zhang, W. L.; Choi, H. J.; Zeng, H., Bio-inspired passion fruit-like $\text{Fe}_3\text{O}_4@C$ nanospheres enabling high-stability magnetorheological performances. *Langmuir* 2020, 36 (26), 7706-7714.

(23) Fang, F. F.; Kim, J. H.; Choi, H. J., Synthesis of core-shell structured PS/ Fe_3O_4 microbeads and their magnetorheology. *Polymer* 2009, 50 (10), 2290-2293.

(24) Kim, J. N.; Dong, Y. Z.; Choi, H. J., Pickering Emulsion Polymerized Polyaniline/Zinc-ferrite Composite Particles and Their Dual Electrorheological and Magnetorheological Responses. *ACS omega* 2020, 5 (13), 7675-7682.

(25) Yoon, C.-M.; Jang, Y.; Lee, S.; Jang, J., Dual electric and magnetic responsivity of multilayered magnetite-embedded core/shell silica/titania nanoparticles with outermost silica shell. *J. Mater. Chem. C* 2018, 6 (38), 10241-10249.

(26) Lee, J. H.; Lu, Q.; Lee, J. Y.; Choi, H. J., Polymer-Magnetic Composite Particles of Fe_3O_4 /Poly(o-anisidine) and Their Suspension Characteristics under Applied Magnetic Fields. *Polymers* 2019, 11 (2), 219.

(27) He, M.; Zeng, Y.; Zhou, F.; Kong, G.; Lu, Y.; Chen, W.; Ma, Y.; Yu,

R.; Wang, Z.; Li, Z., MnFe₂O₄ nanoparticles anchored on the surface of MgAl-layered double hydroxide nanoplates for stable magnetorheological fluids. *J. Mol. Liq.* 2020, 114098.

(28) Chuah, W. H.; Zhang, W. L.; Choi, H. J.; Seo, Y., Magnetorheology of core-shell structured carbonyl iron/polystyrene foam microparticles suspension with enhanced stability. *Macromolecules* 2015, 48 (19), 7311-7319.

(29) Han, S.; Choi, J.; Seo, Y. P.; Park, I. J.; Choi, H. J.; Seo, Y., High-performance magnetorheological suspensions of pickering-emulsion-polymerized polystyrene/Fe₃O₄ particles with enhanced stability. *Langmuir* 2018, 34 (8), 2807-2814.

(30) Choi, J.; Han, S.; Kim, H.; Sohn, E. H.; Choi, H. J.; Seo, Y., Suspensions of Hollow Polydivinylbenzene Nanoparticles Decorated with Fe₃O₄ Nanoparticles as Magnetorheological Fluids for Microfluidics Applications. *ACS Appl. Nano Mater.* 2019, 2 (11), 6939-6947.

(31) Wen, D.; Ding, Y., Effective thermal conductivity of aqueous suspensions of carbon nanotubes (carbon nanotube nanofluids). *J. Thermophys Heat Transfer* 2004, 18 (4), 481-485.

(32) Samouhos, S.; McKinley, G., Carbon nanotube-magnetite composites, with applications to developing unique magnetorheological fluids. *J. Fluids Eng.* 2007, 129 (4), 429-437.

(33) Pu, H.; Jiang, F., Towards high sedimentation stability: magnetorheological fluids

based on CNT/Fe₃O₄ nanocomposites. *Nanotechnology* 2005, 16 (9), 1486

(34) Kim, H.; Kim, S.; Seo, Y., High-Performance Magnetorheological Suspensions of Fe₃O₄-deposited Carbon Nanotubes with Enhanced Stability. *MRS Adv.* 2019, 4 (3-4), 217-224.

(35) Choi, J.; Han, S.; Kim, H.; Nam, K. T.; Seo, Y., Hierarchically Structured Fe₃O₄ Nanoparticles for High-Performance Magnetorheological Fluids with Long-Term Stability. *ACS Appl. Nano Mater.* 2020.

(36) LEE, J. Y.; Kwon, S. H.; Kim, H.; Choi, H. J., Magnetorheological characteristics of carbonyl iron microparticles with different shapes, *Korea Aust. Rheol. J.* 2019, 31 (1), 41-47

(37) Reddy, G. S.; Sahu, S. R.; Prakash, R.; Jagannatham, M., Synthesis of cobalt-rich alloys with high saturation magnetization: A novel synthetic approach by hydrazine reduction method. *Results Phys.* 2019, 12, 652-661.

(38) Murugesan, S., Myers, K.,; Subramanian. V. R., Amino-functionalized and acid treated multi-walled carbon nanotubes as supports for electrochemical oxidation of formic acid. *Appl. Catal. B* 2011, 103 (3-4), 266-274.

(39) Seo, Y. P.; Seo, Y., Modeling and analysis of electrorheological suspensions in shear flow. *Langmuir* 2012, 28 (6), 3077-3084.

(40) Upadhyay, R.; Laherisheth, Z.; Shah, K., Rheological properties of soft

magnetic flake shaped iron particle based magnetorheological fluid in dynamic mode. *Smart Mater. Struct.* 2013, 23 (1), 015002

(41) Farjoud, A.; Vahdati, N.; Fah, Y. F., Mathematical model of drum-type MR brakes using Herschel-Bulkley shear model. *J. Intell. Mater. Syst. Struct.* 2008, 19 (5), 565-572.

(42) Seo, Y. P.; Choi, H. J.; Lee, J. R.; Seo, Y., Modeling and analysis of an electrorheological flow behavior containing semiconducting graphene oxide/polyaniline composite particles. *Colloids Surf. A Physicochem. Eng. Asp.* 2014, 457, 363-367.

(43) Seo, Y. P.; Choi, H. J.; Seo, Y., A simplified model for analyzing the flow behavior of electrorheological fluids containing silica nanoparticle-decorated polyaniline nanofibers. *Soft Matter* 2012, 8 (17), 4659-4663

(44) Seo, Y. P.; Han, S.; Kim, J.; Choi, H. J.; Seo, Y., Analysis of the flow behavior of electrorheological fluids containing polypyrrole nanoparticles or polypyrrole/silica nanocomposite particles. *Rheol. Acta* 2020, 59 (6), 415-423.

(45) Seo, Y. P.; Kwak, S.; Choi, H. J.; Seo, Y., Static yield stress of a magnetorheological fluid containing Pickering emulsion polymerized Fe₂O₃/polystyrene composite particles. *J. Colloid Interface Sci.* 2016, 463, 272-278.

(46) Ruiz-López, J. A.; Fernández-Toledano, J. C.; Hidalgo-Alvarez, R.; de Vicente, J., Testing the mean magnetization approximation, dimensionless and scaling numbers in magnetorheology. *Soft Matter* 2016, 12 (5), 1468-1476.

- (47) De Vicente, J.; Klingenberg, D. J.; Hidalgo-Alvarez, R., Magnetorheological fluids: a review. *Soft matter* 2011, 7 (8), 3701-3710.
- (48) Shah, K.; Seong, M.-S.; Upadhyay, R.; Choi, S.-B., A low sedimentation magnetorheological fluid based on plate-like iron particles, and verification using a damper test. *Smart Mater. Struct.* 2013, 23 (2), 027001.
- (49) Becnel, A. C.; Sherman, S.; Hu, W.; Wereley, N. M., Nondimensional scaling of magnetorheological rotary shear mode devices using the Mason number. *J. Magn. Magn. Mater.* 2015, 380, 90-97.
- (50) Mills, P.; Snabre, P., Settling of a suspension of hard spheres. *EPL* 1994, 25 (9), 651-656.

Chapter 6. Sendust-CoFeNi Magnetic-Magnetic Composites- Based Magnetorheological Fluids for Simultaneous Improvement of Performance and Long-Term Stability

6. 1. Introduction

MR fluids, suspensions of magnetic particles in magnetically-insulating carrier medium, have unique response to external magnetic field. [1-4] With application of magnetic field, magnetic particles aggregated and aligned along field direction due to magnetostatic interaction between the particles, and viscosity of MR fluids increase by several orders in milliseconds. [1,5] The reverse change in rheological properties is observed when magnetic field is turned off, and this characteristic enables the rheological properties of MR fluids to be easily controlled with magnetic field strength. [4] With this modifiability, MR fluids have potential to be used for haptic devices, active suspension systems where active control of fluids' viscosity is needed and damper systems in automobile, buildings and bridges where dissipation external impact in to heat is needed. [6-9]

Despite of potential for used of MR fluids in various area, it is greatly hindered by poor long-term stability of MR fluids. This problem is mostly caused by large difference in density between heavy magnetic particles and light carrier medium, resulting in fast

sedimentation of magnetic particles and making reuse of MR fluids almost impossible. [9,10] To solve this problem, many reaches have been focused on fabrication of magnetic composite materials thorough combination of magnetic materials with materials with low density such as polymers, silica, carbon materials and so on. [11-19] However, when long-term stability of MR fluids is improved, the MR performance is declined due to deterioration of magnetic properties with the use of non-magnetic materials. In chapter 4, hierarchically structured Fe_3O_4 was fabricated and with exclusion of non-magnetic materials and improvement in MR performance compared to h-PDVB@ Fe_3O_4 in chapter 3 was observed. However, due to spherical shape and low magnetization value of Fe_3O_4 , there was limit in simultaneous enhancement of performance and long-term stability.

In chapter 5, CNT- $\text{Co}_{0.4}\text{Fe}_{0.4}\text{Ni}_{0.2}$ composites were fabricated by synthesizing $\text{Co}_{0.4}\text{Fe}_{0.4}\text{Ni}_{0.2}$ on the surface of functionalized CNTs. The saturation magnetization of $\text{Co}_{0.4}\text{Fe}_{0.4}\text{Ni}_{0.2}$ (~165 emu/g) much higher than Fe_3O_4 enabled CNT- $\text{Co}_{0.4}\text{Fe}_{0.4}\text{Ni}_{0.2}$ suspension to have very high yield stress compared to Fe_3O_4 composite-based suspensions. In addition, 3-dimensional network structures were formed in the suspension due to the high aspect ratio of CNTs, resulting in excellent long-term stability against particle sedimentation. From these results, it could be concluded that by exchanging magnetic materials from Fe_3O_4 to $\text{Co}_{0.4}\text{Fe}_{0.4}\text{Ni}_{0.2}$ and morphologies from spherical shape to shape with high aspect ratio, the trade-off between performance and long-term stability of MR fluids can be decreased.

In this chapter, to enhance performance of MR fluids more from that of CNT-

$\text{Co}_{0.4}\text{Fe}_{0.4}\text{Ni}_{0.2}$ fluids, magnetically-inactive CNTs were replaced with magnetic, flake-shaped sendust. Sendust is iron-based magnic alloy material with composition of 85 % iron, 6 % silicon and 9 % aluminum. It has been used as magnetic absorption materials in magnetic-dielectric composite materials for electromagnetic interference shielding. [20,21] Because it has very high saturation magnetization value (~ 130 emu/g), sendust can be a candidate materials for high-performance MR fluids. Also, the flake shape of sendust make them to be proper materials as supports for $\text{Co}_{0.4}\text{Fe}_{0.4}\text{Ni}_{0.2}$ nanoparticles, imparting outstanding long-term stability for MR suspensions. In a previous study, lee et al reported that the sedimentation velocity of anisotropic, flake-shaped carbonyl iron (CI) in MR fluids was slower than spherical-shaped CI because of high friction force resulting from the large surface area of the flake-shaped CI particles, interfering sedimentation of the particles. [22]

For this work, flake-shaped sendust@ $\text{Co}_{0.4}\text{Fe}_{0.4}\text{Ni}_{0.2}$ (FS@ $\text{Co}_{0.4}\text{Fe}_{0.4}\text{Ni}_{0.2}$) composite particles were obtained with synthesis of $\text{Co}_{0.4}\text{Fe}_{0.4}\text{Ni}_{0.2}$ on the surface of FS. By attaching $\text{Co}_{0.4}\text{Fe}_{0.4}\text{Ni}_{0.2}$ with very high magnetization value onto magnetic sendust, the composite particles have magnetization value higher than FS while its density is lowered. This improvement in magnetic properties directly leads to outstanding performacne of MR fluids. At the same time, the high drag coefficient of FS slowed sedimentation velocity of FS@ $\text{Co}_{0.4}\text{Fe}_{0.4}\text{Ni}_{0.2}$ greatly, resulting in excellent long-term stability of FS@ $\text{Co}_{0.4}\text{Fe}_{0.4}\text{Ni}_{0.2}$ suspension.

6. 2. Experimental Section

6. 2. 1. Synthesis of Flake-Shaped Sendust@Co_{0.4}Fe_{0.4}Ni_{0.2}

(FS@Co_{0.4}Fe_{0.4}Ni_{0.2})

FS@Co_{0.4}Fe_{0.4}Ni_{0.2} magnetic-magnetic composite particles were obtained by simply synthesizing Co_{0.4}Fe_{0.4}Ni_{0.2} in the existence of FS. First, FS (3 g) was dispersed in ethanol/H₂O (400 ml, 3:1 v:v ratio) mixed solvent through ultrasonication. CoCl₂ 6H₂O (4.953 g), FeCl₂ 4H₂O (4.137 g), and Ni(NO₃)₂ 6H₂O (3.027 g) were dissolved to mixture under nitrogen atmosphere. After dissolution of precursors at room temperature, 6 M NaOH solution (5.8 ml) was injected and the solution was heated to 80 °C. Then, hydrazine monohydrate (30 ml) was slowly injected at the temperature, and reaction was progressed for 45 min with removing nitrogen flow. The final product was collected with permanent magnet, washed several times with H₂O and ethanol, and dried in vacuum for 24 h. The weight ratio of CI and Co_{0.4}Fe_{0.4}Ni_{0.2} calculated from the amount of CI and Co_{0.4}Fe_{0.4}Ni_{0.2} was 1:1

6. 2. 2. Characterization

Surface morphologies of FS and FS@Co_{0.4}Fe_{0.4}Ni_{0.2} was examined and compared using scanning electron microscopy (SEM; JSM-7600F, JEOL, Tokyo, Japan). The magnetic

properties of the two particles were measured with vibrating sample magnetometer (VSM; VSM-7410, Lake Shore Cryotronics, USA) from -10 kOe to 10 kOe magnetic field range. The densities of magnetic particles were measured with helium pycnometer (AccuPyc 1330, Micromeritics Instrument Corporation, Norcross, USA). MR fluids for MR properties and long-term stability tests were obtained by dispersing magnetic particles in silicone oil (KF-96, 10 cS, Shin Etsu, Japan) with 10 vol % of concentration. MR properties of each fluid were observed using a rotational rheometer (Physica MCR301, Stuttgart, Germany) equipped with a magnetic generator (Physica MRD 180, Stuttgart, Germany). Finally, long-term stability of the MR fluids were evaluated through observing light transmission change of MR fluids for 24h using turbiscan (Classic MA2000, Formulation, France).

6. 3. Results and Discussion

6. 3. 1. Morphologies and Structures

Figure 6.1 is the SEM images for FS (6.1-(a) and (b)) and FS@Co_{0.4}Fe_{0.4}Ni_{0.2} (6.1-(c) and (d)) particles. Before attachment of Co_{0.4}Fe_{0.4}Ni_{0.2} nanoparticles, FS has plate-like shape and relatively smooth surface with very little roughness. With synthesis of Co_{0.4}Fe_{0.4}Ni_{0.2} nanoparticles with existence of FS, it is clearly observed with magnified SEM image (Figure 6.1-(d)) that Co_{0.4}Fe_{0.4}Ni_{0.2} nanoparticles were attached on the surface FS, increasing the roughness of surface. With attachment of Co_{0.4}Fe_{0.4}Ni_{0.2}, the density of magnetic particles decreased from 7.20 g/cm³ for FS to 5.75 g/cm³ for FS@Co_{0.4}Fe_{0.4}Ni_{0.2} although the density of Co_{0.4}Fe_{0.4}Ni_{0.2} (7.85 g/cm³) is higher than that of FS. It is known that aluminum, one of the components of sendust can be etched in alkali metal hydroxide solution. [23] For synthesis of FS@Co_{0.4}Fe_{0.4}Ni_{0.2} in this work, NaOH was used to precipitate metal ions. Thus, Al component in sendust would be etched by NaOH and pores were formed inside the sendust. In addition, pores can also be formed between surface of FS and Co_{0.4}Fe_{0.4}Ni_{0.2}. Similar to HS-Fe₃O₄ in chapter 4, such pores is expected to be the reason for reduction in density of FS@Co_{0.4}Fe_{0.4}Ni_{0.2} despite of absence of light materials.

The magnetic properties of Co_{0.4}Fe_{0.4}Ni_{0.2}, FS, and FS@Co_{0.4}Fe_{0.4}Ni_{0.2} measured with VSM are illustrated in Figure 6.2. The saturation magnetization of each particles was 165, 130 and 145 emu/g for Co_{0.4}Fe_{0.4}Ni_{0.2}, FS, and FS@Co_{0.4}Fe_{0.4}Ni_{0.2}, respectively. With

attachment of $\text{Co}_{0.4}\text{Fe}_{0.4}\text{Ni}_{0.2}$ with higher magnetization value than FS, $\text{FS}@_{\text{Co}_{0.4}\text{Fe}_{0.4}\text{Ni}_{0.2}}$ has saturation magnetization value higher than FS. When VSM profile of each sample was compared, $\text{Co}_{0.4}\text{Fe}_{0.4}\text{Ni}_{0.2}$ showed typical hysteresis curve with relatively large remnant magnetization (17.0 emu/g) and slow increase of magnetization with field strength while FS have small remnant magnetization (4.6 emu/g) and very fast increase of magnetization with magnetic field at low field strength range. This difference is concerned with a geometry dependent constant for magnetization, demagnetization factor, which is used for determination of internal and external field values in magnetic particles induced by applied magnetic fields. [24] The demagnetization factor along longitudinal direction flake-shaped particles is much smaller than spherical magnetic particles and flake-shaped particles are magnetized very easily along the direction. [24-26] Thus, the magnetization of FS increases very quickly with magnetic field at low field strength range. FS have very small coercive field despite of small demagnetization factor owing to evenly oriented magnetic domains with applied magnetic field in single layer. $\text{FS}@_{\text{Co}_{0.4}\text{Fe}_{0.4}\text{Ni}_{0.2}}$ has mixed magnetic characteristic of FS and $\text{Co}_{0.4}\text{Fe}_{0.4}\text{Ni}_{0.2}$. The remnant magnetization (5.2 emu/g) and coercive field value of $\text{Co}_{0.4}\text{Fe}_{0.4}\text{Ni}_{0.2}$ was very closed to that of FS rather than average of FS and $\text{Co}_{0.4}\text{Fe}_{0.4}\text{Ni}_{0.2}$, although expected weight ratio between FS and $\text{Co}_{0.4}\text{Fe}_{0.4}\text{Ni}_{0.2}$ in $\text{FS}@_{\text{Co}_{0.4}\text{Fe}_{0.4}\text{Ni}_{0.2}}$ was 1:1. In contrast, the tendency of magnetization increase with field strength was more closed to that of $\text{Co}_{0.4}\text{Fe}_{0.4}\text{Ni}_{0.2}$. Thus, it can be concluded that magnetic properties near zero field are governed by geometric factor of FS, while properties at higher field are determined by $\text{Co}_{0.4}\text{Fe}_{0.4}\text{Ni}_{0.2}$, which has higher saturation magnetization value.

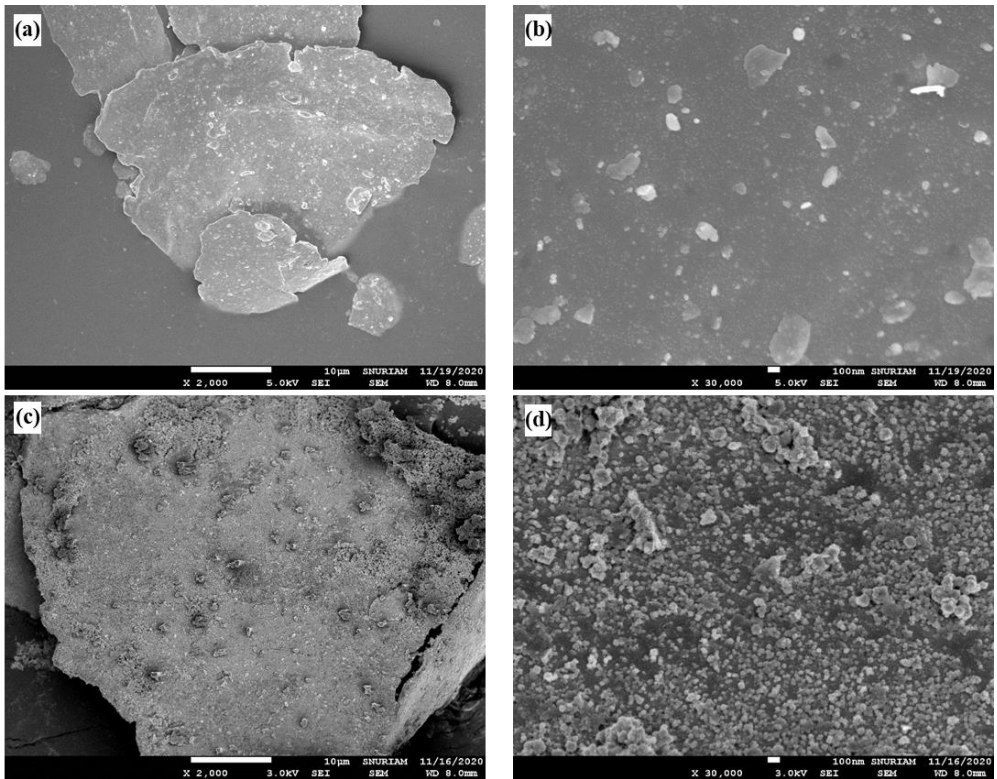


Figure 6. 1. SEM images of (a),(b) flake sendust ((b) is magnified image of surface)) and (c),(d) FS@Co_{0.4}Fe_{0.4}Ni_{0.2} ((d) is magnified image of surface)

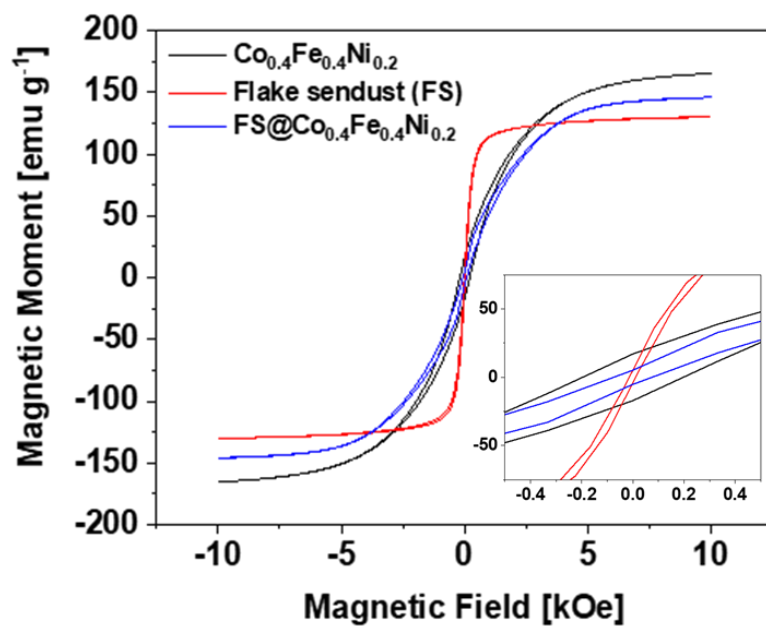


Figure 6. 2. VSM curves for Co_{0.4}Fe_{0.4}Ni_{0.2}, FS, and FS@Co_{0.4}Fe_{0.4}Ni_{0.2}

6. 3. 2. Magnetorheological Properties

Figure 6.3 is the results of change in viscoelastic properties with shear strain (amplitude sweep, Figure 6.3-(a)) and angular frequency (frequency sweep, Figure 6.3-(b)) of FS and FS@Co_{0.4}Fe_{0.4}Ni_{0.2} suspension at two different magnetic field strength. In amplitude sweep results, the plateau region, called viscoelastic region where storage modulus of suspensions was not almost changed with strain was observed. In this region, field-induced magnetostatic interaction overwhelms the shear-induced hydrodynamic interaction, proving successful formation of chain-like structures with magnetic field. [1] With continuous increase of shear strain, chain-like structures are destroyed by hydrodynamic stress, and storage modulus starts to decrease. [1,3] The magnitude of storage modulus increased with magnetic field strength due to enhanced interaction between magnetic particles, proving the modifiability of rheological properties with field strength. Frequency sweep results showed similar change of storage modulus with field strength. When storage modulus of each test is compared with loss modulus, it is higher by about 1 order of magnitude, and does not show remarkable change with frequency. [27] This shows that solid-like elastic properties of MR fluids imparted by formation of chain-like structures is dominant over liquid-like viscous properties, and the mesostructures maintain their undisturbed state for all frequency range. [3,5,28]

Figure 6.4 shows shear stress and viscosity curve of FS and FS@Co_{0.4}Fe_{0.4}Ni_{0.2} as the function of shear rate (0.1-500 s⁻¹) for two different magnetic field, 86 and 343 kA/m. Behavior of MR fluids in shear stress curve can be divided into two regions with shear rate

range. At low shear rate range, chain-like structures can withstand hydrodynamic stress and shear stress shows little change with shear rate. In contrast, as hydrodynamic stress increases with shear rate, it destroys the field-induced mesostructures, and shear stress also increase with shear rate. [3,5] The shear stress curve for all tests showed the explained behavior. When the structural change of partial break and restoration of chain-like structures occurs at intermediate shear rate range, shear stress curve shows sudden decrease and subsequent increase of shear stress before complete destruction of the mesostructures. [5] This phenomena was not observed for FS and FS@Co_{0.4}Fe_{0.4}Ni_{0.2} suspension, meaning chain-like structures in the two suspensions was robust enough to endure external shear at intermediate shear rate range. When shear stress at low shear rate of two suspensions was compared, two suspensions showed different tendency of shear stress change with magnetic field strength. At the field strength of 86 kA/m, shear stress of FS suspension was almost twice of FS@Co_{0.4}Fe_{0.4}Ni_{0.2} suspension. In contrast, when field strength of 343 kA/m was applied to the two MR fluids, FS@Co_{0.4}Fe_{0.4}Ni_{0.2} suspension showed larger increase of shear stress with field strength, and difference in shear stress between FS and FS@Co_{0.4}Fe_{0.4}Ni_{0.2} at 343 kA/m was much smaller than the case of 86 kA/m. This is closely related to VSM results of the two magnetic particles and geometric factor of FS. This will be discussed further with yield stress measurement results. Viscosity of each test has same order with its shear stress as apparent viscosity is $\tau/\dot{\gamma}$. Same with shear stress results, the viscosity increased with magnetic field strength, and higher for FS suspension than FS@Co_{0.4}Fe_{0.4}Ni_{0.2} suspension.

The MR performance of FS and FS@Co_{0.4}Fe_{0.4}Ni_{0.2} was directly compared through theoretical expectation and experimental measurement of yield stress. Dynamic yield stress (τ_{dy}) and static yield stress (τ_{sy}) of two suspensions were expected using Bingham model and Seo-Seo model respectively. The equation for Bingham fluid model is

$$\tau = \tau_{dy} + \eta_{pl}\dot{\gamma} \quad (6.1)$$

with τ as shear stress, τ_{dy} as dynamic yield stress and η_{pl} is plastic viscosity of suspension at high shear rate, and $\dot{\gamma}$ is shear rate. [29] Dynamic yield stress in Bingham fluid model corresponds to complete destruction of chain-like structures. [29,30] Although this model is very simple for estimation of dynamic yield stress, structural change in intermediate shear rate cannot be expressed with this model. To predict yield stress under the condition of such structural change, static yield stress where flow of fluids is induced should be used. [31] Seo-Seo model for calculation of static yield stress is formulated as

$$\tau = \tau_{sy} \left(1 - \frac{(1 - \exp(-a\dot{\gamma}))}{(1 + (a\dot{\gamma})^\alpha)} \right) + \eta_{pl}\dot{\gamma} \quad (6.2)$$

with τ_{sy} as static yield stress and time constant a , the reciprocal of the critical shear rate for an aligned mesostructure deformation and power-law index α which determines the degree of shear thinning. [29,32,33] The factors a and α describes the partial destruction and reformation at intermediate shear rate, and when $a = 0$ equation (6.2) become same with Bingham fluid model. [33, 34] The experimental static yield stress with controlled shear stress (CSS) mode in rotational rheometer. [3,5,28] Viscosity of each sample was measured

as a function of shear stress and static yield stress was determined as shear stress value where huge decrease in viscosity was observed.

Measured static yield stress value of FS and FS@Co_{0.4}Fe_{0.4}Ni_{0.2} is illustrated in Figure 6.5 and compared with theoretic yield stress and yield stress of CNT-Co_{0.4}Fe_{0.4}Ni_{0.2} (from chapter 5) in Table 6.1. The three yield stresses of each sample have very similar values, showing the robustness of chain-like structures, as clearly seen in shear stress curves which do not exhibit sudden change in shear stress at low shear rate range. When yield stress of FS and FS@Co_{0.4}Fe_{0.4}Ni_{0.2} was compared, two samples have different increasing tendency of yield stress with magnetic field strength. For FS suspension, measured static yield stress increased about 2.2 times (2762 Pa to 6078 Pa) when magnetic field strength increased from 86 kA/m to 343 kA/m. Meanwhile, static yield stress of FS@Co_{0.4}Fe_{0.4}Ni_{0.2} suspension increased about 3.7 times (1447 Pa to 5412 Pa) with same change of field strength. The yield stress of FS was almost twice of FS@Co_{0.4}Fe_{0.4}Ni_{0.2} at 86 kA/m while it was only 1.12 times of yield stress of FS@Co_{0.4}Fe_{0.4}Ni_{0.2} at 343 kA/m. Such different tendency in yield stress increase with magnetic field strength can be explained with contrasting magnetic properties of the two magnetic materials. As stated with VSM results, due to small demagnetization factor in longitudinal direction, the magnetization of FS increased much faster than FS@Co_{0.4}Fe_{0.4}Ni_{0.2} at low magnetic field strength range and reach saturation value at relatively low field strength. [24-26] Magnetic field strength of 86 kA/m corresponds to 1.08 kOe in VSM curves, where magnetization of FS is much higher and this results in yield stress of FS much higher than FS@Co_{0.4}Fe_{0.4}Ni_{0.2}. In

contrast, magnetization of FS@Co_{0.4}Fe_{0.4}Ni_{0.2} increases slowly with field strength and at 343 kA/m where both magnetic materials in almost magnetically saturated state, the magnetization FS@Co_{0.4}Fe_{0.4}Ni_{0.2} became larger than that of FS. Thus, increase in yield stress with magnetic field strength is larger for FS@Co_{0.4}Fe_{0.4}Ni_{0.2}. The static yield stress for FS@Co_{0.4}Fe_{0.4}Ni_{0.2} at 343 kA/m was about 89 % of that for FS. The density of FS@Co_{0.4}Fe_{0.4}Ni_{0.2} is 80 % of FS, which means at same volume concentration of magnetic particles, the weight of magnetic particles per unit volume of FS@Co_{0.4}Fe_{0.4}Ni_{0.2} fluid is 80 % of FS suspension. Thus the ratio of yield stress between FS@Co_{0.4}Fe_{0.4}Ni_{0.2} and FS is higher than the ratio of density between two materials. Because FS@Co_{0.4}Fe_{0.4}Ni_{0.2} have larger saturation magnetization value (145 emu/g) than FS (130 emu/g), the decrease in yield stress with reduction of density through fabrication of FS@Co_{0.4}Fe_{0.4}Ni_{0.2} could be minimized. When the measured static yield stress of FS@Co_{0.4}Fe_{0.4}Ni_{0.2} is compared with that of CNT-Co_{0.4}Fe_{0.4}Ni_{0.2}, it is 325 % and 285 % of CNT-Co_{0.4}Fe_{0.4}Ni_{0.2} at 86 kA/m and 343 kA/m, respectively. By replacing magnetically-inactive CNTs with sendust which is magnetic materials with high magnetization value, the reduction in saturation magnetization value from that of Co_{0.4}Fe_{0.4}Ni_{0.2} could be minimized, and this directly contributed much better MR performance of FS@Co_{0.4}Fe_{0.4}Ni_{0.2} fluid compared to CNT-Co_{0.4}Fe_{0.4}Ni_{0.2} fluid.

The reversibility of MR behavior induced by formation of chain structures was examined with switching magnetic field. Figure 6. 6 is the results of transient response of FS and FS@Co_{0.4}Fe_{0.4}Ni_{0.2} suspensions through on-off cycles of magnetic field at shear rate of 1

s⁻¹. For both samples shear stress increased suddenly with application of magnetic field and returned to original state for 3 on-off cycles. Thus, transition of MR fluids between solid-like state and liquid-like state is reversible. Also, the maximum shear stress value under magnetic field for each test was very close to its yield stress, which proves the validity of the data.

The behavior of MR fluids is determined by hydrodynamic drag force and magnetostatic forces and dependent on the ratio between the two forces, called Mason number, $M_n = 8\eta_0\dot{\gamma}/\mu_0\mu_c\beta^2 M^2$. [35-37] In this equation, η_0 is the medium viscosity, $\dot{\gamma}$ is the shear rate, β is the contrast factor ($= (\mu_p - \mu_c)/(\mu_p + 2\mu_c)$), μ_p is the particle relative permeability, μ_c is the relative permeability of the liquid medium phase, and $\mu_0 = 4\pi \times 10^{-7} \text{ N}/\text{A}^2$ is the vacuum permeability, and M is the magnetic field strength. [36, 37] $\eta_0\dot{\gamma}$ term is hydrodynamic force induced by continuous shear and M^2 term is field-induced magnetic polarization force. M_n is equivalent to $\dot{\gamma}/M^2$, and proportional to reciprocal of apparent viscosity, $\tau/\dot{\gamma}$. [36] Thus, for fixed volume fraction by rescaling shear rate in viscosity curve (Figure 6.4 (b)) with M^2 and apparent viscosity with appropriate factor, it is possible to obtain master curve for the specific viscosity (apparent viscosity divided by medium viscosity) against $\dot{\gamma}/M^2$ and compare the behavior of different MR fluids. [36-38] Figure 6.7 shows curves of corrected viscosities versus $\dot{\gamma}/M^2$ for FS and FS@Co_{0.4}Fe_{0.4}Ni_{0.2} at two different magnetic field. All four curves showed exact overlap, meaning the two MR fluids have same MR behavior each other regardless of field strength. Also, when these curves are compared with those in previous chapters, all curves have

same scaling law although magnetic materials used have some different magnetic properties. Thus, it can be concluded that behavior of MR fluids is regardless of particle's morphology and type of magnetic materials.

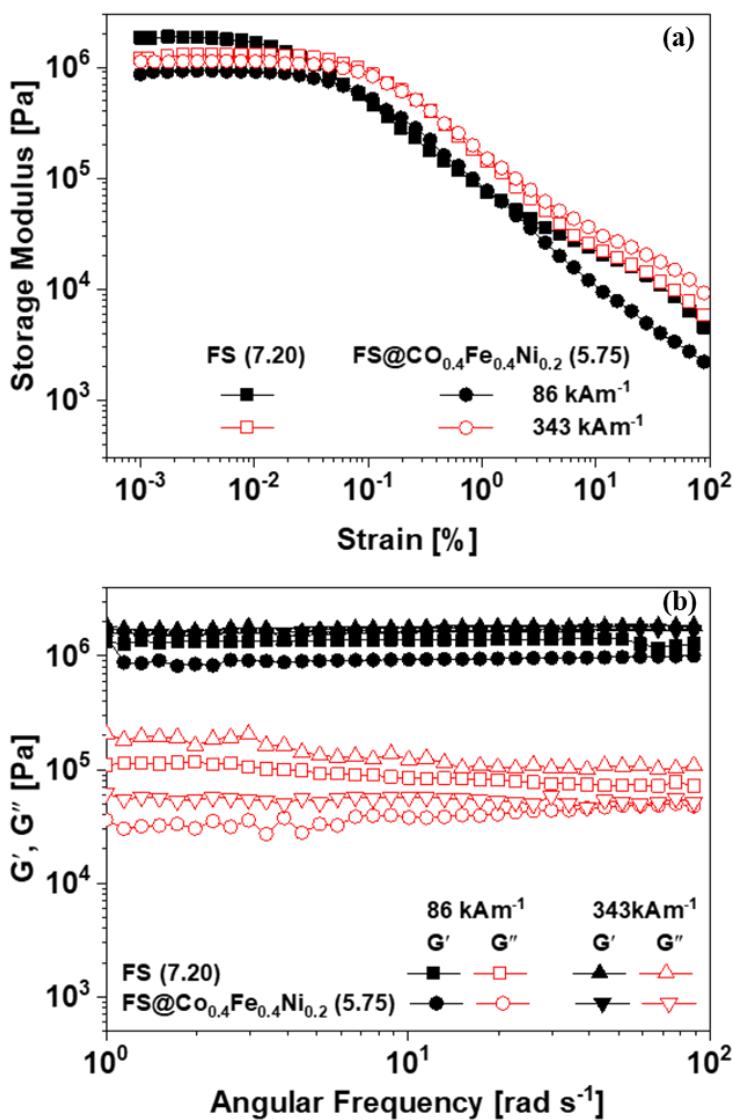


Figure 6. 3. (a) amplitude sweep (strain dependence) of storage modulus, G' and (b) Frequency sweep (frequency dependence) of storage modulus (G') and loss modulus(G'') for FS and FS@Co_{0.4}Fe_{0.4}Ni_{0.2} suspension at 86 kA/m and 343 kA/m.

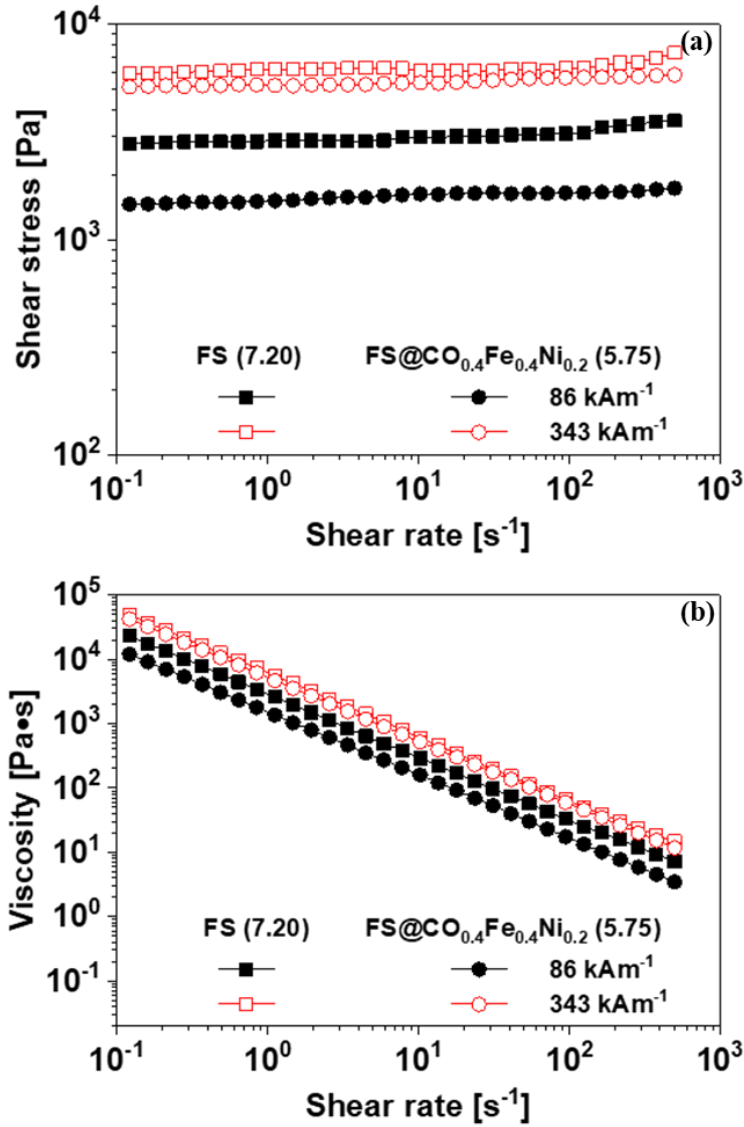


Figure 6. 4. (a) shear stress and (b) viscosity curves as a function of shear rate for MR fluids of FS and FS@ $Co_{0.4}Fe_{0.4}Ni_{0.2}$

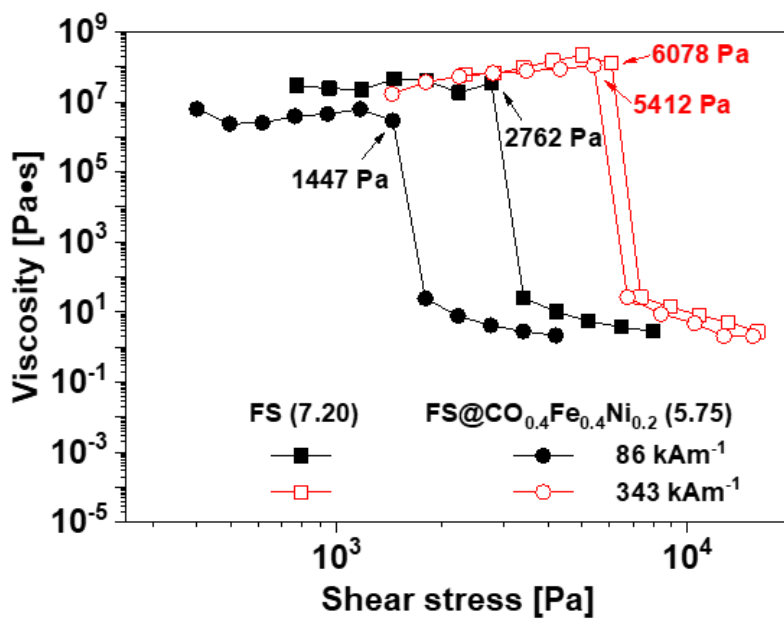


Figure 6. 5. Shear viscosity as a function of shear stress for FS and FS@Co_{0.4}Fe_{0.4}Ni_{0.2} MR fluids at 86 kA/m and 343 kA/m.

Table 6. 1. Static yield stress and dynamic yield stress of $\text{Co}_{0.4}\text{Fe}_{0.4}\text{Ni}_{0.2}$, FS, and $\text{Co}_{0.4}\text{Fe}_{0.4}\text{Ni}_{0.2}$ composites-based MR fluids

	Yield stress (Pa)					
	M = 86 (kA/m)			M = 343 (kA/m)		
	Static exp (τ_{sy})	Dynamic (τ_{dy})	Static SS (τ_{sy})	Static exp (τ_{sy})	Dynamic (τ_{dy})	Static SS (τ_{sy})
$\text{Co}_{0.4}\text{Fe}_{0.4}\text{Ni}_{0.2}$ (7.85 g/cm ³)	1560	1601	1561	7052	7120	7150
FS (7.20 g/cm ³)	2762	2908	2817	6078	6093	6127
FS@ $\text{Co}_{0.4}\text{Fe}_{0.4}\text{Ni}_{0.2}$ (5.75 g/cm ³)	1447	1560	1542	5412	5303	5431
CNT- $\text{Co}_{0.4}\text{Fe}_{0.4}\text{Ni}_{0.2}$ (4.12 g/cm ³)	445	472	485	1901	1887	1889

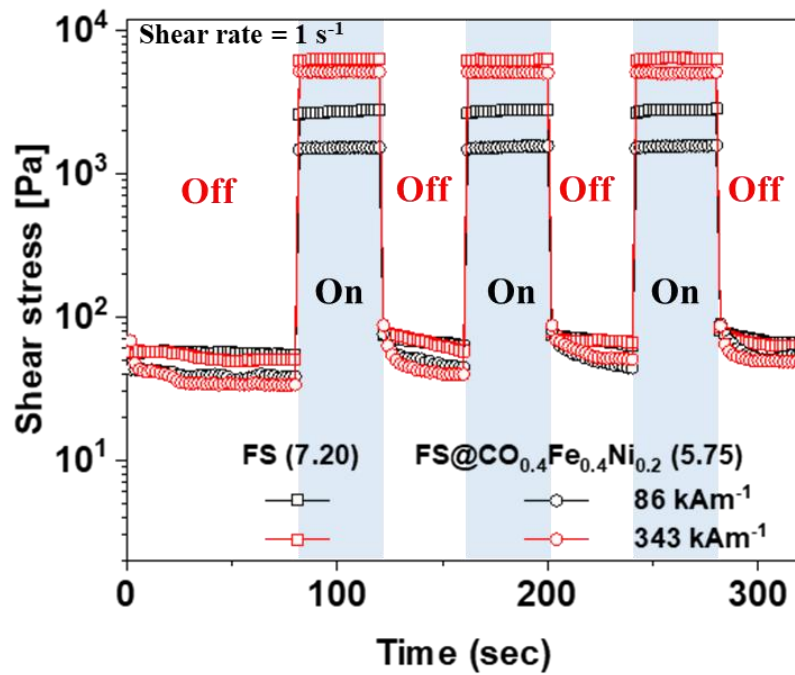


Figure 6. 6. Transient responses (reversibility) of the FS and FS@Co_{0.4}Fe_{0.4}Ni_{0.2} MR fluids at shear rate of 1 s⁻¹.

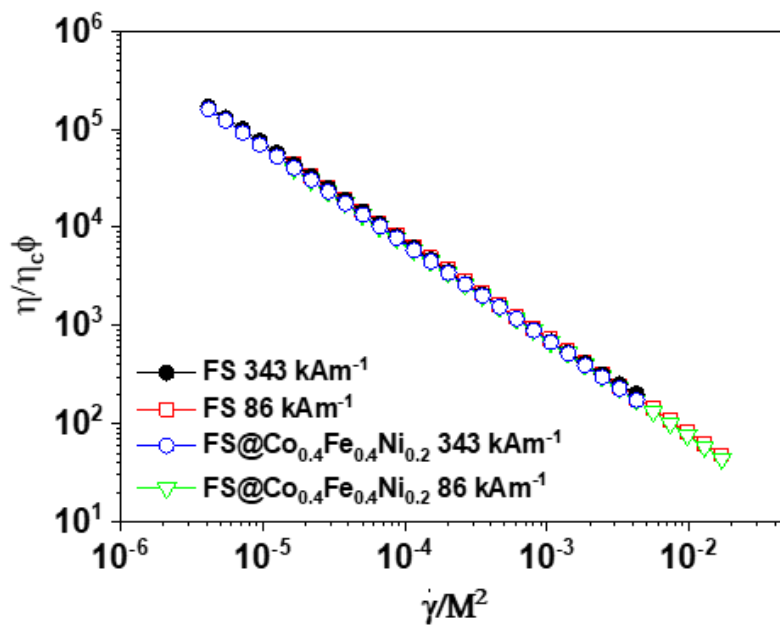


Figure 6. 7. Dimensionless apparent viscosity of the MR fluids as a function of $\dot{\gamma}/M^2$ at various magnetic field strengths.

6. 3. 3. Long-Term Stability of Suspensions

The long-term stability of FS and FS@Co_{0.4}Fe_{0.4}Ni_{0.2} MR suspensions was evaluated by observing light transmission change over 24 h. Light transmission of the two suspensions increased very quickly at early stage of the tests then the sedimentation velocity slow down. After early stage, pronounced change in transmission was not observed until 24 h. Final transmission value at 24 h was 33 and 23 % for FS and FS@Co_{0.4}Fe_{0.4}Ni_{0.2} which means FS@Co_{0.4}Fe_{0.4}Ni_{0.2} suspension have better long-term stability than FS suspension. When those transmission values are compared with that of Co_{0.4}Fe_{0.4}Ni_{0.2} bare particles (81 %), both samples exhibit highly enhanced stability despite of their high density. For spherical particles the initial sedimentation velocity of the particles follows the equation

$$V(\phi, d) = \frac{|\rho_p - \rho_c| \times g \times d^2}{18 \times \nu \times \rho_c} \cdot \frac{[1 - \phi]}{\left[1 + \frac{4.6\phi}{(1 - \phi)^3}\right]} \quad (6.3)$$

where V is the particle migration velocity (m s^{-1}), ρ_p presents the particle density, ρ_c is the continuous phase density (kg m^{-3}), ν denotes the kinematic viscosity of continuous phase, g is gravity constant (9.81 m s^{-2}), d means the particle diameter, and ϕ represents the volume fraction of the particles. [39] If particle diameter term can be neglected due to friction between rough particles, the density difference between particle and medium determined the sedimentation velocity. [5] According to this equation, FS and FS@Co_{0.4}Fe_{0.4}Ni_{0.2} should have very high transmission value because they have large density. However, as FS and FS@Co_{0.4}Fe_{0.4}Ni_{0.2} have flake shape, the effect of particle

morphology on long-term stability should be considered. The excellent stability results for those particles is concerned with a terminal velocity, u_t

$$u_t = \left(\frac{4 Re}{3 C_D} \right)^{1/3} \left[\frac{\rho_f^2}{g\mu(\rho_s - \rho_f)} \right]^3 \quad (6.4)$$

where Re is Reynolds number related to equivalent diameter which is diameter of sphere with same volume, and C_D is a drag coefficient. [40-43] Flake-shaped particles, Reynolds number is smaller than spherical shaped particles due to small equivalent diameter and drag coefficient increases as Reynolds number decreases. [44,45] Thus, for flake shaped particles, terminal velocity u_t become much smaller compared to spherical particles, resulting in much lower light transmission value. When light transmission values of FS and FS@Co_{0.4}Fe_{0.4}Ni_{0.2} were compared, FS@Co_{0.4}Fe_{0.4}Ni_{0.2} showed lower value, which is attributed to reduction of particle density with synthesis of Co_{0.4}Fe_{0.4}Ni_{0.2} on the surface of FS. Also, this results is comparable to that of CNT- Co_{0.4}Fe_{0.4}Ni_{0.2} whose light transmission was 22 %, while yield stress of FS@Co_{0.4}Fe_{0.4}Ni_{0.2} was almost 3 times of Co_{0.4}Fe_{0.4}Ni_{0.2}. Thus, it could be concluded that by replacing CNTs with magnetic, flake-shaped FS, the enormous enhancement in MR performance could be achieved without harming long-term stability of MR suspension.

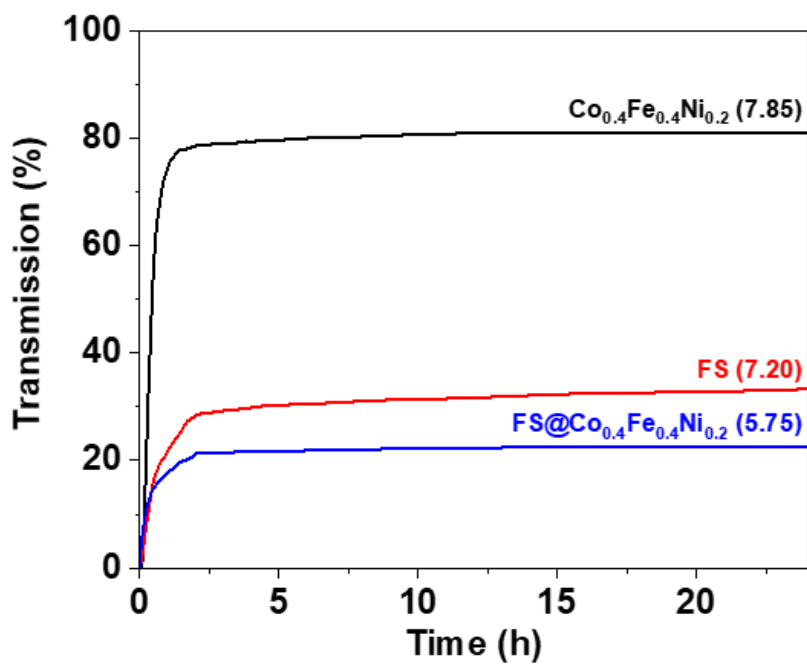


Figure 6. 8. Transmission (%) curve as a function of time (h) for $\text{Co}_{0.4}\text{Fe}_{0.4}\text{Ni}_{0.2}$, FS, and $\text{FS@Co}_{0.4}\text{Fe}_{0.4}\text{Ni}_{0.2}$ particles for 24h.

6. 4. Conclusion

The present study offers the flake-shaped $\text{FS@Co}_{0.4}\text{Fe}_{0.4}\text{Ni}_{0.2}$ magnetic-magnetic composite for simultaneous improvement of MR fluids' performance and long-term stability. $\text{FS@Co}_{0.4}\text{Fe}_{0.4}\text{Ni}_{0.2}$ composite particles were obtained by simply synthesizing $\text{Co}_{0.4}\text{Fe}_{0.4}\text{Ni}_{0.2}$ nanoparticles on the surface of FS. As a result, flake-shaped composite magnetic particles were fabricated. With attachment of $\text{Co}_{0.4}\text{Fe}_{0.4}\text{Ni}_{0.2}$, the saturation magnetization of $\text{FS@Co}_{0.4}\text{Fe}_{0.4}\text{Ni}_{0.2}$ (145 emu/g) became higher than FS (130 emu/g), while the density (5.75 g/cm^3) decreased from that of FS (7.20 g/cm^3). At low magnetic field strength, FS has a relatively high magnetization value due to a low demagnetization factor, leading to a yield stress of FS almost twice higher than that of $\text{FS@Co}_{0.4}\text{Fe}_{0.4}\text{Ni}_{0.2}$. However, due to higher saturation magnetization, the yield stress of $\text{FS@Co}_{0.4}\text{Fe}_{0.4}\text{Ni}_{0.2}$ suspension was comparable to FS suspension despite of lower content of magnetic materials for $\text{FS@Co}_{0.4}\text{Fe}_{0.4}\text{Ni}_{0.2}$ suspension. In addition, when the yield stress of $\text{FS@Co}_{0.4}\text{Fe}_{0.4}\text{Ni}_{0.2}$ was compared to the yield stress of CNT- $\text{Co}_{0.4}\text{Fe}_{0.4}\text{Ni}_{0.2}$ in the previous chapter, it was higher by about 300 % due to an enhanced response to magnetic field with replacement of non-magnetic CNTs to magnetic FS. At the same time, the geometric factor also helped the improvement in long-term stability of MR suspensions. The reduced terminal velocity due to a high drag coefficient, combined with lowered density of $\text{FS@Co}_{0.4}\text{Fe}_{0.4}\text{Ni}_{0.2}$ compared to bare FS, resulted in long-term stability of 23 % light

transmission comparable to CNT-Co_{0.4}Fe_{0.4}Ni_{0.2} suspension. These results can suggest a solution for solving problem of trade-off between MR performance and long-term stability.

References

- (1) Seo, Y. P.; Han, S.; Choi, J.; Takahara, A.; Choi, H. J.; Seo, Y., Searching for a stable high-performance magnetorheological suspension. *Adv. Mater.* 2018, 30 (42), 1704769.
- (2) Ahamed R.; Choi S.B.; Ferdaus M., A state of art on magneto-rheological materials and their potential applications, *J. Intellig. Mat. Syst. Struct.* 2018, 29(10) 2051-2095
- (3) Chuah, W. H.; Zhang, W. L.; Choi, H. J.; Seo, Y., Magnetorheology of core-shell structured carbonyl iron/polystyrene foam microparticles suspension with enhanced stability. *Macromolecules* 2015, 48 (19), 7311-7319.
- (4) Seo, Y.; Choi, H. J., Core-shell-structured Fe₃O₄ nanocomposite particles for high-performance/stable magnetorheological fluids: preparation and characteristics. *J. Korean Ceram. Soc.* 2020, 57, 608-631.
- (5) Han, S.; Choi, J.; Seo, Y. P.; Park, I. J.; Choi, H. J.; Seo, Y., High-performance magnetorheological suspensions of pickering-emulsion-polymerized polystyrene/Fe₃O₄ particles with enhanced stability. *Langmuir* 2018, 34 (8), 2807-2814.
- (6) Park, B. J.; Fang, F. F.; Choi, H. J., Magnetorheology: materials and application. *Soft Matter* 2010, 6 (21), 5246-5253.
- (7) Ashtiani, M.; Hashemabadi, S.; Ghaffari, A., A review on the

magnetorheological fluid preparation and stabilization. *J. Magn. Magn. Mater.* 2015, 374, 716-730.

(8) Bitaraf, M.; Ozbulut, O. E.; Hurlebaus, S.; Barroso, L., Application of semi-active control strategies for seismic protection of buildings with MR dampers. *Eng. Struct.* 2010, 32 (10), 3040-3047.

(9) Chen, Z.; Wang, X.; Ko, J.; Ni, Y.; Spencer Jr, B. F.; Yang, G. In MR damping system on Dongting Lake cable-stayed bridge, *Smart Structures and Materials 2003: Smart Systems and Nondestructive Evaluation for Civil Infrastructures*, International Society for Optics and Photonics: 2003; pp 229-235.

(10) Seo, Y. P.; Choi, H. J.; Seo, Y., Analysis of the flow behavior of electrorheological fluids with the aligned structure reformation, *Polymer*, 2011, 52 (25), 5695-5698

(11) Cvek, M.; Mrlik, M.; Ilcikova, M.; Plachy, T.; Sedlacik, M.; Mosnacek, J.; Pavlinek, V., A facile controllable coating of carbonyl iron particles with poly(glycidyl methacrylate): a tool for adjusting MR response and stability properties. *J. Mater. Chem. C* 2015, 3 (18), 4646-4656.

(12) Pu, H. T.; Jiang, F. J.; Yang, Z.-l., Preparation and properties of soft magnetic particles based on Fe₃O₄ and hollow polystyrene microsphere composite. *Materials Chemistry and Physics* 2006, 100 (1), 10-14.

(13) Du, Z.; Qiu, Y.; Niu, T.; Wang, W.; Ye, X.; Wang, J.; Zhang, W. L.; Choi, H. J.; Zeng, H., Bio-inspired passion fruit-like Fe₃O₄@C nanospheres enabling high-

stability magnetorheological performances. *Langmuir* 2020, 36 (26), 7706-7714.

(14) Fang, F. F.; Kim, J. H.; Choi, H. J., Synthesis of core-shell structured PS/Fe₃O₄ microbeads and their magnetorheology. *Polymer* 2009, 50 (10), 2290-2293.

(15) Kim, J. N.; Dong, Y. Z.; Choi, H. J., Pickering Emulsion Polymerized Polyaniline/Zinc-ferrite Composite Particles and Their Dual Electrorheological and Magnetorheological Responses. *ACS omega* 2020, 5 (13), 7675-7682.

(16) Yoon, C.-M.; Jang, Y.; Lee, S.; Jang, J., Dual electric and magnetic responsivity of multilayered magnetite-embedded core/shell silica/titania nanoparticles with outermost silica shell. *J. Mater. Chem. C* 2018, 6 (38), 10241-10249.

(17) Lee, J. H.; Lu, Q.; Lee, J. Y.; Choi, H. J., Polymer-Magnetic Composite Particles of Fe₃O₄/Poly (o-anisidine) and Their Suspension Characteristics under Applied Magnetic Fields. *Polymers* 2019, 11 (2), 219.

(18) He, M.; Zeng, Y.; Zhou, F.; Kong, G.; Lu, Y.; Chen, W.; Ma, Y.; Yu, R.; Wang, Z.; Li, Z., MnFe₂O₄ nanoparticles anchored on the surface of MgAl-layered double hydroxide nanoplates for stable magnetorheological fluids. *J. Mol. Liq.* 2020, 114098.

(19) Choi, J.; Han, S.; Kim, H.; Shn, E. H.; Choi, H. J.; Seo, Y., Suspensions of Hollow Polydivinylbenzene Nanoparticles Decorated with Fe₃O₄ Nanoparticles as Magnetorheological Fluids for Microfluidics Applications. *ACS Appl. Nano Mater.* 2019, 2 (11), 6939-6947.

- (20) Oh, K.; Hong, S. M.; Seo, Y. Effect of crosslinking reaction on the electromagnetic interference shielding of a Fe–Si–Al alloy (Sendust)/polymer composite at high frequency. *Polym. Adv. Technol.* 2014, 25, 1366–1370
- (21) Kim, H.; Park, S.; Kim, S.; Seo, Y., Microwave Absorption and Shielding Property of Fe–Si–Al Alloy/MWCNT/Polymer Nanocomposites. *Langmuir* 2019, 35 (21), 6950-6955.
- (22) Lee, J. Y.; Kwon, S. H.; Choi, H. J., Magnetorheological characteristics of carbonyl iron microparticles with different shapes. *Korea Aust. Rheol. J.* 2019, 31 (1), 41-47.
- (23) Sandaiji, H.; Ikeda, K.; Onishi, Y. (NGK Insulators Ltd.). Method of producing a core for magnetic head. US Patent 5063653, November 12, 1991
- (24) Pugh, B. K.; Kramer, D. P.; Chen, C. H. Demagnetizing factors for various geometries precisely determined using 3-D electromagnetic field simulation. *IEEE Trans. Magn.* 2011, 47 (10), 4100-4103.
- (25) Prozorov, R.; Kogan, V.G. Effective demagnetizing factors of diamagnetic samples of various shapes. *Phys. Rev. Applied.* 2018, 10, 014030
- (26) Vokoun, D.; De Graef, M. Demagnetization factors for cylindrical shells and related shapes. *Journal of Magnetism and Magnetic Materials.* 2009, 321 (9), 1306-1315
- (27) Upadhyay, R.; Laherisheth, Z.; Shah, K., Rheological properties of soft

magnetic flake shaped iron particle based magnetorheological fluid in dynamic mode.

Smart Mater. Struct. 2013, 23 (1), 015002

(28) Choi, J.; Han, S.; Kim, H.; Nam, K. T.; Seo, Y., Hierarchically Structured Fe₃O₄ Nanoparticles for High-Performance Magnetorheological Fluids with Long-Term Stability. *ACS Appl. Nano Mater.* 2020.

(29) Farjoud, A.; Vahdati, N.; Fah, Y. F., Mathematical model of drum-type MR brakes using Herschel-Bulkley shear model. *J. Intell. Mater. Syst. Struct.* 2008, 19 (5), 565-572.

(30) Seo, Y. P.; Seo, Y., Modeling and analysis of electrorheological suspensions in shear flow. *Langmuir* 2012, 28 (6), 3077-3084.

(31) Seo, Y. P.; Choi, H. J.; Lee, J. R.; Seo, Y., Modeling and analysis of an electrorheological flow behavior containing semiconducting graphene oxide/polyaniline composite particles. *Colloids Surf. A Physicochem. Eng. Asp.* 2014, 457, 363-367.

(32) Seo, Y. P.; Han, S.; Kim, J.; Choi, H. J.; Seo, Y., Analysis of the flow behavior of electrorheological fluids containing polypyrrole nanoparticles or polypyrrole/silica nanocomposite particles. *Rheol. Acta* 2020, 59 (6), 415-423.

(33) Seo, Y. P.; Kwak, S.; Choi, H. J.; Seo, Y., Static yield stress of a magnetorheological fluid containing Pickering emulsion polymerized Fe₂O₃ polystyrene composite particles. *J. Colloid Interface Sci.* 2016, 463, 272-278.

- (34) Seo, Y. P.; Han, S.; Kim, J.; Choi, H. J.; Seo, Y., Analysis of the flow behavior of electrorheological fluids containing polypyrrole nanoparticles or polypyrrole/silica nanocomposite particles. *Rheol. Acta* 2020, 59 (6), 415-423.
- (35) Ruiz-López, J. A.; Fernández-Toledano, J. C.; Hidalgo-Alvarez, R.; de Vicente, J., Testing the mean magnetization approximation, dimensionless and scaling numbers in magnetorheology. *Soft Matter* 2016, 12 (5), 1468-1476.
- (36) De Vicente, J.; Klingenberg, D. J.; Hidalgo-Alvarez, R., Magnetorheological fluids: a review. *Soft matter* 2011, 7 (8), 3701-3710.
- (37) Klingenberg, D.J.; Ulieny, J C.; Golden, M.A. Mason numbers for magnetorheology. *J. Rheol.* 2007, 51, 883-893.
- (38) Becnel, A. C.; Sherman, S.; Hu, W.; Wereley, N. M., Nondimensional scaling of magnetorheological rotary shear mode devices using the Mason number. *J. Magn. Magn. Mater.* 2015, 380, 90-97.
- (39) Mills, P.; Snabre, P., Settling of a suspension of hard spheres. *EPL* 1994, 25 (9), 651-656.
- (40) Jennings, B.R.; Parslow, K. Particle size measurement: the equivalent spherical diameter. *Royal society.* 1988, 1856 (419), 137-149
- (41) Gabitto, J.; Tsouris, C. Drag coefficient and settling velocity for particles of cylindrical shape. *Powder Technology.* 2008, 183 (2), 314-322

- (42) Komar, P. D.; Reimers, C.E. Grain shape effects on settling rates. *The journal of geology*. 1978, 86 (2), 193-209
- (43) Pettyjohn, E.S.; Christiansen E.B. Effect of particle shape on free settling rates of isomertric particles. *Chemical Enginerring Progress*. 1971, 9 (2), 285-291
- (44) Willmarth, W.; Hawk, N.; Harvey, R. Steady and unsteady motions and wakes of freely falling disks. *Physics of Fluids*. 1964, 7(2), 197-208
- (45) Bagheri, G.; Bonadonna, C.; On the drag of freely falling non-spherical particles. *Powder Technology*. 2016, 301, 526-544

Chapter 7. Conclusion

7.1. Overall conclusion

In summary, various magnetic composite materials were fabricated to obtain MR fluids having both excellent MR performance and long-term stability. The performance of MR fluids was evaluated with experimental measurement using rotational rheometer and theoretical prediction of dynamic yield stress and static yield stress using Bingham fluid model and Seo-Seo model. And long-term stability of MR suspensions were observed through light transmission change using turbiscan.

To solve the sedimentation problem first, hollow-structured PDVB@Fe₃O₄ (h-PDVB@Fe₃O₄) were prepared using SiO₂ as sacrificial template, PDVB as polymeric shell, and Fe₃O₄ as magnetic materials and used for MR fluids. Through distillation-precipitation polymerization of DVB on the surface of SiO₂, h-PDVB@Fe₃O₄ with relatively narrow size distribution could be obtained. Due to large cavity inside h-PDVB@Fe₃O₄, its density ($\rho = 1.82 \text{ g/cm}^3$) showed remarkable decrease from that of bare Fe₃O₄ nanoparticles ($\rho = 4.52 \text{ g/cm}^3$). The reduced density mismatch between magnetic particles and carrier medium resulted in highly improved long-term stability for inside h-PDVB@Fe₃O₄ suspension (13 % of light transmission) compared to Fe₃O₄ (65 % of light transmission). However, due to the large portion of magnetically-inactive PDVB polymer, h-PDVB@Fe₃O₄ have rather degraded magnetization value (41 emu/g), and its suspension showed highly lowered yield

stress (185 Pa at 343 kA/m) compared to Fe_3O_4 (1320 Pa).

To enhance the performance of Fe_3O_4 composite-based MR fluids, hierarchically-structured Fe_3O_4 (HS- Fe_3O_4) nanoparticles were fabricated with simple electrospaying process of Fe_3O_4 nanoparticles solution. Unlike h-PDVB@ Fe_3O_4 , HS- Fe_3O_4 did not have any polymeric materials, thus have high saturation magnetization value (70 emu/g) which is comparable to its primary Fe_3O_4 nanoparticles (73 emu/g). As a result, HS- Fe_3O_4 suspension exhibited yield stress (588 Pa at 343 kA/m) higher than 3 times of h-PDVB@ Fe_3O_4 suspension. Meanwhile, pores among Fe_3O_4 nanoparticles formed during particles aggregation lower the density of HS- Fe_3O_4 ($\rho = 3.32 \text{ g/cm}^3$) from that of primary Fe_3O_4 nanoparticles ($\rho = 4.29 \text{ g/cm}^3$), leading to improved stability results of 45 % light transmission, compared to 82 % for primary Fe_3O_4 suspensions.

Despite of performance improvement with exclusion of non-magnetic materials in composite particles, trade-off problem between performance and long-term stability still remain for spherical shaped magnetic composite particles. To minimize this trade-off, two strategy was used for synthesis of magnetic composite materials: 1) replacement of Fe_3O_4 with magnetic materials with superior magnetization and 2) increase of aspect ratio of magnetic composites. To satisfy this condition, CNT- $\text{Co}_{0.4}\text{Fe}_{0.4}\text{Ni}_{0.2}$ composite particles were prepared through synthesis of $\text{Co}_{0.4}\text{Fe}_{0.4}\text{Ni}_{0.2}$ on the surface of functionalized CNTs. Very high magnetization of $\text{Co}_{0.4}\text{Fe}_{0.4}\text{Ni}_{0.2}$ (165 emu/g) enabled CNT- $\text{Co}_{0.4}\text{Fe}_{0.4}\text{Ni}_{0.2}$ to have magnetization value (108 emu/g) even higher than bare Fe_3O_4 , resulting yield stress of CNT- $\text{Co}_{0.4}\text{Fe}_{0.4}\text{Ni}_{0.2}$ (1901 Pa at 343 kA/m) to be more than 10 times of h-PDVB@ Fe_3O_4 .

Although the density of CNT-Co_{0.4}Fe_{0.4}Ni_{0.2} ($\rho = 4.12 \text{ g/cm}^3$) was higher than h-PDVB@Fe₃O₄ ($\rho = 1.83 \text{ g/cm}^3$) and HS-Fe₃O₄ ($\rho = 3.32 \text{ g/cm}^3$), it formed 3-dimensional percolation network structures in fluids which support itself. Thus, CNT-Co_{0.4}Fe_{0.4}Ni_{0.2} MR fluid have excellent long-term stability of 22 % light transmission, which is much better than HS-Fe₃O₄ fluid.

Finally, Flake shaped sendust@Co_{0.4}Fe_{0.4}Ni_{0.2} (FS@Co_{0.4}Fe_{0.4}Ni_{0.2}) magnetic-magnetic composites were produced and used for MR fluids. FS@Co_{0.4}Fe_{0.4}Ni_{0.2} was obtained simply with synthesis of Co_{0.4}Fe_{0.4}Ni_{0.2} on surface of FS. With this process, the density of FS@Co_{0.4}Fe_{0.4}Ni_{0.2} ($\rho = 5.75 \text{ g/cm}^3$) reduced from that of FS ($\rho = 7.20 \text{ g/cm}^3$) by about 20 %. And use of magnetic sendust instead of CNTs make FS@Co_{0.4}Fe_{0.4}Ni_{0.2} to have higher magnetization value (145 emu/g) than CNT- Co_{0.4}Fe_{0.4}Ni_{0.2} (108 emu/g). With this outstanding magnetic properties, FS@Co_{0.4}Fe_{0.4}Ni_{0.2} suspension showed enormously high yield stress 5412 Pa at 343 kA/m. This is almost 29 times of static yield stress for h-PDVB@Fe₃O₄. In addition, FS@Co_{0.4}Fe_{0.4}Ni_{0.2} showed remarkable stability against sedimentation with 23 % of light transmission because of large drag coefficient of flake-shaped particle and slowed terminal velocity of FS@Co_{0.4}Fe_{0.4}Ni_{0.2} particles in MR fluid.

The performance (static yield stress at 343 kA/m) and stability (1-light transmission (%)/100) of the composite-based MR fluids are summarized in Figure 7.1. Also, those results were also compared with other bare magnetic particle-based MR fluids and composite-based MR fluids (Figure 7.2) in previous works. [1-5] For Fe₃O₄-based, spherical shaped composites (h-PDVB@Fe₃O₄ and HS-Fe₃O₄), those MR fluids have

trade-off between performance and stability, as clearly seen by red-line and blue-line in Figure 7.1. Such trade-off problem was also observed for most other MR fluids in Figure 7.2 as data for the MR fluids was placed near red, dashed-line (upper left and lower right region) showing the trade-off. For this case, optimal application of each MR fluid is needed to find because long-term stability and performance of those fluids cannot co-exist. In contrast, as $\text{Co}_{0.4}\text{Fe}_{0.4}\text{Ni}_{0.2}$ was used as magnetic materials and aspect ratio of composites increased (CNT- $\text{Co}_{0.4}\text{Fe}_{0.4}\text{Ni}_{0.2}$, and FS@ $\text{Co}_{0.4}\text{Fe}_{0.4}\text{Ni}_{0.2}$), simultaneous improvement of MR performance and stability was observed when compared to h-PDVB@ Fe_3O_4 and HS- Fe_3O_4 fluids in Figure 7.1. In contrast with other MR fluids, data for CNT- $\text{Co}_{0.4}\text{Fe}_{0.4}\text{Ni}_{0.2}$, and FS@ $\text{Co}_{0.4}\text{Fe}_{0.4}\text{Ni}_{0.2}$ was far from the dashed line and placed in upper right region of Figure 7.2, where MR fluids have both high performance and long-term stability.

From the results of previous chapters and this chapter, it can be concluded that by using proper magnetic materials and controlling the morphology of composite materials, the trade-off problem between performance and long-term stability of MR fluids is resolved. This achievement means that using this strategy, it is possible to apply one MR fluid to various fields, which can reduce the cost of selecting optimal MR fluid for each application. Also, this study provides possibility of additional enhancement in performance and long-term stability of MR fluids through fabrication of various composite magnetic materials, which can increase utilization of MR fluids much more.

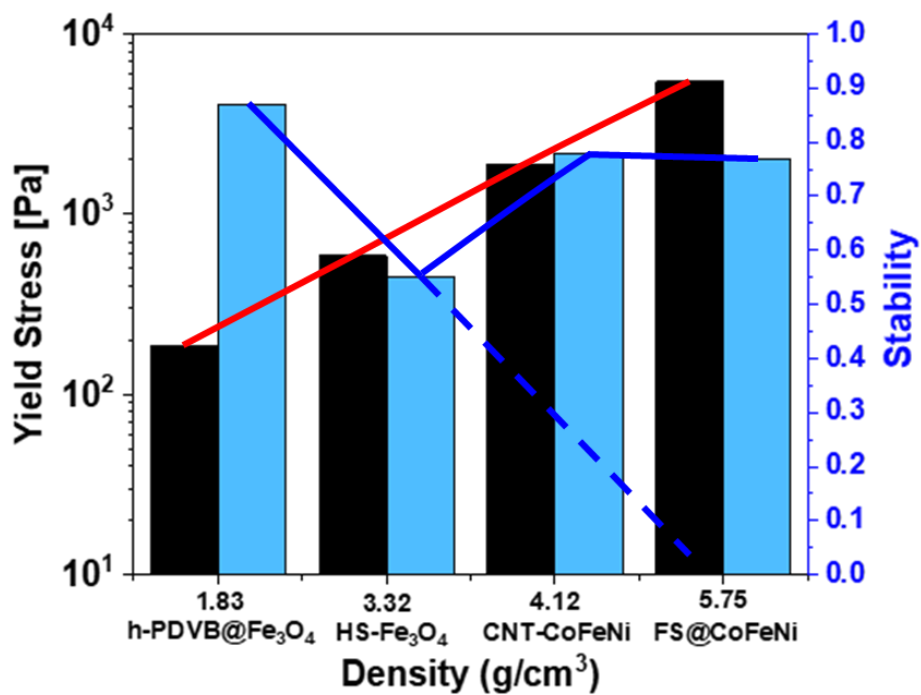


Figure 7. 1. Yield stress at 343 kA/m and long-term stability of composite-based MR fluids in this work.

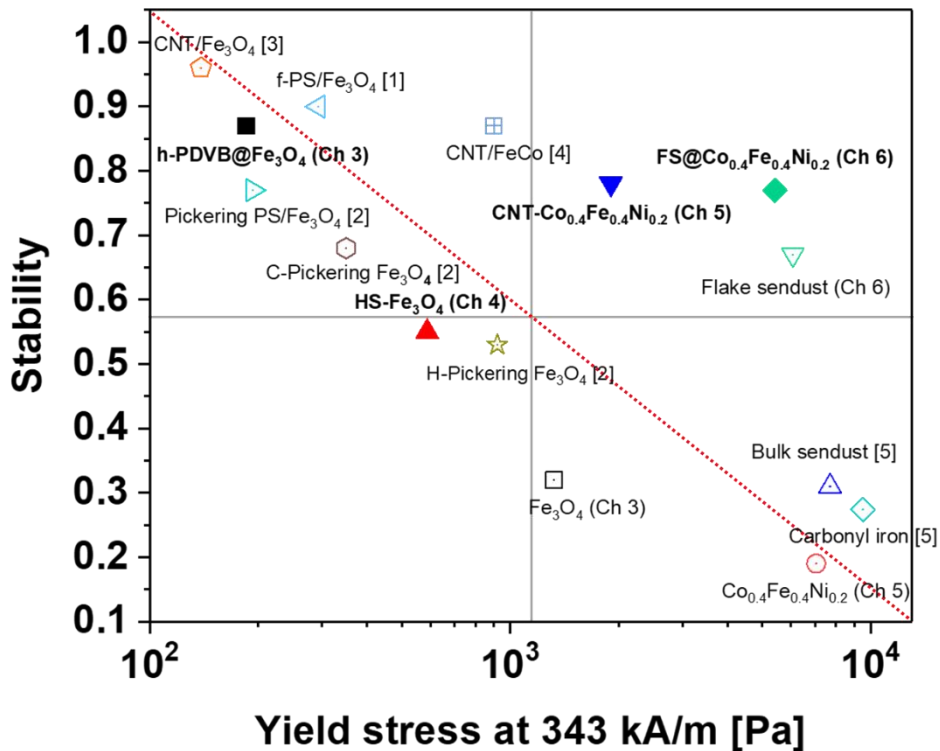


Figure 7. 2. Static yield stress and Long-term stability of various MR fluids. Open symbols correspond to bare magnetic particle-based MR fluids or composite-based fluids in previous works. Closed symbols presents composite-based MR fluids in this dissertation.

7.2. Further works

In this study, various magnetic composite materials were fabricated and MR properties and long-term stability of the composite-based MR fluids. We believe this study suggest a method to overcome trade-off between MR performance and long-term stability against sedimentation. However, there is still another challenge remained which related to stability of MR fluids: oxidation problem of magnetic materials. The magnetic materials used in this study can be oxidized due to thermal energies generated during continuous use of MR systems. With oxidation, the materials lose their magnetic properties and serious deterioration in performance of MR systems would occur. Although protective coating on magnetic materials can relieve this problem, this method also has a bad influence to their magnetic properties. Thus, it is needed to find a way for enhancing stability of MR fluids against oxidation of magnetic materials without seriously harming their MR properties.

References

- (1) Han, S.; Choi, J.; Seo, Y. P.; Park, I. J.; Choi, H. J.; Seo, Y., High-performance magnetorheological suspensions of Pickering-emulsion-polymerized polystyrene/Fe₃O₄ particles with enhanced stability. *Langmuir* 2018, 34 (8), 2807-2814.
- (2) Han, S.; Choi, J.; Kim, J.; Han, H. N.; Choi, H. J.; Seo, Y., Porous Fe₃O₄ Submicron Particles for Use in Magnetorheological Fluids. *Colloids Surf. A Physicochem. Eng. Asp.* 2020, 613, 126066.
- (3) Kim, H.; Kim, S.; Seo, Y., High-Performance Magnetorheological Suspensions of Fe₃O₄-deposited Carbon Nanotubes with Enhanced Stability. *MRS Adv.* 2019, 4 (3-4), 217-224.
- (4) Kim, H., The Study On Development of Composites for Higher Barrier Properties and Interfacial Phenomena. Ph.D. Thesis, Seoul National University, Seoul, Aug 2019.
- (5) Han, S., The Study on high performance MR fluid with enhanced sedimentation stability, Ph.D. Thesis, Seoul National University, Seoul, Aug 2020.

국문초록

자기유변유체는 자성입자가 비자성 매개액에 분산된 현탁액 형태의 스마트 물질이다. 외부 자기장 하에서 자성입자들 사이의 쌍극자로 인한 정자기성 상호작용으로 체인 형태의 구조가 형성되고, 이 구조가 유체의 흐름을 막아 매우 짧은 시간 내에 점도가 크게 향상되게 된다. 이러한 성질로 인해 자기유변유체의 유변특성을 외부 자기장을 통해 쉽게 조절하는 것이 가능하다. 이러한 외부자장에 대한 특정한 반응성으로 인해, 햅틱 디바이스 파워스티어링 펌프, 그리고 자동차, 다리, 건물 등의 충격 방지 시스템에 자기유변유체를 이용할 수 있다.

하지만 자기유변유체의 활용은 자성입자의 침전에 대한 안정성의 부족함으로 인해 크게 제한 될 수 있다. 밀도가 높은 자성입자와 밀도가 낮은 매개액 사이의 큰 밀도차이로 인해 자성입자가 빠르게 가라앉게 되면, 자기유변유체의 수명이 크게 감소하게 된다. 이러한 문제를 해결하기 위한 한가지 방법으로 자성물질과 밀도가 낮은 물질(고분자, 실리카 탄소물질 등)을 결합하여 자성복합입자를 합성함으로써, 자성입자의 밀도를 낮추고 자기유변유체의 침강안정성을 높이는 연구들이 진행되어 왔다. 하지만 이러한 경우 복합자성입자의 자기적 성질이 저하되기 때문에 자기유변유체의 침강안정성과 성능이 서

로 상충관계에 있다는 문제점을 가지고 있다.

본 논문에서는 뛰어난 성능과 침강안정성을 가지는 자기유변유체를 제조하기 위해 다양한 물질구성과 구조를 가지는 합성하였다. 첫 단계로 실리카를 템플레이트로 사용하여 할로우 구조를 가지는 고분자- Fe_3O_4 복합자성입자를 합성하였다. 할로우 구조 내부의 공동으로 인해, 입자의 밀도가 순수 Fe_3O_4 대비 40 % 수준까지 감소하였고, 이로 인해 자기유변유체의 침강안정성이 크게 상승하였다. 다음 연구로, 비자성 고분자로 인한 자기유변유체 성능의 감소를 최소화하기 위해, 간단한 전기방사 방법을 통해 계층구조를 가지는 Fe_3O_4 나노입자들을 제조하였다. 앞의 연구와 대비하여, 고분자의 배제를 통해 높은 자화값을 가지는 Fe_3O_4 나노구조입자들을 얻을 수 있었고, 이를 자기유변유체에 적용하여 할로우 고분자- Fe_3O_4 입자 기반 자기유변유체 대비 3배 이상의 성능을 가지는 자기유변유체를 얻을 수 있었다. 이와 동시에 Fe_3O_4 나노구조입자 내부에 생성된 기공들로 인해 순수 Fe_3O_4 대비 밀도가 약 23 % 정도 감소하였고, 이로 인해 침 Fe_3O_4 나노구조입자 기반 자기유변유체의 침강안정성이 향상됨을 확인할 수 있었다.

자기유변유체의 성능과 침강안정성사이의 상충성을 최소화 하기 위해서 비구형의, CoFeNi 합금기반 자성 복합입자를 합성하고 자기유변유체에 적용하였다. 먼저 개질된 카본나노튜브 표면에 CoFeNi를 합성하는 방법을 통해 카본나노튜브-CoFeNi 복합체를 합성하였다. Fe_3O_4 대비 높은 CoFeNi의 자화

값으로 인해 카본나노튜브-CoFeNi 복합체 기반 자기유변유체는 Fe_3O_4 복합체기반 유체 대비 3배에서 10배 이상의 뛰어난 유변성능을 보였다. 또한 중횡비가 높은 카본나노튜브로 인해 복합체가 유체 내에서 3차원 네트워크 구조를 형성하여, 빛 투과도 22 %의 매우 뛰어난 침강안정성을 보였다. 마지막으로 비자성 물질인 카본나노튜브를, 자성물질인 플레이크형 섀터스트로 대체한 섀터스트-CoFeNi 복합입자를 합성하여 자기유변유체에 적용하였다. 플레이크형 섀터스트의 높은 중횡비로 인해 나타나는 높은 항력계수로 인해, 해당 자기유변유체는 빛 투과도 23 %의, 높은 입자밀도 대비 매우 뛰어난 침강안정성을 보였다. 동시에, 섀터스트 CoFeNi 모두 높은 자화값을 가지는 자성물질이기 때문에, 섀터스트-CoFeNi 기반 자기유변유체의 성능이 카본나노튜브-CoFeNi 유체 대비 크게 향상되는 것을 확인할 수 있었다.

주요 키워드: 자기유변유체, 자성입자의 침강, 침강안정성, 자기유변성능, 자성복합체, 입자의 중횡비

학번: 2016-20839

Appendix

Appendix A. Nonisothermal Crystallization Behaviors of Structure-Modified Polyamides (Nylon 6s)

A. 1. Introduction

Nylon is a condensation polymer with amide bonds in the backbone which consists of several different types of monomers in combination with one another. Its many outstanding properties such as exceptionally strong, durable, chemical-resistant, elastic, easy to wash, and relatively high abrasion resistance make it widely used for various purposes such as clothes, reinforcement in rubber material such as car tires, a rope, or a thread, and a range of injection-molded parts for vehicles and machinery [1–3]. It can be also easily mixed with a variety of additives to create different variations with significantly different material properties [4].

However, polyamides usually have a relatively low molar mass compared to other polymers synthesized by free-radical polymerization [5]. This characteristic is common to all polymers synthesized by the step polymerization process. Because of their low molar mass, these melts generally have quite different rheological properties from other polymers.

They show a wide Newtonian viscosity plateau over a wide range of shear rates and have very low melt viscosities [5,6]. The result of this property is the lack of processibility in the extrusion process such as a blow molding process because of the low degree of shear thinning [7]. Moreover, their weak strain-hardening gives rise to difficulties in processing operations where elongational properties dominate [5]. The issue is then how can the rheological properties of these polyamides be controlled to easily meet the requirements under different processing conditions [6,7]. One possible method to solve the characteristic rheological problem is to change the molecular weight and structure of the molecules in a controllable manner. The chain relaxation dynamics and the rheological properties of polymer melts vary significantly because of the resulting polymer chain entanglements [6]. We reported a simple process of changing the molecular structure. This makes it easy to generate long-chain branches in a controllable manner without creating a network structure [6–8]. By adding a linking agent, a branched structure can be created in the polyamide backbone. The relaxation dynamics and rheological properties of a polyamide [nylon 6 (Ny6)] melt were significantly improved by the formation of three-arm or four-arm (H) star polymer molecules, the branches of which were placed in the connecting molecules [6]. Zero shear viscosity increased more than 200 times the linear chain viscosity without forming a network structure. The storage modulus and loss modulus at low frequencies increased more than 10^4 and 10^3 times compared to neat Ny6 [6,8]. These results may solve the rheological barriers of polyamide melts and open up new possibilities for a wide range of applications. We have also succeeded in synthesizing Ny6 by reactive in situ extrusion using a linking agent (a diepoxide or a diamine) [7,9]. The linking agent reacted with

growing Ny6 chains during anionic polymerization in the extruder to produce branched Ny6 chains with branch structures without the formation of cross-linked molecules, which was accompanied by a remarkable improvement in physical and rheological properties [7–9]. Even though the produced or modified nylons exhibit significantly improved rheological properties, the introduction of the linking agent reduced both melt enthalpy and crystallinity [6,7]. This means that the crystallization of Ny6 was hindered by structure changes. The branched part of the Ny6 chains had low mobility because of its binding to the backbone, making it difficult to crystallize [7–9]. The crystallinity was then possibly affected by the branched structure [7,9]. This is different from the case of a commercial Ny6 modification [6]. In that case, the branch was a long chain involved in the crystallization in different layers, so the crystallinity does not decrease significantly. However, the branches produced in the reactive extrusion synthesis can be quite short enough to disrupt the main chain ordering. The crystallinity then decreases with the addition of the linking agent. The amount of the linking agent was then a limiting factor for the short branched molecules [7–9]. Although the molecular weight of modified nylons was increased in all modification processes which help improve physical properties, a decrease in the crystallinity of the solid polymer synthesized by the reactive extrusion process can partially offset the molecular weight effect. Therefore, investigating the crystallization behavior of the structurally modified nylons is necessary to examine the difference in crystallinity as it has a serious impact on the potential properties of the polymer. This study investigated the crystallization kinetics and the crystalline morphology of the modified commercial nylons as a part of an ongoing effort to

characterize the physical properties of the structure-modified Ny6s. Because the long branching affects the crystallization behavior and the resulting crystalline morphology, the modified nylons are expected to have different crystallization characteristics from the normal crystal growth that usually occurs in Ny6 [10].

Isothermal crystallization kinetics using the Avrami equation is usually applied for the crystallization kinetics [11]. However, it is difficult to keep the molten sample in an amorphous state while it is being cooled to the crystallization temperature in an isothermal crystallization experiment. In addition, the normal crystallization process in commercial production is nonisothermal. The nonisothermal crystallization kinetics was theoretically investigated by Ozawa [12]. However, it has an implicit drawback of comparing the conversions at fixed temperatures at different cooling rates which can lead to deviations from the predicted linear behavior [12–15]. We have devised a nonisothermal crystallization analysis scheme that can avoid the problem of the Ozawa analysis [14,15]. The nonisothermal crystallization kinetics used can provide additional insights into the crystallite structures that occurs during the formation of nanocomposites [16–18]. Therefore, the objective of this study is to apply the nonisothermal analysis method to the crystallization behavior of modified Ny6 molecules, with an emphasis on the morphological changes caused by the presence of long-chain branches.

A. 2. Experimental Section

A. 2. 1. Materials

Ny6H was a Kolon product (KN171, Korea). The number average molar mass (M_n) was found to be $24,200 \text{ g mol}^{-1}$ with a polydispersity index of 3.5. This molar mass was much higher than M_n of Ny6 (2233 g mol^{-1}) [19]. It is a high viscosity-grade Ny6. For a comparison, we also used another Ny6 of medium viscosity grade, Ny6M (KN111, $M_n = 20,000 \text{ g mol}^{-1}$, $\eta_{\text{rel}} = 2.45$ in 96% H_2SO_4), also a Kolon product. The high viscosity-grade Ny6H (KN171) was used to produce the modified Ny6 in order to prepare high viscosity nylons. For synthesis of modified Ny6, 4,4'-di(2,3-epoxypropyloxy) phenyl benzoate (DEPPB) was used as a linking agent (Figure 1). Details of the process were fully explained in the previous study [6].

A. 2. 2. Characterization

TGA was performed on a TA instrument under a nitrogen atmosphere with a heating rate of $20 \text{ }^\circ\text{C}/\text{min}$ in a temperature range of $50\text{--}650 \text{ }^\circ\text{C}$. Differential scanning calorimetry (DSC) was performed on a METTLERTOLEDO DSC832e under a nitrogen atmosphere with a heating rate of $10 \text{ }^\circ\text{C}/\text{min}$ in a temperature range of $50\text{--}240 \text{ }^\circ\text{C}$. To examine nonisothermal crystallization, the samples were melted at $240 \text{ }^\circ\text{C}$ for 5 min to eliminate the previous thermal history and then cooled at different cooling rates. A polarized optical microscope

(Olympus BX-51) equipped with a METTLER-TOLEDO FP82 HT hot stage and a digicam II camera was used to record the growth of the crystallites.

A. 2. 3. Description of the Nonisothermal Crystallization Model

Here, we briefly reiterate the nonisothermal analysis scheme [14,15]. In the Ozawa equation, the time variable in the Avrami equation is replaced by the cooling rate term as follows

$$\ln[-\ln(1 - x_v(T)_u)] = \ln K(T) - n \ln U \quad (1)$$

where n is the Avrami exponent, $x_v(T)$ is the volume fraction of the polymer transformed at a temperature T , U is the cooling rate, and $K(T)$ is the so-called cooling function, which is only a function of temperature [14]. The volume fraction of a polymer, $x_v(T)$, can be easily obtained by converting the weight fraction of the polymer, $x_w(T)$, using the density of the amorphous phase and the density of the crystallized phase [15]. Adopting the exponential dependence of the $K(T)$ function ($\ln K(T) = aT + b$), eq 1 can be expressed as a linear relation between T_{\max} and $\ln U$; that is, $n \ln U = a T_{\max} + b - \ln[-\ln(1 - x_v(T_{\max})_u)]$ [14–16]. Therefore, eq 1 can be rewritten as

$$\ln[-\ln(1-x_v(T)_u)] = a (T-T_{\max}) + \ln[-\ln(1 - x_v(T_{\max})_u)] \quad (2)$$

All parameter values can be determined without resorting to any numerical process [17,18]. Plotting $\ln[-\ln(1-x_v(T)_u)]$ versus $T-T_{\max}$ gives a straight line whose slope represents the

parameter a value and plotting T_{ma} versus $\ln U$ presents a straight line with a slope of n/a and an intercept is $(\ln[-\ln(1-x_v(T_{\text{max}})U)] - b)/a$.

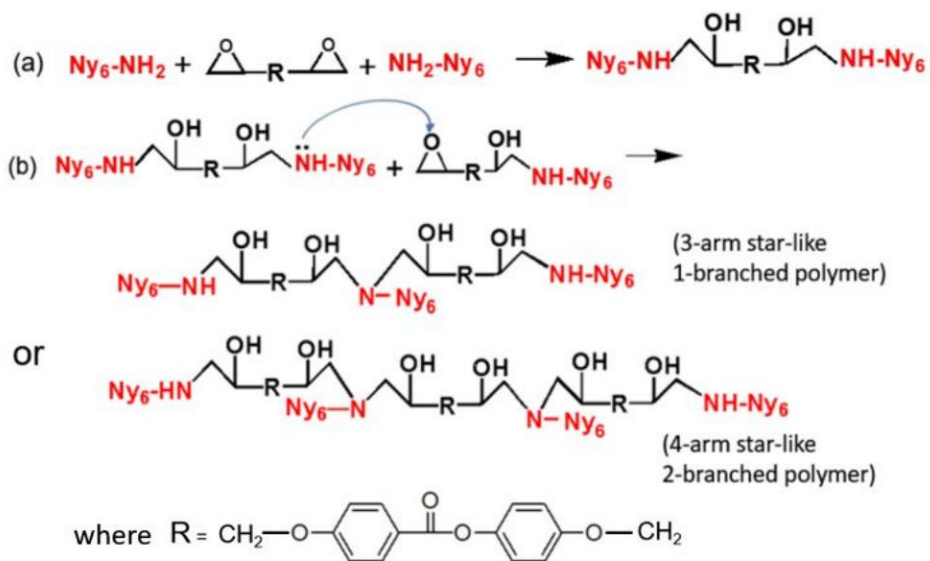


Figure A. 1. Reaction of the Linking Agent (DEPPB) with Nylon 6 Molecules (a) The reactive group molar ratio is 1:1 (linking of two nylon 6 molecules). (b) The reactive group molar ratio is greater than 1:1 (3- or 4-armed starlike polymer formation)

A. 3. Results and Discussion

A previous report introduced a novel strategy for controlling the polymer melt rheology and the chain relaxation dynamics [6]. The modification process involves a linking agent that can connect two chains in a linear matter first to double its molar mass and then later generate three- or four-armed polymers [6]. Long-chain branches were easily generated in a controllable manner without the formation of a network structure (see the Supporting Information for the chemical structure of the linking agent and the reactions [6]). This has resulted in unusually large improvements in the rheological properties of the polymer melt and thus its relaxation dynamics.

Figure 2 shows the melt viscosities of various modified Ny6 as a function of frequency. Neat Ny6 melts show a broad Newtonian plateau of low viscosity until the frequencies reach 100 rad/s, above which it exhibits weak shear thinning. High viscosity-grade Ny6 (KN171 and Ny6H) displays three times higher viscosity than medium-grade Ny6 (KN111 and Ny6M). Modified nylons show different tendencies depending on the linking agent concentration. When the molar amount of the epoxy group in the sample was larger than that of the Ny6 amine group (over 1:1 ratio), the melt viscosities increased significantly higher than that of Ny6H (see the Supporting Information for the reaction between the linking agent and Ny6 molecules). Surprisingly, there is no apparent Newtonian plateau in these samples but only strong shear-thinning behavior is observed over the whole frequency range [6]. The shear-thinning behavior of the modified Ny6 melts in Figure 1

could be well-explained using a simple Carreau equation using the Cox-Merz rule [10]. The zero shear rate viscosity obtained from the Carreau model (Table 1) increased with the addition of the linking agent (DEPPB, (4,4'-di(2,3-epoxypropyloxy) phenyl benzoate)) concentration. After reaching the peak of 1.09×10^5 Pa·s for DEPPB (2), it decreased to 9.07×10^4 Pa·s for DEPPB (2.25). The peak melt viscosity was more than 200 times that of the Ny6H melt. The intrinsic viscosity was measured and the molar mass was calculated using the Mark–Houwink equation (Table 1) [6]. Like the melt viscosity, the viscosity average molar mass reached the maximum when the molar ratio of the reactive functional groups was 2 (DEPPB(2)) and then it decreased. The viscosity average molar mass of DEPPB(2) was about 1.6 times that of Ny6H. Assuming the melt viscosity to follow the 3.4 power law ($\eta \sim M^{3.4}$), this small molar mass change (1.6 times) can increase the melt viscosity by less than 5 times of Ny6H. [20] Hence, it verifies that a significant increase in the melt viscosity of DEPPB(2) with strong shear thinning without the appearance of Newtonian plateau is inconsistent with the increase in the linear molar mass because of the linking agent. Neither was it due to the cross-linking reaction because the reacted extrudates could be reprocessed many times without showing any signs of solidification in the extrusion (Figure 3 of ref 6). Also, one of the reactants must have three functional groups on the molecules to proceed the cross-linking reaction, but the linking agent, DEPPB, has two functional groups and the Ny6H molecule has a monoamine group at the end of the chain. The other chain end of Ny6H terminates with the ϵ -caprolactam polymerization initiator. Therefore, no crosslinking reaction occurs [17]. Also, light scattering analysis of the polymer solution did not detect any particles insoluble in formic

acid [6]. According to the Einstein equation, even if crosslinking occurred, the amount of cross-linked particles could not increase the melt viscosity so much [20]. All these observations implicate that the cross-linking reaction or gelation cannot be the reason for unexpectedly high melt viscosity at low shear rates and the strong shear thinning [6]. Figure 3 shows the thermal degradation characteristics of all nylons by thermogravimetric analysis (TGA). The medium viscosity-grade Ny6M exhibits earlier degradation behavior than Ny6H and modified nylons because of its low molar mass and hence low thermal properties. The modified nylons demonstrate two different degradation trajectories. Modified nylons of linear molecules (no. 2 and 3) follow the trajectory of Ny6H, but others (no. 4–7) of high melt viscosity having the nonlinear molecular structure (branching) show better degradation behavior because of the enhanced molar mass and the different molecular structures (Figure 1 and Figure 2). On the other hand, in the latter group of samples, the 5 wt % degradation temperature (Table 2) increased slightly. This is consistent with the change in molar mass (Table 1). The starting temperature of degradation did not change noticeably. The molar mass of the branched molecules increased but was not sufficient to delay the onset of the degradation of the modified nylons. It is also consistent with the change in zero shear rate viscosity in different samples (Table 1). Another point of difference is that all linear polymers were totally degraded at 600 °C, whereas a small amount (less than 4 wt %) of samples (no. 4–7) remained at that temperature. At the temperature going over ~400 °C, the C–C bonds of the nylon backbone spontaneously break to yield two shorter chains furnished with a terminal radical. It can be conjectured that some cross-linking reactions between degrading radicals might happen at that

degradation temperature, although we did not investigate further details. As mentioned in our previous study, the crystallinity decreased slightly with the chain structure modification (branching) [8,9]. DSC scan curves are presented in Figure 4. All curves were recorded after cooling the melts at 240 °C with various cooling rates. The main difference between different cooling rates is in the characteristic onset and peak crystallization temperature which are related to the associated enthalpy change and the peak-broadening effect in the modified Ny6 compared to neat Ny6 (Ny6H). The onset temperatures of the modified Ny6 were lower than those of neat Ny6H. This means that the degree of supercooling necessary for the crystallization was larger for all modified Ny6's. This consequence is attributed to the slowing down of the crystallization by the branching structure which hinders chain ordering in the crystallization process. All of the samples exhibit a single crystallization exotherm. As the cooling rate goes up, the polymer melt has less time for crystallization. Thus, the exotherm peaks appear at lower temperature. T_{max} of the modified Ny6s is also lower than those of the neat Ny6H at low cooling rates because they need more time for chain ordering. One exception is the sample 2 which has a larger molar mass than pure Ny6 (H or M) but still relatively low zero shear rate viscosity because it does not have branching arms in the Ny6 molecule backbones yet (Table 1). A high melt viscosity restricts the movement of the molecules, but the arrangement of local molecules through the hydrogen bonds improves with the molecular weight, which makes the simple chain arrangement for crystallization easier. In the case of other modified polymers, the change in the chain structure (branching) disrupts the arrangement of the chain molecules. The thermograms also show that the curves are symmetric around T_{max} , which implies that

crystallization occurs as much after T_{\max} . This exemplifies that the dynamic restriction (high melt viscosity) is less critical than the structural ordering effect (participation of the branching moiety in crystallization). Because of the restriction in the chain conformation, it takes more time for the modified molecules to become ordered. A linear variation of the maximum temperature crystallization isotherm, T_{\max} , with the logarithm of the cooling rates ($\ln U$) is displayed in Figure 5. It shows predicted linear behavior when the cooling rate is low (was quite evident [8,9]). The melting temperatures of the Ny6H and Ny6M were 224 and 220 °C, respectively. The melting temperatures of the modified nylons were 3–4 °C lower which indicates that the modified nylons have a thinner lamellar thickness of the Ny6 chains because of the structure change [18]. Modified nylons show peak broadening compared to neat nylons because of the retardation of chain relaxation and movement by the high viscosity. The plot of $\ln[-\ln(1 - x_v(T)U)]$ versus $T - T_{\max}$ provides a straight line with a slope of n/a (Figure 8). Calculated Avrami constant values from Figures 5 and 8 are listed in Table 3. The calculated values of the Avrami exponent, n , for neat Ny6H were between 5.2 and 5.7 with an average value of 5.4. This value is close to the characteristic value for the heterogeneous nucleation [11]. Ny6H is a polyamide of high viscosity grade that includes unknown catalysts or chemicals for the molar mass increase which is considered to act as the heterogeneous nuclei. This can be proved by the morphological observation later. In contrast, the Avrami constant of Ny6M shows the n value between 3.2 and 4.4 with an average value of 3.7, of which the crystallization mechanism is the normal threedimensional growth rate and slow down of the nucleation rate. The modified nylons all show the Avrami constant values between 3.7 and 4.4, close

to that occurred by the solid sheaf growth in three-dimensional space with athermal nucleation [18]. As the cooling rate increases, the Avrami index decreases. If the cooling rate becomes faster, then less time is allowed for a molecule to be relaxed and ordered. For the heterogeneous crystallites at high cooling rates, crystallization occurs at an earlier stage than that for low cooling rates. In the early stage of Ny6M, the Avrami constant values are close to 3 which means that more Ny6M molecules participate in three-dimensional growth at slow cooling rates. On the other hand, Ny6H molecules have high Avrami constant values because of heterogeneous nucleation. The Ny6H crystallites formed in the early stage do not have enough space to be fully ordered and grow. Thus, the size of hedrite decreases significantly compared to that of Ny6M, as shown below. Figure 9 shows the crystalline morphology by polarized optical microscopy. Ny6M melt forms large spherulites with slightly twisted lamellae. [23] In contrast, the crystal structure of Ny6H consists of smaller ones of hedrites. The photomicrographs clearly reveal that the Ny6M has a larger, more developed spherulitic structure which is consistent with a lower rate of nucleation, yielding a lower, “overall” crystallization rate. This morphology difference can elucidate the Avrami constant difference. Because of excessive heterogeneous nucleation sites for Ny6H, the crystallites did not grow as large as those for Ny6M. The half crystallization time ($t_{1/2}$) values increase with the cooling rate because of faster growth and crystallization (Table 4). It increases more rapidly for Ny6H than Ny6M because of heterogeneous nucleation. The morphological appearance of modified nylons is similar to Ny6H but much smaller than that. Because of the rheological property restriction (much higher viscosity) and branching structure, the crystallite could not grow so large as Ny6H.

Also, the branching structure seriously hinders the homogeneous nucleation. This morphological appearance is in agreement with the Avrami constant n values. The less crystallite formation and slow growth definitely slow down the crystallization speed and/or nucleation rate. Thus, the Avrami constant values of modified nylons are around 4 decreased from that of Ny6H (ca. 5.4).

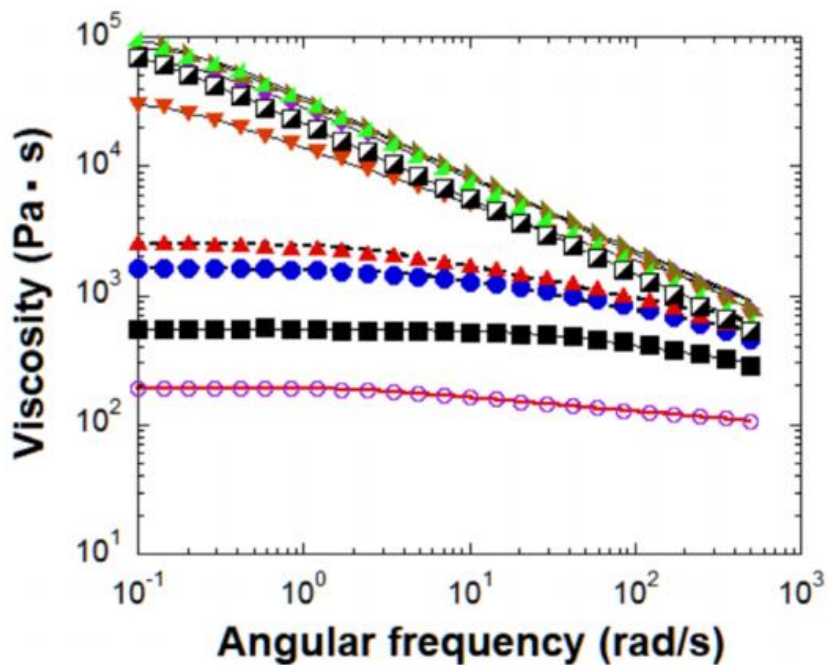


Figure A. 2. Dynamic melt viscosities of Ny6H (■), Ny6M (violet ○), and modified Ny6s (approximate ratio between amine and epoxy groups); (blue ●) 1:0.2 (sample 1, DEPPB(0.2)), (red ▲) 1:0.4 (sample 2, DEPPB (0.4)), (red ▼) 1:0.6 (sample 3, DEPPB (0.6)), (dark yellow ◆) 1:1 (sample 4, DEPPB(1)), (▣) 1:1.25 (sample 5, DEPPB(1.25)), (green ◀) 1:2 (sample 6, DEPPB(2)), and (dark yellow ▶) 1:2.25 (sample 7, DEPPB (2.25)) measured at 250 °C

Table A. 1. Viscosity Molar Mass Calculated from the Mark–Houwink Equation

Molar ratio between the epoxy group of the linking agent and the amine group of nylon6	Viscosity molar mass (g/mole) after the reaction	Zero shear rate viscosity (Pa-s) from the Carreau equation
0.0 (Ny6M)	2.82×10^4	200
0.0 (Ny6H)	3.24×10^4	540
0.2 (sample1)	3.38×10^4	1600
0.4 (sample2)	3.76×10^4	2500
0.6 (sample3)	3.97×10^4	3.33×10^4
1.0 (sample4)	4.54×10^4	7.24×10^4
1.25(sample5)	4.91×10^4	8.85×10^4
2.0 (sample6)	4.97×10^4	10.9×10^4
2.25(sample7)	4.18×10^4	9.07×10^4

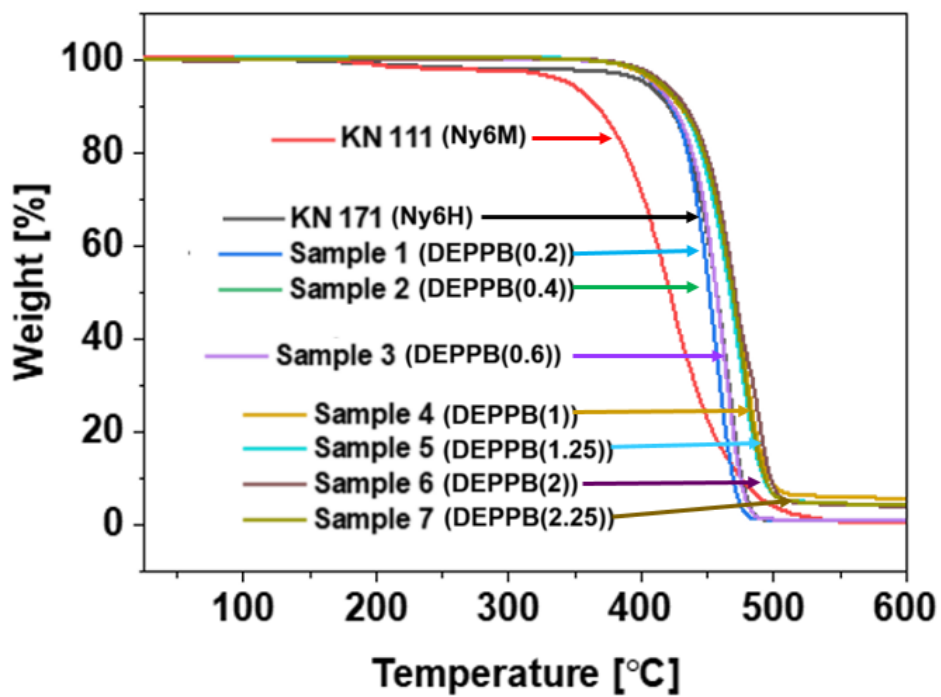


Figure A. 2. TGA graphs for homo-Ny6s (Ny6M and Ny6H) and modified nylons.

Table A. 2. $T_{d,5\%}$ of Nylons and Modified Nylons

Name of sample	$T_{d,5\%}$ (°C)
Ny6M	370
Ny6H	403
Sample 1 (DEPPB(0.2))	408
Sample 2 (DEPPB(0.4))	409
Sample 3 (DEPPB(0.6))	410
Sample 4 (DEPPB(1))	411
Sample 5 (DEPPB(1.25))	414
Sample 6 (DEPPB(2))	417
Sample 7 (DEPPB(2.25))	414

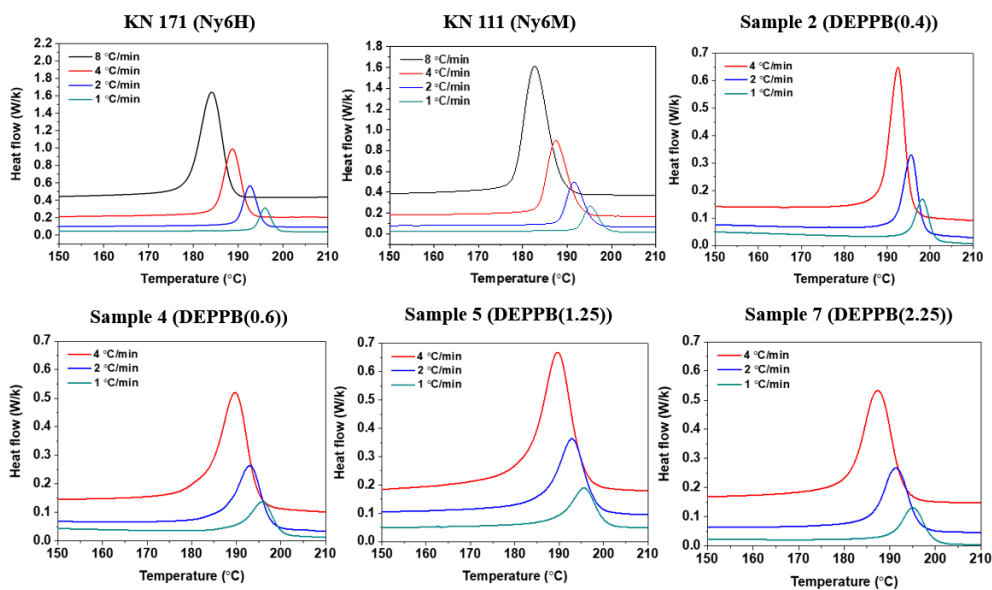


Figure A. 3. DSC curves of nonisothermal crystallization at different cooling rates.

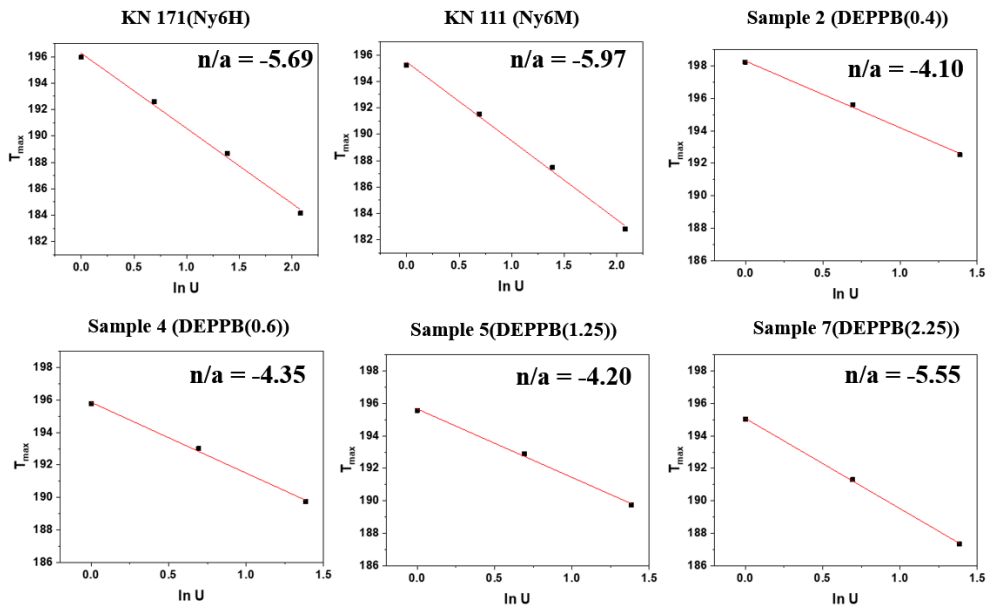


Figure A. 4. Evolution of T_{\max} as a function of $\ln(U)$.

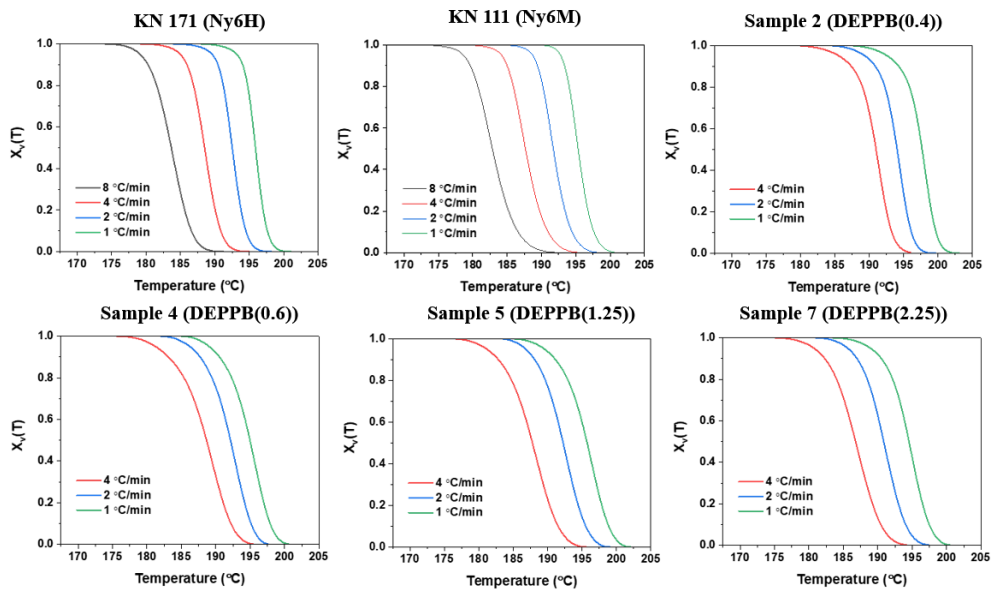


Figure A. 5. Development of relative crystallinity, x_v , as a function of temperature at different cooling rates.

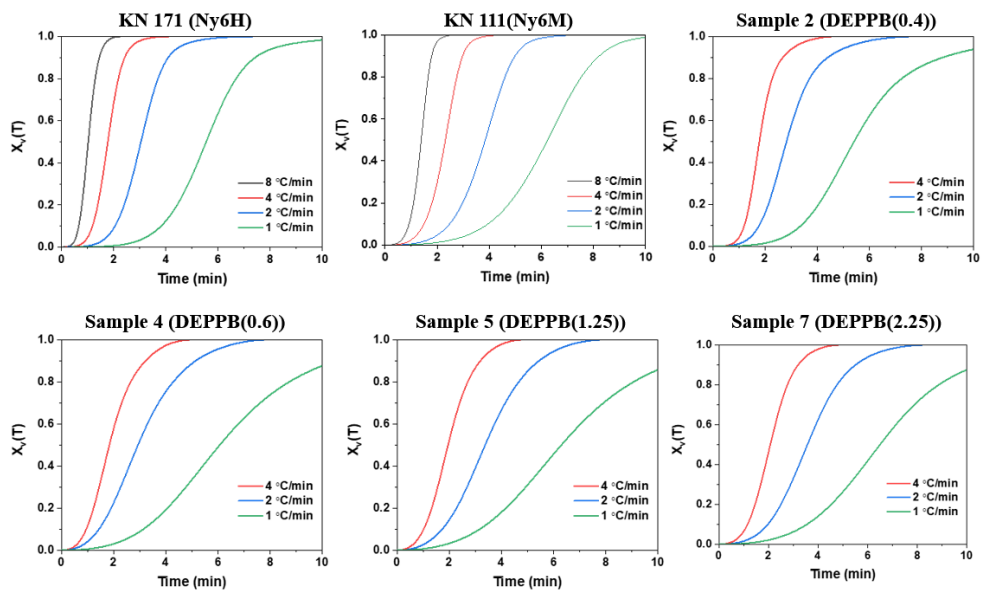


Figure A. 6. Development of relative crystallinity, x_v , as a function of time at different cooling rates.

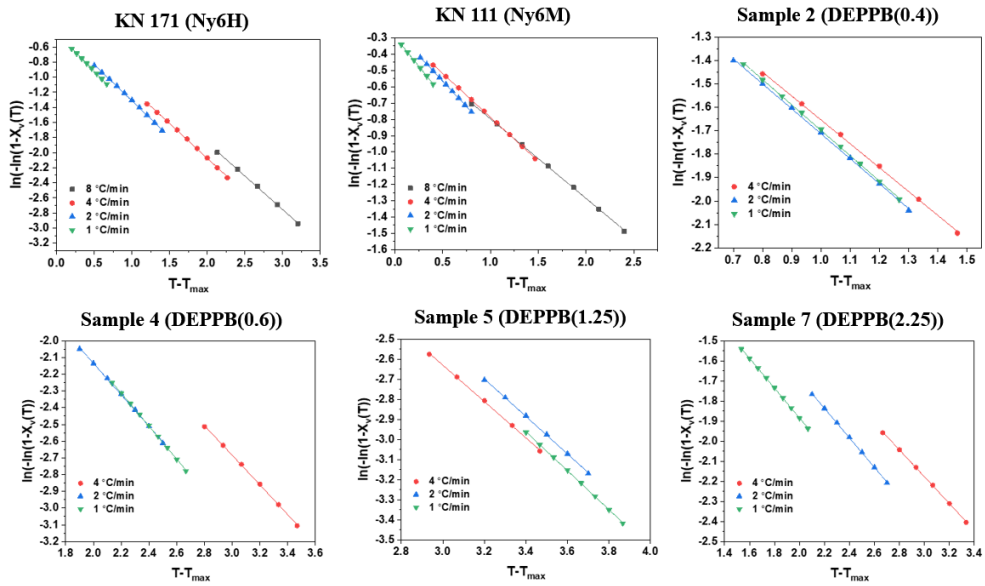


Figure A. 7. Plot of $\ln[-\ln(1 - x_v(T))]$ vs $T - T_{max}$ at different cooling rates.

Table A. 3. Avrami Constant, n, Values

cooling rate (°C/min)	Ny6M	Ny6 H	Sample 2 (DEPPB (0.4))	Sample4 (DEPPB (1))	Sample5 (DEPPB(1.25))	Sample7 (DEPPB(2.25))
1	4.44	5.73	4.18	3.86	3.81	3.71
2	3.71	5.44	4.37	4.09	3.93	4.08
4	3.20	5.22	4.45	4.29	4.09	4.13
Average	3.78	5.46	4.33	4.08	3.94	3.97

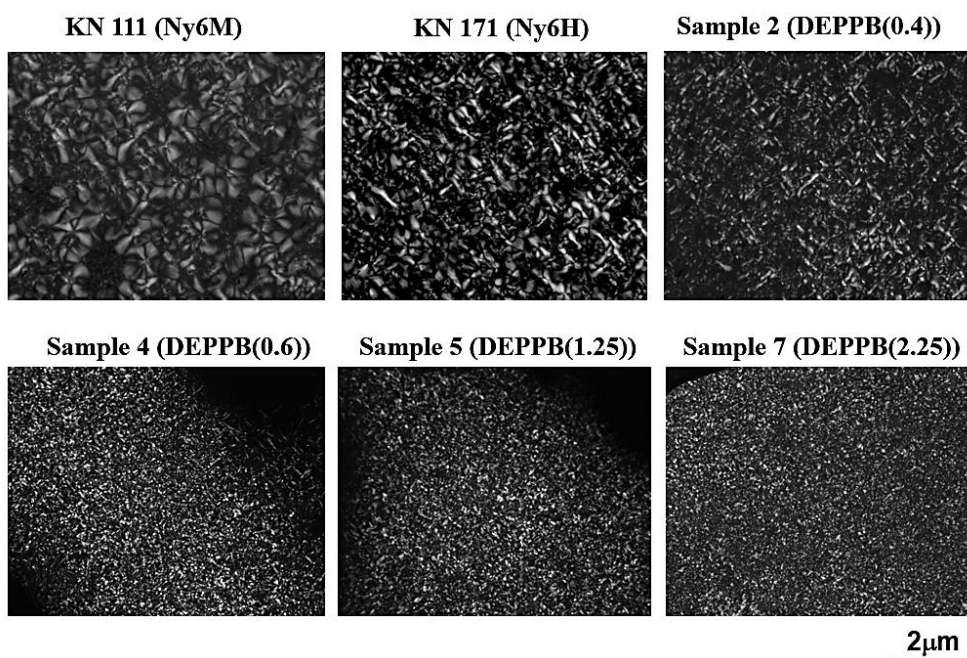


Figure A. 8. POM images of Ny6s at cooling rate, 4 °C/min

Table A. 4. The half crystallization time $t_{1/2}$

cooling rate (°C/min)	Ny6 M	Ny6 H	Sample2 (DEPPB (0.4))	Sample4 (DEPPB (1))	Sample5 (DEPPB(1. 25))	Sample7 (DEPPB(2.2 5))
1	6.23	5.54	5.42	6.03	6.3	6.49
2	3.84	3.05	2.83	2.92	3.38	3.58
4	2.32	1.77	1.79	1.84	1.95	2.08

A. 4. Conclusions

Nonisothermal crystallization analysis of neat Ny6s (Ny6H of high viscosity grade and Ny6M of medium viscosity grade) and modified nylons (modified Ny6H) provides some important information: the structural variation as well as the heterogeneous nuclei decides the crystalline structures of these nylons. The Avrami exponent of the Ny6H was close to 5.4 indicating that the crystallites follows the crystallization process of the heterogeneous nucleation, whereas that of the Ny6M was close to 4, indicating the kinetics of the normal three-dimensional growth rate and slow down of nucleation. [21,22] All the modified nylons of Ny6H show the Avrami constant values between 3.8 and 4.4, which are close to that occurred by the solid sheaf growth in three-dimensional space with athermal nucleation because of crystallization hindrance by the branching point [23]

The morphology looked differently for Ny6H and Ny6M; Ny6M melt forms large spherulites with slightly twisted lamellae, whereas the crystal structure of Ny6H consists of smaller ones of hedrites. For Ny6H, the crystallites did not grow so large as those in Ny6M because of excessive heterogeneous nucleation sites while the crystalline morphology of Ny6M was that of large spherulites with slightly twisted lamellae. This morphology difference can elucidate the Avrami constant difference. The half-crystallization time ($t_{1/2}$) values increase with cooling rates because of faster growth and crystallization (see Table 4). It increases more rapidly for Ny6H than Ny6M because of heterogeneous nucleation. On the other hand, the crystallite morphologies of modified

nylons look similar to that of Ny6H but in much smaller sizes. The rheological restriction (much higher viscosity) and the branching structure prevent the crystallite growth from being as large as that of Ny6H. Also, the branching structure inhibits the homogeneous nucleation. This morphological appearance is in agreement with the Avrami constant value difference. The less crystallite formation and slow growth definitely slow down the crystallization speed and/or nucleation rate. The Avrami constant values of modified nylons were around 4, decreased from that of Ny6H (ca. 5.4). The nonisothermal crystallization analysis provides the clue of morphological development as well as molecular ordering and relaxation of the modified nylons. Thermal stability of the modified nylons was better than that of pure Ny6H because of the increased molecular weight.

References

- (1) Rulkens, R.; Koning, C. E. (2012). Chemistry and technology of polyamides. In K. Matyjaszewski, & M. Moller (Eds.), *Polymer Science : a Comprehensive Reference* (pp. 431-467). Elsevier. <https://doi.org/10.1016/B978-0-444-53349-4.00147-3>
- (2) Russo, S.; Casazza, E. Ring-Opening polymerization of cyclic amides (Lactams). in *Polymer Science: A Comprehensive Reference*; Matyjaszewski, K., Möller, M., Eds.; Elsevier: Amsterdam, 2012; pp 331-396
- (3) Hashimoto, K. Ring-opening polymerization of lactams. Living anionic polymerization and its applications. *Prog. Polym. Sci.* **2000**, *25*, 1411–1462.
- (4) Rulkens, R. ; Koning, C., Chapter 5.18, Chemistry and Technology of Polyamides in *Polymer Science: A Comprehensive Reference* (Eds. Matyjaszewski, K. and M. Möller), Volume 5, Elsevier, Amsterdam, 2012
- (5) Dijkstra, D.J. Guidelines for rheological characterization of polyamide melts *Pure Appl. Chem.*, **2009**, *81*, 339-349
- (6) Seo, Y. P.; Seo, Y. Effect of molecular structure change on the melt rheological properties of a polyamide (nylon 6), *ACS Omega*, **2018**, *3*, 16549-16555.
- (7) Steeman, P.; Nijenhuis, A. The effect of random branching on the balance between flow and mechanical properties of polyamide-6, *Polymer* **2010**, *51*, 2700-2707
- (8) Oh, K.; Kim, H.; Seo, Y. Long-living anions could dramatically change the overall physical properties of a polyamide (Nylon 6) synthesized by a novel process *ACS*

- (9) Kim, H.; Oh, K.; Seo, Y., Rheological and mechanical properties of a novel polyamide 6 synthesized by anionic polymerization of ϵ -caprolactam in a twin-screw extruder, *Polymer*, **2019**, 179, 196–201
- (10) Dealy, J.M.; Larson, R.G., *Structure and Rheology of Molten Polymers* (Hanser, Munich, 2006)
- (11) Wunderlich, B. In Thermal characterization of polymeric materials; Turi, A., Ed.; Academic Press: New York, 1997; Chapter 2.
- (12) Ozawa, T. Kinetics of non-isothermal crystallization, *Polymer* **1971**, 12, 150-158.
- (13) Hong, S. M.; Seo, Y., Crystallization of a polypropylene terpolymer made by a Ziegler-Natta catalyst: formation of gamma-phase *J. Physical Chemistry B*, **2007**, 111, 3571- 3575.
- (14) Seo, Y.; Kang, T.; Hong, S. M.; Choi, H. J., Nonisothermal crystallization behaviors of a polyolefin terpolymer and its foam *Polymer*, **2007**, 48, 3844~3849.
- (15) Seo, Y.; Kim, S., Nonisothermal crystallization behavior of poly(aryl ether ether ketone) *Polym. Eng.Sci.*, **2001**, 41, 940~945.
- (16) Seo, Y., Nonisothermal crystallization kinetics of polytetrafluoroethylene *Polym. Eng. Sci.* **2000**, 40, 1293~1297.
- (17) Lim, J. Kim, J.; Kim, S.; Kwak, S.; Lee, Y.; Seo, Y. Nonisothermal crystallization

behaviors of nanocomposites of poly(vinylidene fluoride) and multiwalled carbon nanotubes *Polymer*, **2015**, *62*, 11~18.

(18) Oh, K.; Chuah, W.; Park, S.; Kim, J., Kwak, S., Kim, S.; Seo Y, Nonisothermal crystallization behaviors of nanocomposites prepared by in situ polymerization of high-density polyethylene on tungsten oxide particles *Macromol. Res.*, **2015**, *23*, 265~272.

(19) Young, R.J.; Lovell, P.A.; *Introduction to Polymers* (3rd Edn, CRC Press, Boca Raton, 2011)

(20) Wu, S. Chain Structure and Entanglement, *J. Polym. Sci.: Part B: Poly. Phys.*, **1989**, *27*, 723-741

(21) Turska, E.; Gogolewski, Study on crystallization of nylon-6 (polycapramide). Part 1. Isothermal crystallization, *Polymer*, **1971**, *12*, 616-628

(22) Turska, E.; Gogolewski, Study on crystallization of nylon-6 (polycapramide)" Part 2. Effect of molecular weight on isothermal crystallization kinetics, *Polymer*, **1971**, *12*, 629-641

(23) Martins, J. C. A.; Novack, K. M.; Gomes, A. S., Non-isothermal crystallization kinetics of thermotropic polyesters with flexible spacers in the main chain, *Polymer*, **1998**, *39*, 6941–6944

(24) Khanna, Y.P.; Reimschuessel, A.C.; Benerjie, A.; Altman, C., Memory effects in polymers. II. processing history vs. crystallization rate of Nylon 6-observation of

phenomenon and product behavior, *Polym. Eng. Sci.*, **1988**, 28, 1600-1606